THE UNIVERSITY *of* EDINBURGH

Underground measurement of hydrogen-burning reactions on ^{17,18}O at energies of astrophysical interest

Carlo Giulio Bruno

Doctor of Philosophy
The University of Edinburgh
July 2017

Abstract

The ^{17,18}O(p,α)^{14,15}N nuclear reactions play an important role in several astrophysical scenarios, and in Asymptotic Giant Branch (AGB) stars in particular. These stars are the site of several mixing and recirculating processes that transport matter from their hot cores to their cooler surfaces, and *vice versa*. Some of these mixing processes are still not well understood. Constraining them would improve our knowledge of stars that are in, or will enter, the AGB phase, including our own Sun. An ideal way to trace these poorly understood mixing processes are provided by the rare, stable ^{17,18}O isotopes. Their abundances are strongly sensitive to the ^{17,18}O(p,α)^{14,15}N reactions. At temperatures of astrophysical interest, the ^{17}O(p,α)^{14}N reaction is dominated by a narrow, isolated resonance at E_{proton}=70 keV. This resonance has been studied several times in the past, using both direct and indirect methods. However, the picture painted in the literature is still not completely satisfying. The situation is more complex for the ^{18}O(p,α)^{15}N, for which an interference pattern between at least three resonances dominates the reaction rate at the temperatures of interest.
This thesis work concerns an experimental campaign aimed at measuring both reactions at energies of astrophysical interest. These challenging measurements were performed by exploiting the low radiation background at the underground LUNA accelerator in Gran Sasso Laboratories, Italy. The two reactions were investigated in direct kinematics. A proton beam was accelerated onto solid Ta_2O_5 targets and the alpha particles produced were detected at backward angles using an array of silicon detectors mounted in a purpose-built scattering chamber. Our results indicate that the ^{17}O(p,α)^{14}N reaction rate at temperatures of astrophysical interest is approximately a factor of two higher than previously reported, solving a long standing puzzle on the origin of some pre-solar grains. For the ^{18}O(p,α)^{15}N reaction, we find a reaction rate largely in agreement with previous investigations, but with a significantly reduced uncertainty which could help improve the accuracy of stellar models of a number of stellar sites.

Lay Summary

Stars, including our Sun, are powered by nuclear reactions. These nuclear reactions keep the stars shining, while producing most of the elements necessary for life. Nuclear astrophysics is a field of research that aims to study nuclear reactions occurring in stars by performing experiments here on Earth. Improving our knowledge of nuclear reactions allows us answer questions such as how are elements produced, or how do stars evolve and eventually die. This work focussed on convective and recirculating processes that occur in a phase of stellar evolution known as Asymptotic Giant Branch (AGB). In AGB stars, mixing processes transport elements synthesised in the hot stellar cores to the surface, and *vice versa*. Improving our understanding of mixing and convection in AGB stars would in turn improve our understanding of the evolution of all stars that are currently in, or that will enter, the AGB phase, including our own Sun.

It is exceedingly difficult to observe directly what occurs inside a star. A better way to trace mixing processes is to observe the surface abundance of rare, stable isotopes such as ^{17,18}O that are known to be only synthesised in the stellar cores. Accurate predictions of the abundance of ^{17,18}O in the core of a star, paired with direct observations of the ^{17,18}O isotopic abundance on the surface of the same star, would allow us to establish the magnitude and depth of the mixing processes. Very precise direct measurements of surface isotopic abundances in stars can be obtained from so-called "pre-solar grains", tiny remnants of stars pre-dating the birth of our Sun, transported to the Solar System by meteorites. However, model predictions of ^{17,18}O abundances in the core of stars are at present limited by the uncertainty in the destruction rate of ^{17,18}O, *i.e.* by the probability of the two nuclear reactions ^{17,18}O + proton $\rightarrow \alpha +$ ^{14,15}N to occur. The present work involved measuring these two nuclear reactions in a laboratory in order to reduce the current uncertainties in destruction probability of ^{17,18}O.

Previous measurements suggest that the probability of interaction is very small for both reactions. Therefore the signal produced when the reactions occur, *i.e.*

the production of one alpha particle, could have been masked by background radiation of cosmic origin. In order to reduce the background radiation the experiment was performed deep underground at the LUNA-400kV accelerator in the Laboratori Nazionali del Gran Sasso, Italy, located under the Gran Sasso massif. The background reduction afforded by the underground environment allowed us to successfully measure both reactions. Our results shed light on the mixing processes in AGB stars, and helped solving a long-standing puzzle on the isotopic abundances of pre-solar grains.

Declaration

I declare that this thesis was composed by myself, that the work contained herein is my own except where explicitly stated otherwise in the text, and that this work has not been submitted for any other degree or professional qualification except as specified. The experiments described in this thesis were performed by myself and fellow members of the LUNA collaboration.

Parts of this work have been published in

M. Lugaro, A. Karakas, **C.G. Bruno** *et al.*, Nature Astronomy, **1** (2017) 27
O. Straniero, **C.G. Bruno** *et al.*, Astrophys. J., **598** (2017) A128
C.G. Bruno for the LUNA Collaboration, JPS Conf. Proc., **14** (2017) 020401
C.G. Bruno *et al.*, Phys. Rev. Lett., **117** (2016) 142502
A. Boeltzig, **C.G. Bruno** *et al.*, Eur. Phys. J. A **52** (2016) 75
C.G. Bruno for the LUNA Collaboration, JPCS, *accepted* (2016)
C.G. Bruno *et al.*, Eur. Phys. J. A **51** (2015) 94
C.G. Bruno for the LUNA Collaboration, PoS (NIC XIII) (2014) 042
C.G. Bruno for the LUNA Collaboration, AIP Conf. Proc. **1595** (2014) 258
D.A. Scott, **C. Bruno**, A. Caciolli, Nucl. Instr. Meth. Phys. A, **718** (2013) 481
C.G. Bruno, Master Thesis, Università degli Studi di Milano (2013)

(Carlo Giulio Bruno, July 2017)

Acknowledgements

First and foremost I thank my supervisors, Marialuisa Aliotta and Tom Davinson, whom I am greatly indebted to for all the support and guidance they provided throughout my studies at Edinburgh.

I thank the members of the LUNA Collaboration, and in particular Alba Formicola, for the help provided during the data taking in Gran Sasso. I also thank Pierre Descouvemont for the invaluable discussions on the R matrix technique and for his hospitality in Brussels. Thank you David, for the 'memorable' shifts underground, as you called them.

Thanks also goes to the staff and students of the Edinburgh University Nuclear Physics Group for making my time in Edinburgh be so enjoyable. I am extremely grateful for your friendship and support.

Finally, I thank my parents, Mara and Vito, for their constant support.

Contents

Chapter 1

Astrophysical introduction

This chapter briefly describes the evolutionary stages of single stars as well as the mixing processes that transport matter from the hot stellar cores to the cooler surfaces, following the approach of refs. [1, 2, 3]. Some of these mixing processes can be studied and traced using the isotopic abundances of the rare, stable ^{17,18}O isotopes which are strongly influenced by the ^{17,18}O(p,α)^{14,15}N nuclear reactions. Improving our understanding of mixing processes in single stars, in particular Asymptotic Giant Branch (AGB) stars, through the experimental study of the ^{17,18}O(p,α)^{14,15}N nuclear reactions was the primary motivation of this thesis work.

1.1 Stellar evolution of single stars

Stars originate from the gravitational collapse of interstellar gas clouds and consist mainly of hydrogen and helium. The density and the temperature of the gas increase during the collapse, and if the initial mass is sufficiently large ($M \geq 0.013 M_{\odot}$) [1] temperatures as high as a few million Kelvin can be reached, triggering thermonuclear fusion reactions. A star reaches hydrostatic equilibrium when the thermal pressure due to the energy liberated by the nuclear reactions balances the gravitational attraction. The evolutionary path that the star follows from this point on largely depends on its mass. In general, the larger the mass, the greater the temperature reached before hydrostatic equilibrium is attained and the heavier the nuclei that can be fused to generate energy.

1.1.1 Hydrogen burning

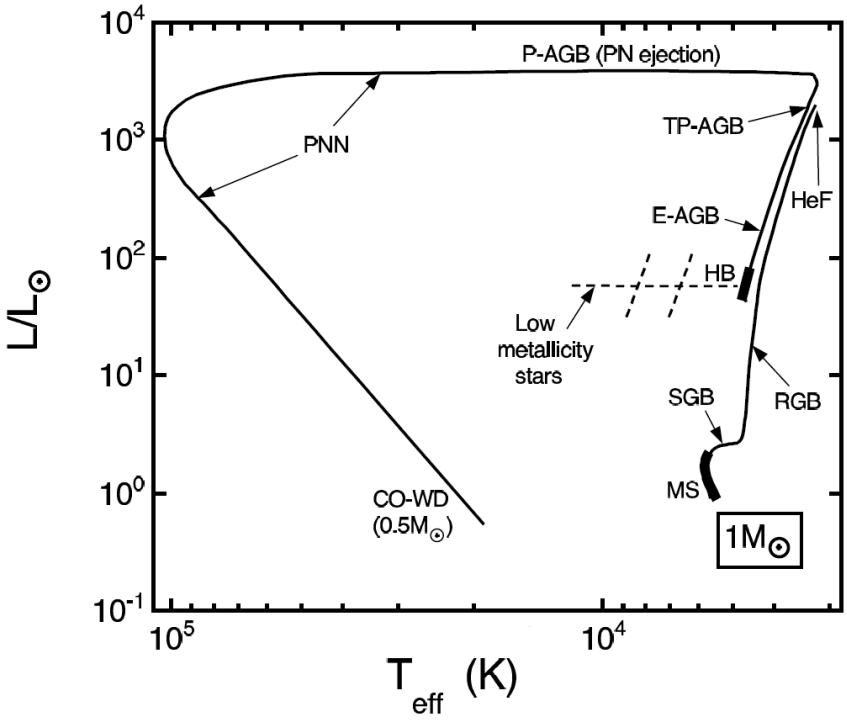

Figure 1.1 *Schematic evolutionary track of the Sun in the Hertzsprung-Russel Diagram. Adapted from ref. [1]. See text for acronyms and details.*

Stars with masses close to that of our Sun ($0.4M_\odot \leq M \leq 2M_\odot$) follow a complex evolutionary path consisting of several stages [1] (Fig. 1.1). Energy production during the main sequence (MS – Fig. 1.1) phase occurs primarily through hydrogen burning in the central part of the star. Specifically, in stars with masses below $1.5M_\odot$ energy production is dominated by the pp nuclear reaction chains, while in more massive stars the CNO cycles dominates. The first pp chain consists of the reactions

$$\mathrm{p(p,\gamma)^2He(\beta^+\nu_e)^2H(p,\gamma)^3He(^3He,\alpha)d}$$

where p is a proton and α is a ^{4}He nucleus. The CNO-I cycle consists instead of the reactions

$$\mathrm{^{12}C(p,\gamma)^{13}N(\beta^+\nu_e)^{13}C(p,\gamma)^{14}N(p,\gamma)^{15}O(\beta^+\nu_e)^{15}N(p,\alpha)^{12}C}$$

Note that in both cases the net result is the fusion of four protons to form an

alpha particle, two positrons and two electron neutrinos. The pp chain and the CNO cycle have a different dependency on the stellar temperature. At low temperatures (low stellar masses), protons do not possess enough energy to overcome the hindering effect of the large Coulomb barriers of the C, N, O isotopes (Z=6–8); nuclear fusion can only progress through reactions between H and He (Z=1–2). On the other hand, at temperatures ($T \geq 3 \times 10^7$ K) reached by stars with masses $M \geq 1.5 M_{\odot}$, the proton energies are sufficient to tunnel through the Coulomb barrier of the C, N, O isotopes which act as reaction catalysts, resulting in faster hydrogen burning compared to the pp chain.

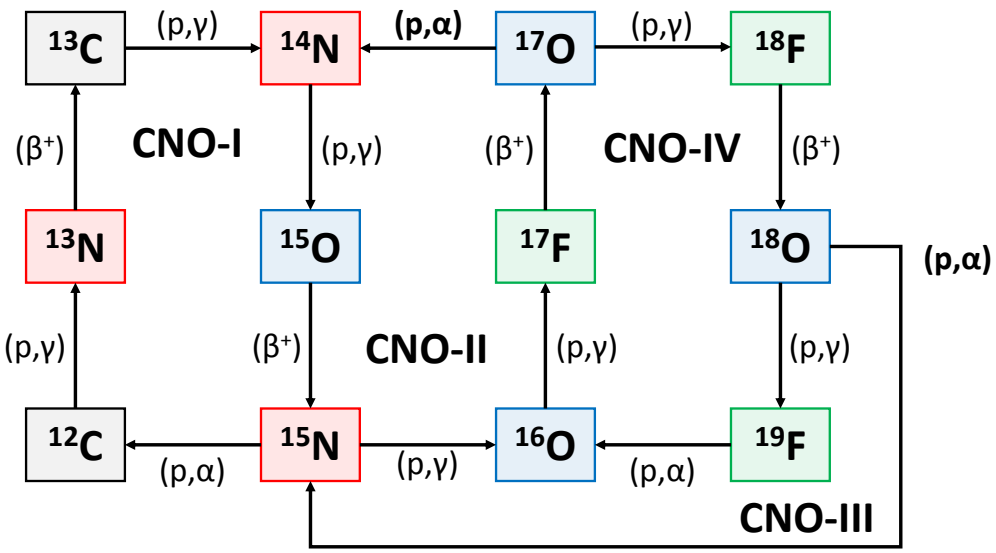

Figure 1.2 *Diagram of the four CNO cycles. The $^{17}O(p,\alpha)^{14}N$ reaction is at the branching point between CNO-II and CNO-III/IV, while the $^{18}O(p,\alpha)^{15}N$ reaction is at the branching point between CNO-III and CNO-IV.*

In addition to energy production, the pp chain and the CNO cycle play a significant role in the synthesis of new elements. The first pp chain and the CNO-I cycle presented above are the most likely reaction paths, but other, less likely reaction chains fusing four protons to give an alpha particle are also possible. In particular, Fig. 1.2 shows the four CNO cycles in which the ^{17,18}O(p,α)^{14,15}N nuclear reactions take part. The probability of a given nuclear reaction being triggered is crucial to predict the isotopic abundances of all the isotopes involved in a reaction network. For instance, during the operation of the CNO-II cycle the ^{17}O(p,α)^{14}N and the ^{17}O(p,γ)^{18}F reactions are in competition with one another. If the (p,α) process occurs, nitrogen is produced and the reactions will continue

following the CNO-II cycle. However, if the (p,γ) process is triggered, fluorine is produced and the cycle may continue along CNO-III or CNO-IV, enriching the star in fluorine and depleting it of carbon. More information on how the two ^{17,18}O(p,α)^{14,15}N nuclear reactions specifically influence the isotopic abundances of elements in AGB stars is given in section 1.2.

1.1.2 Helium burning

After the hydrogen in the stellar core has been burned via the pp chain or the CNO cycle, a star contracts as the gravitational energy is no longer balanced by the thermal pressure [1]. Hydrogen starts burning in a thick shell around the helium core and the star leaves the main sequence and enters the Sub-Giant Branch (SGB – Fig. 1.1). Convection processes become increasingly significant in the stellar envelope around the core. When the envelope becomes fully convective the star leaves the SGB to enter the Red Giant Branch (RGB – Fig. 1.1) and starts to experience significant mass loss due to stellar winds. The lost mass is injected into the interstellar medium where it may either be captured by another stellar site, or be preserved inside meteorites [4, 5]. This second scenario is one of the possible origins of the so-called pre-solar grains, cosmic dust that bears the isotopic signature of the star where it was produced. More details on the wealth of information that can be deduced from these pre-solar grains are given in ref. [4] and references therein.
During the RGB phase the core contracts and reaches such high densities that matter becomes electron degenerate [1]. The convective envelope deepens until matter from the outer part of the core is brought to the surface in a process known as first dredge up. Eventually, the temperature of the star becomes sufficient to ignite helium burning in the core. The energy generation rate increases, but because the electrons in the core are degenerate, the increase in temperature does not reduce the core density as it would for an ideal gas. Instead, the temperature keeps increasing causing even higher energy generation, eventually leading to a thermonuclear runaway known as a core Helium Flash (HeF – Fig. 1.1) which lifts the electron degeneracy of the core. The core expands and starts slowly burning helium as the star enters the Horizontal Branch (HB – Fig. 1.1). When the helium in the core is exhausted, the core contracts and helium burning starts in the shell outside the core while hydrogen ignites in a shell surrounding the helium-burning region [1]. The star is now in the early asymptotic giant branch phase (E-AGB – Fig. 1.1) of its evolution. Hydrogen burning provides the nuclear energy for

about 90% of the time, producing helium which increases the mass of the helium-burning region. The density and temperature of the helium shell region keep increasing, until another thermonuclear runaway occurs. The release of energy expands the star, cooling down the hydrogen-burning shell until it stops burning. Eventually, the helium burning shell cannot sustain the expansion anymore and the star contracts, restarting the hydrogen burning. This cycle is known as a thermal pulse and keeps repeating as the star reaches the thermally pulsing AGB phase (TP-AGB – Fig. 1.1). Thermal pulses cause significant variations in the radius of the star and very large amounts of mass are lost to stellar winds [1], producing more cosmic dust. During each thermal pulse, the convective envelope reaches deep inside the helium ashes and transports matter to the surface in a process known as the third dredge up[1]. Thermal pulses cease and the star enters the post-AGB phase (P-AGB – Fig. 1.1), shedding outer layers as the bright, hot inner layers are uncovered. Eventually, the surface becomes hot enough to ionise the expanding ejecta which begin to fluoresce becoming a planetary nebula (PN). The residual core becomes a planetary nebula nucleus (PNN – Fig. 1.1). The final destiny of a star depends on its mass and isotopic composition. For our Sun, it is currently accepted [1] that when all the hydrogen is exhausted it will transform in a carbon-oxygen white dwarf (CO-WD – 1.1), having lost approximately half of its initial mass.

The evolution of stars with masses $2M_{\odot} \leq M \leq 9M_{\odot}$ proceeds along stages which are qualitatively similar to those just described. In general, the more massive the star, the higher the temperatures reached and the heavier the nuclei which can be fused. The probability of interaction between nuclei increases with energy, therefore more massive stars which reach higher temperatures burn nuclear fuel faster and have shorter lives.

1.2 Mixing processes in AGB stars

Experimental evidence and stellar models [6, 7, 8, 9] suggest that the convection processes described in the previous section, including the three dredge-up episodes, are not the only mixing processes taking place in AGB stars. Our imperfect knowledge of some of these mixing processes [10] affects the precision of our predictions of the evolutionary paths taken by stars that are, or will enter, the

[1]The second dredge-up is a mixing process that occurs at the onset of the E-AGB phase, but only in stars with $M \geq 4M_{\odot}$. Stars with masses $M \leq 4M_{\odot}$ have only the first and third dredge ups.

AGB phase, including our own Sun [1]. In particular, one of the most important recirculating processes in massive ($M \geq 4M_{\odot}$) AGBs is the so-called Hot Bottom Burning (HBB – Fig. 1.3) [7, 9] that occurs when the base of the convective envelope of an AGB star becomes sufficiently hot for hydrogen burning to occur through the CNO cycle [4]. HBB has several important effects on the expected isotopic abundances and the evolution of a star, which are largely beyond the scope of this work (see instead refs. [4, 5, 7, 9] and references therein).
The ashes of HBB hydrogen burning are brought to the surface by the convective envelope and for this reason cosmic dust originating from the surface of massive AGB stars should show the isotopic signature of CNO processing. While current models suggest that massive AGB stars produce significant amounts of cosmic dust [4], no pre-solar grains have been found matching the expected isotopic signature. The most obvious candidates are the oxygen-rich Group II grains which, however, show ^{17}O abundances approximately a factor of two lower than expected from models [5, 4] and are tentatively associated with another production site as detailed at the end of this section. One possible solution to this missing dust puzzle could be a revision of the nuclear reaction rates that influence the abundance of ^{17}O and in particular the ^{17}O(p,α)^{14}N reaction [5], which was one of the key motivations of this thesis.

Currently, Group II grains are thought to be produced in low mass ($M \leq 1.5M_{\odot}$) AGB stars that are influenced by the so-called Cool Bottom Process (CBP Fig. 1.3). Material from the bottom of the convective envelope penetrates the thin radiative region located between the base of the convective envelope and the top of the hydrogen burning shell [6, 8]. The physical nature of CBP is still unclear and several possibilities have been proposed including rotation, magnetic buoyancy, gravity waves and thermohaline circulation (ref. [10] and references therein). At present CBP is treated in a parametric way, in other words the rate and depth of extra mixing are treated as free parameters and optimised *ad hoc* to match experimental observations [4]. This is the reason why, even though in principle Group II grain abundances can be matched invoking CBP, the solution is only tentative.
In spite of being poorly understood, CBP is invoked in RGBs as well as in AGBs [10]. Therefore, a better understanding of the physical nature, or at least the magnitude, of CBP would significantly improve the reliability of our stellar models. Stable isotopes such as ^{17,18}O can be used as tracers to follow the extra mixing processes by comparing isotopic abundances from model predictions with experimental observations [10, 6, 8]. The abundances of the tracer isotopes

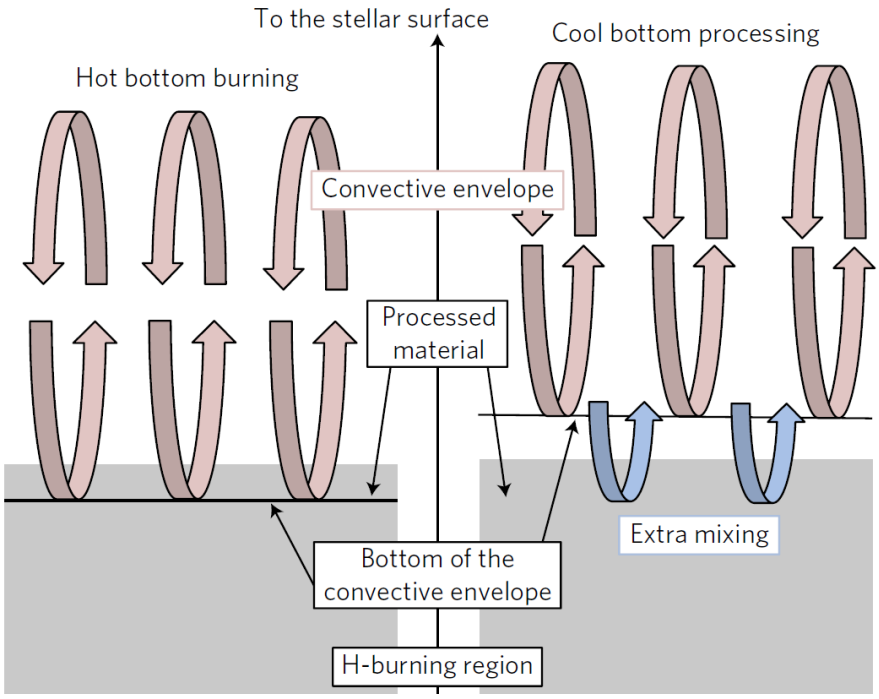

Figure 1.3 *Schematic of the internal structure of AGB stars at the interface between H-burning region and the convective envelope. Adepted from ref. [4]. See text for details.*

^{17,18}O are currently affected by the uncertainties in the reaction rates of the ^{17,18}O(p,α)^{14,15}N nuclear reactions at the relevant astrophysical temperatures [5, 4]. This was another key motivation for the present study.

Chapter 2

Nuclear physics framework

This chapter presents the theoretical framework used in this thesis to deduce the properties of nuclear reactions in stars from experimental measurements on Earth. In particular, the aim of this chapter is to show how to obtain a stellar reaction rate from a nuclear physics experiment.

2.1 Basic definitions

Nuclear reactions are quantum phenomena, and have a certain probability of occurring under given conditions. In particular, for reactions happening in a laboratory where a beam is accelerated onto a target, it is useful to introduce a quantity known as the cross section σ

$$\sigma = \frac{N_R}{N_T N_B} \tag{2.1}$$

where N_R is the total number of reactions that took place, N_T is the number of target nuclei interacting with the beam and N_B is the number of beam particles that were accelerated on the target. N_R and N_B are pure numbers, while N_T is usually measured in atoms/cm^2 or equivalently atoms/barn where 1 barn = 10^{-24} cm^2. Therefore the cross-section has the dimensions of an area, unlike a probability. The cross-section depends in general on the relative energy of the projectile and the target, i.e. $\sigma = \sigma(E_{\mathrm{CM}})$ where E_{CM} is the energy of the projectile-target system in the centre-of-mass (CM) reference frame. Equivalently,

if we consider the target to be at rest, we can write $\sigma = \sigma(E_{\mathrm{b}})$, where E_{b} is the energy of the beam in the laboratory frame. However since projectiles generally lose energy in the target, the reaction does not occur at a single energy but in an energy range. Because of energy loss, Eq. 2.1 cannot be immediately related to measurable experimental quantities. What one obtains from a laboratory measurement is instead the yield Y

$$Y(E_b) = \frac{N_R}{N_B} = \int_{E_{\mathrm{b}}-\Delta E}^{E_{\mathrm{b}}} \frac{\sigma(E)}{\epsilon(E)} dE \tag{2.2}$$

where ΔE is the energy loss of the beam in the target, expressed in energy units (e.g. eV), ϵ is the stopping power and E is the laboratory energy. The stopping power is defined as the energy loss of the projectile in some units, typically either energy per unit length (e.g. eV/nm) or energy per atomic density (e.g. eV/(10^{15}atoms/cm^2)). The stopping power is in general known with some uncertainty from models and measurements, and can be readily calculated with programs such as SRIM/TRIM [11]. In case a target contains several isotopes, one can use instead the effective stopping power ϵ_{eff}

$$\epsilon_{\mathrm{eff}} = \left(\epsilon_t + \sum_i^N \epsilon_i \frac{n_i}{n_t} \right) \tag{2.3}$$

where ϵ_t is the stopping power for the target nucleus, on which the reaction of interest occurs, ϵ_i are the stopping power for the N nuclei other than the target nucleus, and n_t and n_i are the number densities for the target nucleus and the nucleus i respectively. One of the main difficulties in obtaining a cross-section is that in Eq. 2.2 the cross-section appears inside an integral. In order to obtain a cross-section one usually needs to deconvolve the integral in Eq. 2.2. Sections 2.2 and 2.3 describe a few ways in which this deconvolution can be either performed or side-stepped.

In order to obtain a yield from an experimental measurement, one has to account for the efficiency η of the experimental set-up, that is to say how many reactions were detected (N_D) out of those which occurred (N_R). In this work, the efficiency η is defined for an isotropic reaction in the CM frame. Some reactions, however, do not emit products isotropically. There are two possible solutions in this case. If the angular distribution is known, a correction factor W can be introduced. W is expressed in Legendre polynomials and can be calculated explicitly using e.g.

R-matrix theory (see later). In this case the yield is obtained as

$$Y = \frac{N_R}{N_B} = \frac{N_D}{N_B \eta W} \tag{2.4}$$

where all the quantities on the right-hand side can be directly measured or calculated. If the angular distribution is not known, or not reliable, one can define instead a *differential* cross-section, $d\sigma/d\Omega$

$$\frac{d\sigma}{d\Omega} = \frac{Y}{N_T d\Omega} = \frac{N_D}{N_T N_B \eta d\Omega} \tag{2.5}$$

where $d\Omega$ is the solid angle covered by the detector(s). One assumes that the probability of emission is constant across $d\Omega$. Note η is still the efficiency, but now refers to the number of particles emitted at a solid angle $d\Omega$ over those detected.

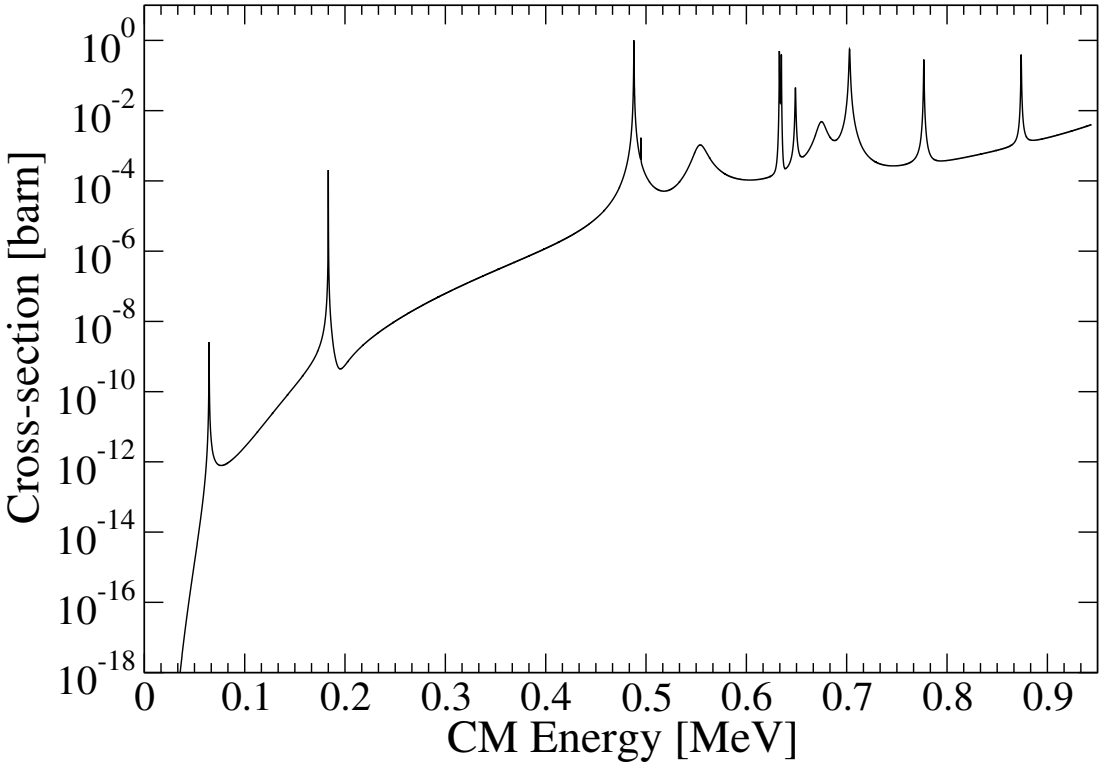

Figure 2.1 *An R-matrix calculation of the cross-section of the $^{17}O(p,\alpha)^{14}N$ reaction. Several resonances are present in the energy range shown. Note the logarithmic scale on the y-axis.*

Cross-sections are generally not smooth but may present resonances. In the simplest case these resonances appear as peaks over a smooth contribution

decreasing with energy. However, more complex interferences can also take place. See Fig. 2.1 and section 2.4.3. From a physical point of view, resonances occur when a compound nucleus is formed during the reaction. If the total energy of the initial projectile-target system is close to the energy of a state in the compound nucleus, a resonance may be present. Resonances have a width Γ as shown in Fig. 2.1. This width has a lower bound, given by the indeterminacy in the energy of the state, and an upper bound given by Wigner's limit [3]. It is important to note that resonances can increase the cross-section significantly, and often play a central role when calculating the stellar reaction rate (see section 2.6). In the presence of resonances, cross-sections are difficult to model using simple analytical expressions. Extrapolating and interpolating is also potentially dangerous if undetected resonances of unknown energy are present in the relevant energy range. One way to approach this problem is the (phenomenological) R-matrix theory. This tool, detailed in section 2.4, will be used in this work to describe a reaction - and in particular the reaction's cross-section - using a small number of physically meaningful parameters. Once a cross-section has been extracted from a yield and has been described using either the R-matrix technique or another equivalent approach, one can use the parameters obtained in order to compute the stellar reaction rate, as described in section 2.6.

2.2 Deconvolution - special cases

There are a few special situations in which a full deconvolution of Eq. 2.2 is not required in order to obtain quantities of astrophysical interest. This section covers two such situations that will be relevant in the following chapters.

2.2.1 Thin-target yield

Let us consider Eq. 2.2. If the cross-section $\sigma(E)$ and the stopping power $\epsilon_{\text{eff}}(E)$ are approximately constant over the integration range $E_\text{b} - \Delta E$ to E_b one may write

$$Y = \int_{E_\text{b}-\Delta E}^{E_\text{b}} \frac{\sigma(E)}{\epsilon(E)} dE = \frac{\sigma(E_\text{b} - \frac{\Delta E}{2})}{\epsilon(E_\text{b} - \frac{\Delta E}{2})} \int_{E_\text{b}-\Delta E}^{E_\text{b}} dE = \frac{\sigma(E_\text{b} - \frac{\Delta E}{2})}{\epsilon(E_\text{b} - \frac{\Delta E}{2})} \Delta E \qquad (2.6)$$

where the energy at which the integral is evaluated is historically [1, 2, 3] set to the mean energy $E_\mathrm{b} - \frac{\Delta E}{2}$ in order to improve the quality of the approximation. Note that if the cross-section and the stopping power are approximately constant over the range of the integral in Eq. 2.6, since the cross-section depends strongly on the interaction energy it must follow $E_\mathrm{b} \simeq E_\mathrm{b} - \Delta E$, or equivalently $\Delta E \ll E_\mathrm{b}$. Therefore, the choice of energy is not critical. The main weakness of the thin-target yield approximation is that it does not work at energies close to those of narrow, intense resonances. Here the cross-section may vary significantly in the energy range of the integral in Eq. 2.6, even for targets that are "thin" at other, non-resonant energies. Very narrow resonances of this kind exist both in the ^{17}O(p,α)^{14}N and the ^{18}O(p,α)^{15}N reactions (see later chapters). Fig. 2.2 shows an example of the thin-target yield applied to yields simulated for different target thickness values. For very thin (10^{16} atoms/cm^2, red dots) targets, the approximation works well both at resonant energies and at non-resonant ones. For thicker targets (10^{17} atoms/cm^2, green squares) the thin-target yield approximation still works well at non-resonant energies, but breaks down near resonances. Finally, using the thin-target yield approximation on very thick targets (10^{18} atoms/cm^2) can result in an incorrect cross-section assignment in a wide energy range. Note the energy assigned to the experimental measurement ($E_b - \frac{\Delta E}{2}$) is also incorrect for targets that are too thick.

2.2.2 Thick-target yield approach for resonances

Another standard [1, 2, 3] approach is the so-called "thick-target yield" approximation. This approximation can be used for narrow, isolated resonances for which the resonance width Γ is significantly smaller than the energy loss in the CM frame ($\Gamma \ll \Delta E_\mathrm{CM}$). According to R-matrix theory (see section 2.4), a narrow and isolated resonance can be described using the so-called one-level Breit-Wigner (or Lorentzian) curve

$$\sigma_\mathrm{BW}(E) = \frac{\lambda^2}{4\pi} \frac{(2J+1)(1+\delta_{01})}{(2j_0+1)(2j_1+1)} \frac{\Gamma_a \Gamma_b}{(E_\mathrm{r}-E)^2 + \Gamma^2/4} \tag{2.7}$$

where λ is de Broglie's wavelength, J and E_r are the spin and energy of the resonance, Γ_i are the partial widths of the entrance and exit channels[1], Γ is the total width, $j_{0,1}$ are the spins of the target and projectile nucleus respectively,

[1] See section 2.4 for the formal definition of a channel.

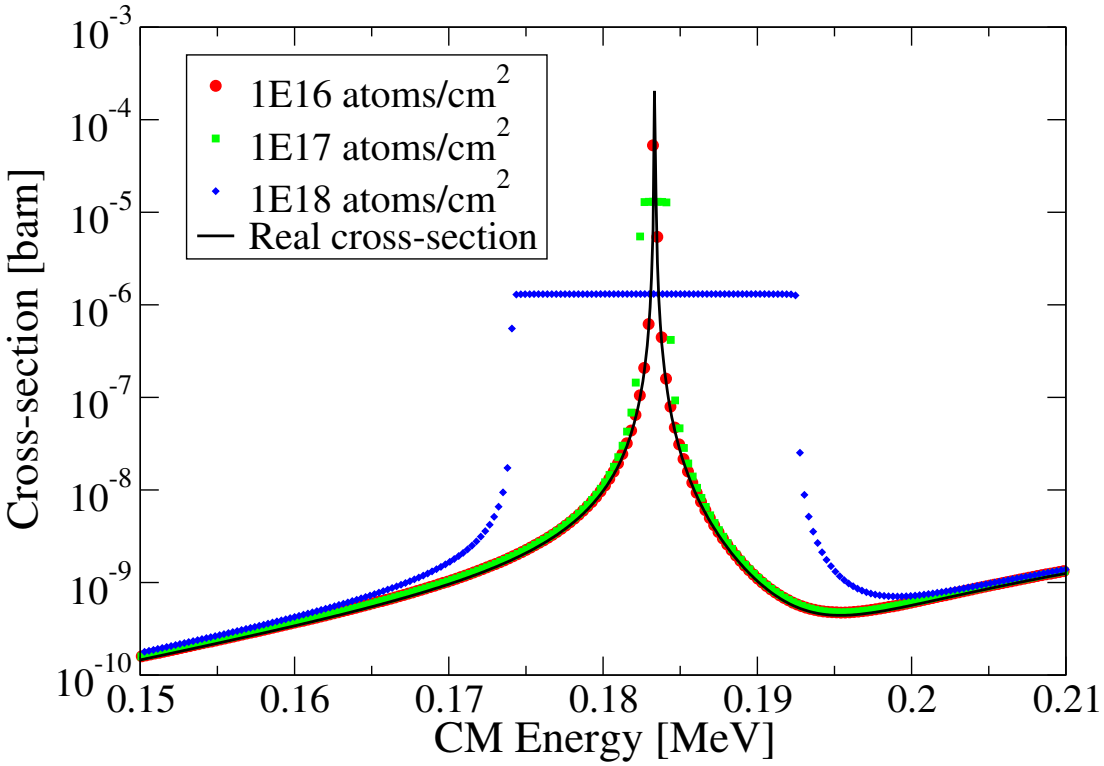

Figure 2.2 *The thin-target yield approximation applied to three simulated datasets obtained with three different target thickness values of $N_T = 10^{16}$ (red dot), 10^{17} (green square), and 10^{18} (blue diamond) atoms/cm^2. The black line shows the real cross-section used to generate the data. The approximation works well on thin target data, but is unsuited for thick target data or near resonances.*

and δ_{01} is the Kronecker delta. All quantities are given in the CM frame. This approximation has been tested experimentally and is considered to be very reliable [2]. Following ref. [2], one can replace Eq. 2.7 into Eq. 2.2 obtaining

$$\begin{aligned} Y(E_0) &= \int_{E_0-\Delta E}^{E_0} \frac{1}{\epsilon(E)} \frac{\lambda^2}{4\pi} \frac{(2J+1)(1+\delta_{01})}{(2j_0+1)(2j_1+1)} \frac{\Gamma_a \Gamma_b}{(E_\mathrm{r}-E)^2+\Gamma^2/4} dE \\ &= \int_{E_0-\Delta E}^{E_0} \frac{1}{\epsilon(E)} \frac{\lambda^2}{4\pi} \omega \frac{\Gamma_a \Gamma_b}{(E_\mathrm{r}-E)^2+\Gamma^2/4} dE \\ &= \frac{\lambda_r^2}{2\pi} \frac{\omega\gamma}{\epsilon_r} \frac{\Gamma}{2} \int_{E_0-\Delta E}^{E_0} \frac{dE}{(E_\mathrm{r}-E)^2+(\Gamma/2)^2} \\ &= \frac{\lambda_r^2}{2\pi} \frac{\omega\gamma}{\epsilon_r} \left[\arctan\left(\frac{E_0-E_\mathrm{r}}{\Gamma/2}\right) - \arctan\left(\frac{E_0-E_\mathrm{r}-\Delta E}{\Gamma/2}\right) \right] \end{aligned} \tag{2.8}$$

where E_0 is the interaction energy in the CM frame, $\omega = \dfrac{(2J+1)(1+\delta_{01})}{(2j_0+1)(2j_1+1)}$, $\gamma =$

$\frac{\Gamma_a\Gamma_b}{\Gamma}$, λ_r and ϵ_r are respectively de Broglie's wavelength and the stopping power at the resonant energy E_r. While Eq. 2.8 may look complex, it is straightforward to find its maximum ($E_0 = E_r$)

$$Y_{max} = \frac{\lambda_r^2}{\pi}\frac{\omega\gamma}{\epsilon_r}\arctan\left(\frac{\Delta E}{\Gamma}\right) \tag{2.9}$$

and if $\Delta E_{\mathrm{CM}} \gg \Gamma$ then

$$\omega\gamma = Y_{\max}\frac{2}{\lambda_r^2}\epsilon_r \tag{2.10}$$

where $\omega\gamma$ is known as the resonance strength. This resonance strength is given in the CM frame and therefore the quantities that appear in Eq. 2.10 are calculated in the CM frame. Critically, note that $\omega\gamma$ does not depend on the shape of the resonance, but only on the yield at its maximum. If one knows the spin-parities of the states involved in the resonance, then one can readily obtain $\gamma = \Gamma_a\Gamma_b/\Gamma$ from an experimental measurement. The width of a state can be used to calculate the stellar reaction rate, as explained in sections 2.4 and 2.6. Thus the thick-target yield approach side-steps the problem of deconvolving the cross-section.

It is worth noting that Eq. 2.10 is not used experimentally. To account for efficiency and effective stopping power, one substitutes Eq. 2.3 in Eq. 2.10

$$\omega\gamma = \frac{N_D}{N_B\eta W}\frac{2}{\lambda_r^2}\epsilon_r^{\mathrm{eff}} \tag{2.11}$$

One of the main strengths of this technique is that, if $\Delta E_{\mathrm{CM}} \gg \Gamma$, the yield distribution is flat in the energy range around Y_{max}. That means the precise resonant energy is not needed to extract a resonance strength. If the $\Delta E_{\mathrm{CM}} \gg \Gamma$ condition is not met, one can simply fit Eq. 2.8. One of the main drawbacks of the thick-target yield approach is that it does not result in a cross-section, and it can only be applied to narrow and isolated resonances. Neither the thin-target yield approximation nor the thick-target yield approach work at energies close to resonances or for cross-sections dominated by interference patterns. A more general approach is therefore required.

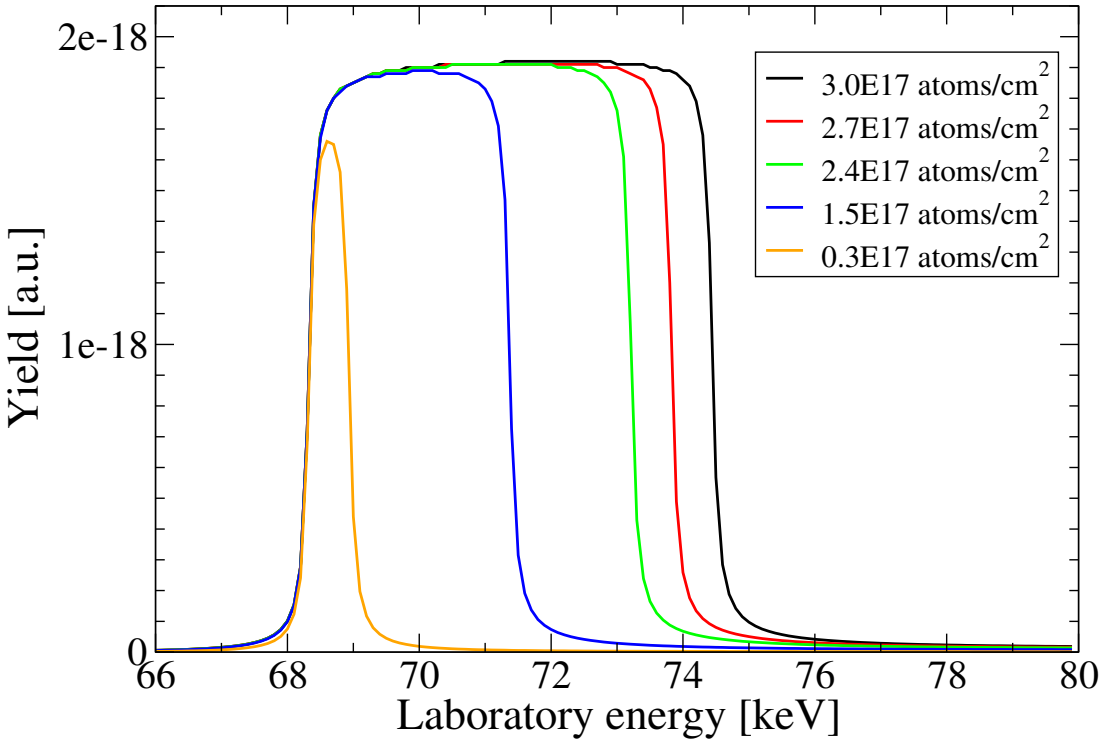

Figure 2.3 *The yield of the E_p = 70 keV resonance in the $^{17}O(p,\alpha)^{14}N$ reaction in thick-target yield conditions, for different target thickness values. The height of the plateau does not depend on the thickness of the target as long as the target is sufficiently thick (¿1.5×10^{17} atoms/cm^2 in this case).*

2.3 Deconvolution - a general approach

There are a few general approaches to the problem of extracting (de-convolving) the cross-section from the yield. Some of these techniques, known as the "effective energy" approach as well as the "mean energy" or "median energy" approach, have been used for decades. A recent paper [12] briefly reviews the history of these methods and shows that the median energy definition proposed in [3] and [1] is incorrect. The authors propose some corrections to the classical definitions that allow, in their words, a "faithful mathematical deconvolution" of the yield into a cross-section. Thanks to these corrections, they are also able to show that these three techniques are just special cases of a general approach. As part of this work, I developed a program that employs the new, general approach of ref. [12] to extract a cross-section from the yield data. In this section I will briefly explain how I made use of the formalism sketched in ref. [12] as well as making explicit some of the steps and assumptions of the mathematical derivation proposed in that work.

2.3.1 Deconvolution strategy

The aim of this general approach is to rewrite Eq. 2.2 as follows

$$Y(E_b) = \int_{E_b-\Delta E}^{E_b} \frac{\sigma_{\rm ex}(E)}{\epsilon_{\rm eff}(E)} dE = \sigma_{\rm ex}(\tilde{E}) f \int_{E_b-\Delta E}^{E_b} \frac{1}{\epsilon_{\rm eff}(E)} dE \tag{2.12}$$

where $\sigma_{\rm ex}$ is now explicitly the cross-section obtained from the experimental measurement, and f is the correction factor proposed in ref. [12]. $\tilde{E}$ does not have a name in ref. [12], and is the energy assigned to the experimental data point. It will be called "assigned energy" in this work. It makes physical sense for the assigned energy $\tilde{E}$ to be inside the energy range of the integral in Eq. 2.12, but this is not mathematically required. The definition of the assigned energy is arbitrary: it can be the mean energy, median energy, effective energy, or any other definition. The definition of the correction factor f is

$$f = \frac{\int_{E_b-\Delta E}^{E_b} \frac{\sigma_{\rm pr}(E)}{\epsilon_{\rm eff}(E)} dE}{\sigma_{\rm pr}(\tilde{E}) \int_{E_b-\Delta E}^{E_b} \frac{1}{\epsilon_{\rm eff}(E)} dE} \tag{2.13}$$

where $\sigma_{\rm pr}$ is a prior cross-section. In general one may obtain this prior cross-section from a theoretical estimate, another measurement of the same cross-section or even from a technique such as the thin-target yield approximation. Note ref. [12] ignores the difference between the prior and the experimental cross-section in the derivation. However, this difference is quite important. If one substitutes Eq. 2.13 in Eq. 2.12 one gets

$$\begin{aligned} Y(E_b) = \int \frac{\sigma_{\rm ex}(E)}{\epsilon_{\rm eff}(E)} = \sigma_{\rm ex}(\tilde{E}) \frac{\int \frac{\sigma_{\rm pr}(E)}{\epsilon_{\rm eff}(E)}}{\sigma_{\rm pr}(\tilde{E}) \int \frac{1}{\epsilon_{\rm eff}(E)}} \int \frac{1}{\epsilon_{\rm eff}(E)} = \\ = \frac{\sigma_{\rm ex}(\tilde{E})}{\sigma_{\rm pr}(\tilde{E})} \int \frac{\sigma_{\rm pr}(E)}{\epsilon_{\rm eff}(E)} = \frac{\sigma_{\rm ex}(\tilde{E}) \int \frac{\sigma_{\rm pr}(E)}{\epsilon_{\rm eff}(E)}}{\sigma_{\rm pr}(\tilde{E}) \int \frac{\sigma_{\rm ex}(E)}{\epsilon_{\rm eff}(E)}} \int \frac{\sigma_{\rm ex}(E)}{\epsilon_{\rm eff}(E)} = M \int \frac{\sigma_{\rm ex}(E)}{\epsilon_{\rm eff}(E)} \end{aligned} \tag{2.14}$$

where integration limits have been omitted for clarity. Eq. 2.14 holds if

$$M = \frac{\sigma_{\rm ex}(\tilde{E}) \int \frac{\sigma_{\rm pr}(E)}{\epsilon_{\rm eff}(E)}}{\sigma_{\rm pr}(\tilde{E}) \int \frac{\sigma_{\rm ex}(E)}{\epsilon_{\rm eff}(E)}} = 1 \tag{2.15}$$

which is trivially true if the prior and the experimental cross-sections are the same, that is the implicit assumption made in ref. [12]. In that reference, the authors suggest iterating until convergence is reached, however no quantitative test of this convergence is proposed. Here, iterating means iteratively substituting the prior cross-section with that obtained from the deconvolution. The factor M defined in Eq. 2.15 will be used in this work as a figure of merit for the convergence of the deconvolution. If the experimental and the prior cross-section are sufficiently similar, it follows $M \simeq 1$ and the cross-section obtained from the experimental yield data is an approximately "faithful" deconvolution in the sense of ref. [12].

2.3.2 Effective energy

As an example, let us see what happens if the assigned energy is the effective energy. The effective energy $E_{\rm eff}$ is defined implicitly as

$$\int_{E_b-\Delta E}^{E_b} \frac{\sigma_{\rm pr}(E)}{\epsilon_{\rm eff}(E)} dE = \sigma_{\rm pr}(E_{\rm eff}) \int_{E_b-\Delta E}^{E_b} \frac{1}{\epsilon_{\rm eff}(E)} \tag{2.16}$$

Using Eq. 2.16 one may rewrite Eq. 2.12 as

$$Y(E_b) = \int_{E_b-\Delta E}^{E_b} \frac{\sigma_{\rm ex}(E)}{\epsilon_{\rm eff}(E)} dE = \sigma_{\rm ex}(E_{\rm eff}) \int_{E_b-\Delta E}^{E_b} \frac{1}{\epsilon_{\rm eff}(E)} dE \tag{2.17}$$

and note in particular that if Eq. 2.15 holds, replacing Eq. 2.16 in Eq. 2.13 yields $f = 1$. That is to say, if the prior and the experimental cross-section are sufficiently similar, no correction factor is required for the effective energy. Because of this property, cross-sections extracted from datasets using the effective energy technique in the past are correct, as long as convergence was reached. That is not true for cross-sections extracted using any other technique (e.g. median energy) for which the f factor is in general different from unity. In spite of

this convenient behaviour, the effective energy approach has some issues, namely its definition is not unambiguous near resonances [12]. A different definition is therefore preferable.

2.3.3 Median energy

The median energy E_m is defined implicitly as

$$\int_{E_b-\Delta E}^{E_b} \frac{\sigma_{\mathrm{pr}}(E)}{\epsilon_{\mathrm{eff}}(E)} dE = 2 \int_{E_m}^{E_b} \frac{\sigma_{\mathrm{pr}}(E)}{\epsilon_{\mathrm{eff}}(E)} dE \tag{2.18}$$

where the two integrals can be readily calculated numerically if one possesses the expression of the prior cross-section. Therefore, for a given beam energy E_b and a given measured yield Y, one first calculates the median energy E_m according to Eq. 2.18 using some prior, and then uses E_m to obtain the cross-section as

$$\sigma_{\mathrm{ex}}(E_m) = \frac{Y(E_b)}{\int_{E_b-\Delta E}^{E_b} \frac{\sigma_{\mathrm{pr}}(E)}{\epsilon_{\mathrm{eff}}(E)} dE} \sigma_{\mathrm{pr}}(E_m) \tag{2.19}$$

where finally all of the quantities on the right side are known. After a few iterations, if $M \simeq 1$, one has deconvolved the cross-section. Unlike the effective energy, the median energy is always well-defined. For its ease of computation, it is one of the definitions recommended by the authors in ref. [12]. In this work, the assigned energy will be obtained as the median energy.

2.4 The R-matrix theory

A full review of the R-matrix theory is beyond the scope of this work. This section provides a summary of the main assumptions and features of this powerful tool, focusing on nuclear physics applications and on those aspects that will play a key role in later chapters. For a recent review of the R-matrix techniqe, see instead ref. [13].

2.4.1 General framework

There are two closely related techniques known as "R-matrix". The calculable R-matrix is a tool to efficiently solve the Shrödinger equation describing scattering states resulting from the interaction of particles or systems of particles - in our case nuclei. The phenomenological R-matrix is instead a tool to parametrize and extrapolate experimental cross-sections employing a small number of physically meaningful parameters. This second version of the R-matrix is the one employed in this thesis.

Both aspects of the R-matrix rely on the same theoretical framework, and in particular on the concept of "channels". Given a many-body system, a channel is a partition of the system where the internal energies of all the parts are specified. For example, given a system that contains nine protons and nine neutrons ^{17}O+p is a possible partition - a possible way to group the particles. A channel is defined by a partition and by the internal energies of the parts. For instance, both the ^{17}O and the proton could be in their ground states. Given the same many-body system some other possible channels are ^{14}N+α, ^{18}F, ^{17}F+n, where all the parts are in their ground states. A channel c has a threshold energy E_c^T equal to the sum of the internal energies E_c^i of the i parts, with respect to some reference energy:

$$E_c^T = \sum_i E_c^i \tag{2.20}$$

A channel is open or closed depending on whether E_c^T is respectively smaller or larger than the total energy E of the system. We will focus only on open channels where the nucleons are divided in two groups.

Let us consider a channel containing two nuclei. To model a scattering process between these two nuclei, one proceeds in the following way. One divides the configuration space into an internal and an external region. The boundary between these two regions is defined by a parameter known as the channel radius. This radius is chosen so that - in the channel being considered - the wave function can be approximated by its asymptotic expression in the external region. In other words the potential $V_{\text{external}} \simeq V_{\text{Coulomb}}$. The Coulomb potential is well-known, unlike the nuclear one. In the internal region the system is confined and the wave function can be expanded there over a discrete basis of eigenstates that can be calculated. Increasing the radius improves the $V_{\text{external}} \simeq V_{\text{Coulomb}}$ approximation,

but it also increases the number of basis eigenstates required in the inner region and thus the complexity of the computation. At the boundary between the two regions, the continuity of the wave function and its derivative are required. The R-matrix is defined as the inverse of the logarithmic derivative of the wave function at the boundary. One can show [13] that in the case of a single channel for an arbitrary partial wave l, this R-matrix R_l takes the form

$$R_l(E) = \sum_{n=1}^{N} \frac{\gamma_{nl}^2}{E_{nl} - E} \tag{2.21}$$

where E is the energy, N is the number of basis eigenstates of the internal region, and γ_{nl}^2 are known as reduced widths. E_{nl} are known as poles and are variational approximations of the exact eigenvalues of the Hamiltonian of the system; in other words, if the system is bound, E_{nl} are the approximate energies of the bound states of the system. Eq. 2.21 is the form generally employed in the calculable R-matrix theory. Note that the size of the R-matrix is equal to the number of channels considered. Since we are only considering one channel here, the R-matrix is just a scalar. In the phenomenological R-matrix theory, traditionally [13], N tends to infinity and one gets

$$R_l(E) = \sum_{n=1}^{\infty} \frac{\gamma_{nl}^2}{E_{nl} - E} \tag{2.22}$$

which looks almost the same as Eq. 2.21. Now, however, E_{nl} are the exact eigenvalues. Note that the R-matrix R_l is the only unknown quantity to obtain the solution to the Scrödinger equation. One can write the solution to the Schrödinger equation in terms of the γ_{nl}, the E_{nl}, and the partial waves l. The partial waves can be determined knowing the spin-parities J^π involved in the process. In the calculable R-matrix, one uses some theoretical assumptions (e.g. a potential, a base for the internal regions) to estimate the unknowns. One calculates the R-matrix according to Eq. 2.21 and then uses it to approximately solve the Schrödinger equation and derive any desired quantity of the system. In the phenomenological R-matrix approach, one optimises the parameters in Eq. 2.22 so that the quantities calculated match experimental observations. In other words, one uses experimental measurements to constrain a parametrised solution to the Schrödinger equation, obtain the wave function, and then calculate any quantity of interest. The strength of the phenomenological R-matrix method

lies primarily in the immediate physical meaning of the unknown parameters, as explained in the next section.

2.4.2 Poles, states and resonances

There are several ways [13] to model the resonant process in the R-matrix theory. Let us take for simplicity a reaction in a single channel (i.e. elastic scattering) with a single pole E_0. The R-matrix takes the form

$$R(E) = \frac{\gamma_0^2}{E_0 - E} \tag{2.23}$$

In R-matrix theory, it can be shown [13] that the phase shift δ [1, 2, 14] can be written as

$$\delta = \phi + \arctan \frac{P(E)R(E)}{1 - S(E)R(E)} \tag{2.24}$$

where ϕ is the hard-sphere phase shift, $S(E)$ is the shift function and $P(E)$ is the penetration function. These three quantities can all be expressed in terms of the regular and irregular Coulomb functions F and G, which are both well-known [13]. Substituting Eq 2.23 in Eq. 2.24 one gets

$$\delta = \phi + \arctan \frac{\gamma_0^2 P(E)}{E_0 - \gamma_0^2 S(E) - E} \tag{2.25}$$

which resembles the Breit-Wigner form of the phase shift

$$\delta^{BW} = \phi + \arctan \frac{\frac{1}{2}\Gamma(E)}{E_{\mathrm{R}} - E} \tag{2.26}$$

and by comparison one defines the resonance energy E_{R}

$$E_{\mathrm{R}} = E_0 - \gamma_0^2 S(E) \tag{2.27}$$

and the resonance width $\Gamma(E)$

$$\Gamma(E) = 2\gamma_0^2 P(E) \tag{2.28}$$

Therefore the energy of a pole E_{nl} in the phenomenological R-matrix theory is connected by a simple relationship to the energy of a given resonance, or equivalently to the energy of a state of the compound nucleus. In the same way, the reduced width γ_{nl}^2 is connected to the width of a state in a given channel, also called the width of the channel. As explained in the previous section, the unknowns in the R-matrix theory are the poles, the reduced widths and the partial waves. Knowing the energies, widths and spin-parities of all resonances in a reaction allows in principle the derivation of all quantities of interest for that reaction. Furthermore, since all of these quantities are associated with states of the compound nucleus, all reactions that produce the same compound nucleus share the same parameters. This allows one to constrain the R-matrix parameters employing different reactions and different channels, greatly reducing the systematic uncertainties.

2.4.3 Interference

Until now, we never considered the case of multiple channels being open at the same time. If two channels are open at the same time, the R-matrix in a given partial wave l can be written as

$$R_{l;c,c'} = \sum_{n=1}^{\infty} \frac{\gamma_{nc}\gamma_{nc'}}{E_n - E} \tag{2.29}$$

where c, c' are matrix element indices and γ_{nc} is the n-th reduced width *amplitude* in channel c. While the reduced widths γ_{nc}^2 can be readily derived from experimental quantities using Eq. 2.28, the reduced width amplitudes cannot. That implies the sign of γ_{nc} cannot be derived directly from experimental observations. This becomes an issue when computing the R-matrix in a system with at least two open channels and two or more resonances having the same J^π value [1, 2]. Depending on the sign, the interference between the two resonances can change significantly. See for instance Fig. 2.4, which shows the cross-section in the two possible cases. The effect is very obvious, and can have a tremendous

influence on the stellar reaction rate. While the sign of this interference cannot be measured *directly*, it can often be inferred *indirectly* based on the shape of the cross-section around the resonant energies of interest.

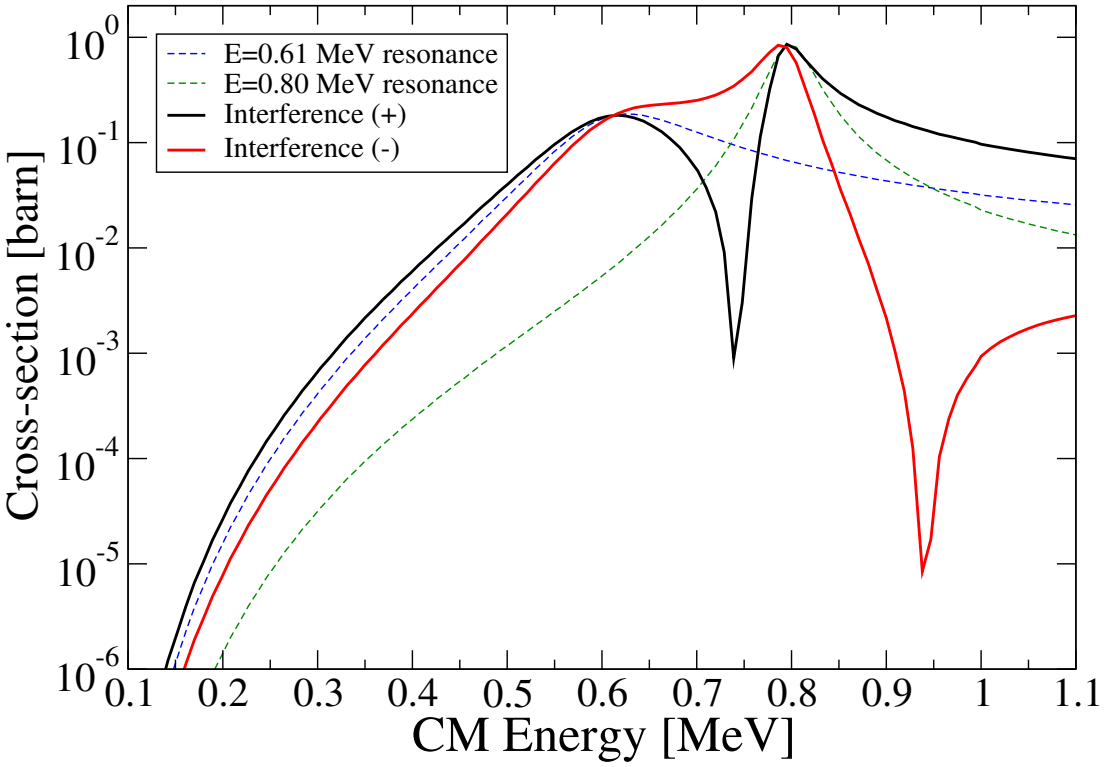

Figure 2.4 *A simple interference between two broad, isolated resonances. Dashed lines show the individual contribution of the two resonances, while the solid black and red lines show the cross-section for the two interference signs. The somewhat symmetric behaviour is due to the $E_n - E$ energy dependence of the poles. Note the choice of sign is significant even at energies far from the two resonances.*

If more than two resonances with the same J^π value are present, more than one interference sign has to be chosen and the situation becomes (significantly) more complex. Finally, note there exist several other ways in which different channels, different resonances or different contributions to the cross-section interfere, or in general sum coherently, in R-matrix theory. However, aside from the interference mechanism described in this section, all other interference processes can be computed without the need of additional input parameters.

2.4.4 Background states

While the phenomenological R-matrix approach is based on Eq. 2.22, it is not experimentally possible to measure all resonances at all energies in a reaction.

However, the phenomenological R-matrix is used to fit data only in a limited energy range of interest. In this sense, the meaning of Eq. 2.22 is that those states which are measured are considered exact eigenstates of the Hamiltonian. Those states which remain unknown are either considered negligible at the energies of interest, or are modelled using so called-background states (or background poles). These background states are non-physical states placed at energies significantly higher than those of interest ($E_n \gg E$), so that one may write

$$\frac{\gamma_n^2}{E_n - E} \simeq \frac{\gamma_n^2}{E_n} = \text{constant} \tag{2.30}$$

that is to say, the contribution of a background state to the R-matrix is constant. Like regular states, background states have a partial wave and may interfere as described in the previous section. One can think of a background state as an effective average of the states which are not experimentally measured. Because of the way a background state is defined, the resonant energy and the widths associated with it do not have an immediate physical meaning.
Background states can also be used to model non-resonant processes. In this case, one assumes that the non-resonant contribution is constant with energy in the energy range of interest. It is worth noting explicitly that this means the R-matrix theory is unable to discriminate between the contribution of unseen, high-energy resonances and a non-resonant process.

2.5 The electron screening effect

The energies E of interest for astrophysical scenarios are often significantly lower than the Coulomb barrier between the interacting nuclei, i.e. $E \ll V_C$. From a quantum mechanical point of view this situation requires the projectile to tunnel through a Coulomb potential barrier, a process which is strongly dependent on energy. Therefore, the cross-section of nuclear reactions between charged particles drops exponentially at low energies. To avoid dealing with a strongly-varying cross-section it is often useful to introduce the astrophysical S-factor $S(E)$, which is defined implicitly as

$$\sigma(E) = \frac{1}{E} S(E) \exp(-2\pi\eta) \tag{2.31}$$

where the energies are in the CM frame and $2\pi\eta = 2\pi Z_1 Z_2 e^2/\hbar v$ is the Sommerfeld parameter[2]. $Z_{1,2}$ are the charges of the interacting nuclei, μ is their reduced mass, and v is the velocity in the CM frame. Most of the energy dependence of the cross-section is absorbed in the $\frac{1}{E}\exp(-2\pi\eta)$ term, while $S(E)$ gives the nuclear contribution.

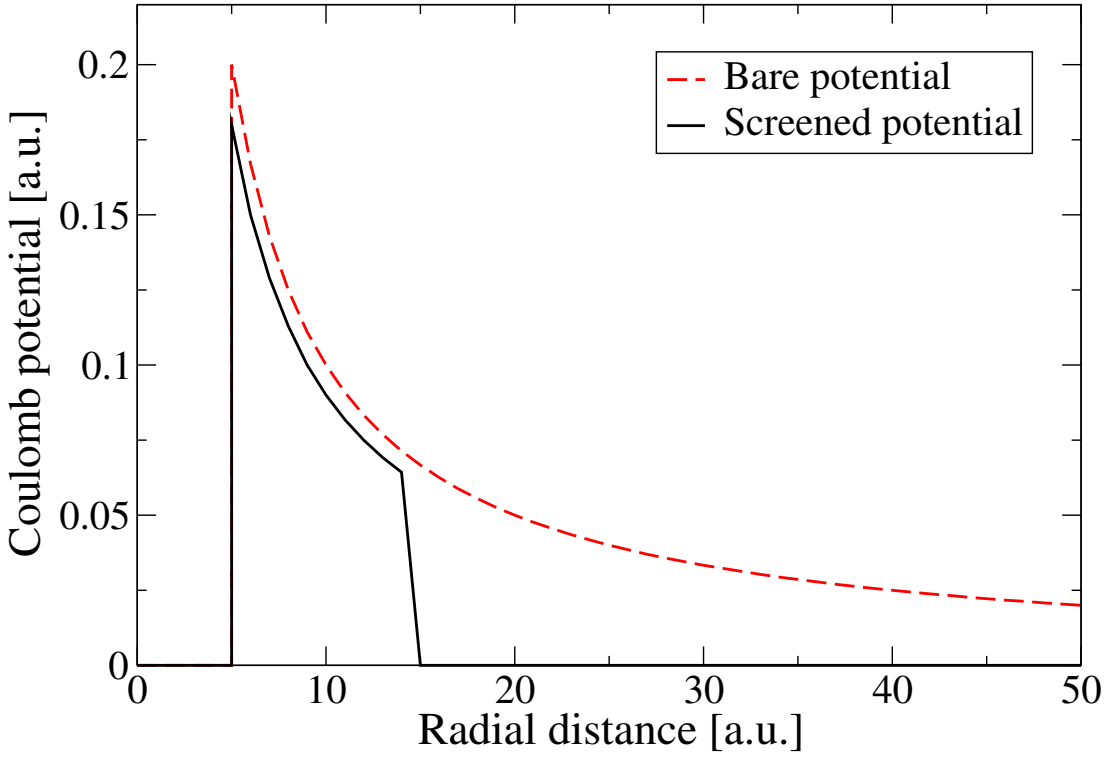

Figure 2.5 *An idealised and simplified sketch of the Coulomb potential seen by a charged particle interacting with an atom (black line) vs. the Coulomb potential for a bare nucleus (dashed red line). Adapted from ref. [3].*

Until now we have implicitly assumed the nuclei to be *bare*, that is to say without a surrounding electron cloud. However, this is not true. The presence of an electron cloud changes the behaviour of the Coulomb potential, as sketched in Fig. 2.5. The reduction of the Coulomb barrier increases the likelihood of tunnelling and therefore the probability of a reaction to occur. This effect is known as electron screening and it is especially significant at low interaction energies ($E \ll V_C$). In an Earth-based laboratory, targets (and sometimes projectiles) are not bare. In the stellar plasma nuclei are bare but surrounded by a sea of electrons which may screen the nuclear Coulomb potential at high stellar densities [3]. Our objective is to extract a stellar reaction rate from nuclear physics measurements on Earth and electron screening must be accounted for. A theoretical framework to accurately

[2]The quantity η is also known as the Gamow parameter.

model electron screening is still outside of our grasp, see e.g. the recent ref. [15]. The models that are usually employed to account for this effect do not always agree with experimental observations. A full discussion of the history of the electron screening problem is beyond the scope of this work. A classic introduction to electron screening and the adiabatic model can be found in refs. [3, 16], while ref. [17] has a more in-depth theoretical discussion of the issue. In this section, I will present the adiabatic model that is described in these three references, and generally used in low-energy nuclear astrophysics experiments [18].

The penetration through a screened Coulomb barrier at a given energy E is equivalent to that through a non-screened Coulomb barrier at energy $E_{\text{eff}} = E+U_e$ where U_e is the screening potential. To find U_e one employs the adiabatic approximation. In an atom, the electrons and the nucleus have characteristic velocities, v_e and v_n respectively. If $v_e \gg v_n$ then the electrons can be assumed to react instantly to the motion of the nucleus and one can decouple the motion of the nucleus from that of the electronic cloud. This is known as the adiabatic approximation or the Born-Oppenheimer approximation. Under this approximation, when two non-bare nuclei fuse, the electrons instantly occupy the atomic orbitals of the compound nucleus. If this is the case, the screening potential U_e can be calculated [18] as the difference between the atomic binding energy of the compound atom and the atomic binding energies of the target and projectile atoms in the entrance channel. We can define a screening correction factor f_e

$$f_e = \frac{\sigma(E_{\text{eff}})}{\sigma(E)} = \frac{E}{E_{\text{eff}}} \frac{\exp\{-2\pi\eta(E_{\text{eff}})\}}{\exp\{-2\pi\eta(E)\}} \tag{2.32}$$

with the assumption $S(E) \simeq S(E_{\text{eff}})$, which is true if $E \simeq E_{\text{eff}}$. Note that the screening potential U_e is usually of the order of a few hundred eV, and the electron screening correction is significant only at low energies ($E_{\text{CM}} \lesssim$ 100 keV).

2.6 Thermonuclear reactions in stars

This section deals with the calculation of the reaction rate, a quantity which expresses the likelihood of a reaction taking place in a star. Reaction rates can be used in astrophysical models of stars, to predict stellar observables. The

calculation of a reaction rate is the last step in deducing the properties of a nuclear reaction in stars from experimental measurements on Earth.

2.6.1 Reaction rate

The cross-section of a nuclear reaction depends on the number of reagents available as well as their interaction energy. While cross-sections are useful to express the probability of interaction in an Earth-based laboratory, in a star the reaction rate r_{01} is used instead [1, 2]:

$$r_{01} = N_0 N_1 v\sigma(v) \tag{2.33}$$

where 0 and 1 are two nuclear species, $N_0 = N_T/V$, $N_1 = N_B/V$ (see Eq. 2.1), and V is the unit volume. In a laboratory the energy of the interaction is fixed between E_b and $E_b - \Delta E$. In a star, the energy available to the reactions is the *thermal* energy of the nuclei. These *thermonuclear* reactions occur in a wide range of energies or equivalently velocities. In most situations, the velocity probability distribution $P(v)$ can be described by a Maxwell-Boltzmann distribution, and one can rewrite the reaction rate as [2]

$$r_{01} = N_0 N_1 \int_0^\infty vP(v)\sigma(v)dv = N_0 N_1 \int_0^\infty v(E)P(E)\sigma(E)dE = \\ N_0 N_1 \langle\sigma v\rangle_{01} = N_0 N_1 \sqrt{\frac{8}{\pi m_{01}}} \frac{1}{(k_B T)^{3/2}} \int_0^\infty E\sigma(E) e^{-E/k_B T} dE \tag{2.34}$$

where $\langle\sigma v\rangle_{01}$ is the reaction rate per particle pair, m_{01} is the reduced mass, k_B is Boltzmann's constant, and T is the temperature. Everything is in principle known in Eq. 2.34 except the cross-section $\sigma(E)$, which is obtained as described in the previous sections, and the temperature T, which depends on the astrophysical scenario of interest. Knowing $\sigma(E)$ one can calculate numerically the integral in Eq. 2.34 as a function of T. The details of this calculation and most of all the treatment of uncertainties are not entirely straightforward. In this work, the reaction rate calculation was carried out using a standard tool called RatesMC, which is briefly described in section 2.6.3.

2.6.2 The Gamow peak

When planning a nuclear physics measurement to investigate a stellar scenario where thermonuclear reactions occur at a typical temperature T, it is necessary to determine at which energies the cross-section should be measured. A straightforward way of doing so is by calculating the position and width of the Gamow peak. In Eq. 2.34, the integral depends on the product of two terms, the cross-section $\sigma(E)$ and the Maxwell-Boltzmann factor Ee^{-E/k_BT}. Employing Eq. 2.31, one can write

$$\langle \sigma v \rangle_{01} \sim \int_0^\infty S(E) e^{-2\pi\eta} e^{-E/k_BT} dE \tag{2.35}$$

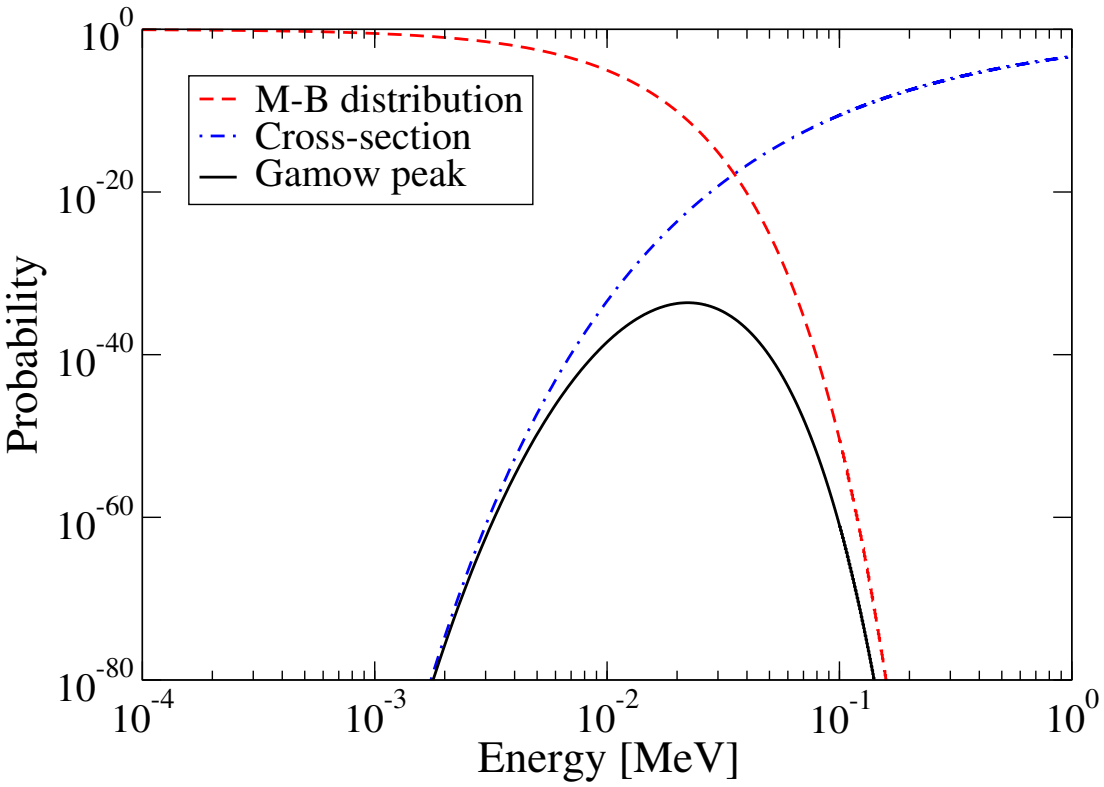

Figure 2.6 *The Gamow peak for the $^{17}O(p,\alpha)^{14}N$ reaction at T=0.01 GK, assuming S(E)=1. The probability of interaction has a maximum around $E \simeq 30$ keV.*

If the S-factor is approximately constant (i.e. there are no strong resonances), for a given temperature T one can calculate the product of the two exponentials in Eq. 2.35 as a function of the energy. As shown in Fig. 2.6, a peak appears in a relatively narrow energy range. This is the Gamow peak, which is located at the energies that give the largest contribution to the reaction rate for a given

temperature T and a given pair of nuclei. While the Gamow peak is a very useful approximation, it does break down in case of very strong resonances.

2.6.3 RatesMC

RatesMC is a standard program used to calculate reactions rates from nuclear physics inputs. It is described in ref. [19], and available online on the website of the STARLIB compilation [20, 21]. RatesMC is a Monte Carlo program that takes as the input the R-matrix parameters and their uncertainties for a given reaction, and provides as the output the reaction rate and its uncertainty. For every iteration, each input parameter is randomly assigned a value with a probability density function defined by the parameter's central value and uncertainty. A reaction rate is then calculated numerically at temperature values of interest based on the random values generated and a new iteration begins. At the end of the Monte Carlo calculation, the average, the median and other estimators of the reaction rate are calculated temperature by temperature, based on the reaction rates obtained while iterating. In this work, the median reaction rate and the suggested upper and lower rates will be quoted. The upper (lower) rate is calculated as the the 0.84 (0.16) quantile of the cumulative distribution function. If the distribution of the reaction rates is Gaussian, these quantiles correspond to the values at $\pm 1\sigma$ from the median. For further details on RatesMC see ref. [19].

Chapter 3

Current status of the ^{17,18}O(p,α)^{14,15}N reactions

3.1 The ^{17}O(p,α)^{14}N reaction

3.1.1 Previous measurements

The first direct measurements of the ^{17}O(p,α)^{14}N reaction (Q-value = 1.192 MeV) were performed by Ahnlund in 1957 [22] and Brown in 1962 [23], spanning a combined energy range $E_{\rm p} = 490 - 3000$ keV in the laboratory. They observed several resonances corresponding to states in the compound nucleus ^{18}F, which at the time was not well-known. Later, Kieser and collaborators [24] managed to reach proton energies as low as $E_{\rm p} = 400$ keV in the laboratory frame. No systematic scan of the excitation function has ever been performed below $E_{\rm p} = 400$ because of the dramatic drop in the cross-section at low energies (see Fig. 2.1). However, the Gamow peak for ^{17}O(p,α)^{14}N is expected to be at an energy of just $E_{\rm p} \simeq 30$ keV (see Fig. 2.6) for a typical temperature of T=0.01 GK of interest in scenarios such as AGB stars. At these energies, two states discovered in 1961 by Silverstein *et al.* [25] dominate the reaction rate. Because of their importance, the two resonances corresponding to these two states have been the focus of several investigations. The resonant energies of these two states were measured by, among others, Silverstein *et al.* [25], Bogaert *et al.* [26] and more recently Chafa *el al.* [27]. This latter, the most precise measurement, reported

observing the two states at $E_x = 5671.6 \pm 0.2$ keV and $E_x = 5789.8 \pm 0.3$ keV, corresponding to E_p= 70 and 193 keV respectively.

The resonance with the higher energy, corresponding to $E_p = 193$ keV, was first observed by Fox *et al.* [28], and then measured independently by Chafa *et al.* [29], Moazen *et al.* [30], and Newton *et al.* [31]. These three measurements [29, 30, 31] are in excellent agreement and this resonance can be considered quite well-known. Its resonance strength is $\omega\gamma = 1.67 \pm 0.17$ meV [31].

The situation is significantly more complicated for the lower energy resonance, at $E_p = 70$ keV, as summarised in Table 3.1. A first direct measurement of the strength of this resonance was attempted by Berheide *et al.* [32], and resulted in an upper limit $\omega\gamma \leq 0.8$ neV. Later, Blackmon *et al.* [33, 34] perfomed a second direct measurement of this resonance and found a significantly higher strength value, in disagreement with the previous upper limit. Following this work, the data acquired by Berheide *et al.* were re-analysed by Niemeyer [35] who found a much higher upper limit value, in agreement with Blackmon's measurement. Later, however, issues were found in the statistical treatment in Blackmon's work and a simple independent re-analysis was performed by Hannam and Thompson [36]. Following their work, Blackmon performed a second, unpublished re-analysis of the data [37] which was used to calculate the reaction rate in the widely used STARLIB [21] compilation. Recently, two indirect measurements of the E_p=70 keV resonance were performed using an indirect method (Trojan Horse) by Sergi *et al.* [38, 39]. Note that this indirect technique, unlike the direct measurements, is not affected by electron screening.

Table 3.1 *A review of the most recent determinations of the strength of the $E_p = 70$ keV resonance in $^{17}O(p,\alpha)^{14}N$. See text for details.*

Reference	$\omega\gamma$ [neV]	Method
Berheide *et al.* [32]	≤ 0.8	Direct
Blackmon *et al.* [33, 34]	$5.5^{+1.0}_{-0.9}$	Direct
Niemeyer *et al.* [35]	≤ 22.0	Reanalysis of [32]
Hannam and Thompson [36]	$5.3^{+0.9}_{-0.8}$	Reanalysis of [33]
Blackmon [37]	$4.8^{+0.5}_{-0.5}$	Reanalysis of [36]
Sergi *et al.* (2010) [38]	$3.66^{+0.76}_{-0.64}$	Indirect
Sergi *et al.* (2015) [39]	3.42 ± 0.60	Indirect

3.1.2 Aims of the present study

The aim of the present study was a precise, direct measurement of the E_p = 70 keV resonance in $^{17}O(p,\alpha)^{14}N$. Because of the weakness ($\omega\gamma \sim$ neV) of this

resonance, a very low counting rate was expected (few counts/h, see section 5.2). A reliable method of precisely identifying a region of interest (ROI) for the signal in the energy spectrum was mandatory. To obtain this ROI, it was decided to measure the $E_p = 193$ keV resonance in the same set-up employed for the $E_p = 70$ keV resonance. The $E_p = 193$ keV resonance is six to seven orders of magnitude stronger than the $E_p = 70$ keV and a clear signal was expected. Since the reaction's Q-value (1.192 MeV) is significantly higher than the beam energy, the energy of the α particles detected in this experiment is almost independent of the beam energy. Therefore, the ROIs for the two resonances were expected to be very close in energy. Note this type of combined measurement has never been attempted in the past for this reaction.
Our aims were thus:

- to measure the strength of the $E_p = 193$ keV resonance in $^{17}O(p,\alpha)^{14}N$
- to infer a ROI for the $E_p = 70$ keV resonance in $^{17}O(p,\alpha)^{14}N$
- to measure the strength of the $E_p = 70$ keV resonance in $^{17}O(p,\alpha)^{14}N$

3.2 The $^{18}O(p,\alpha)^{15}N$ reaction

3.2.1 Previous measurements

There exist several measurements of the $^{18}O(p,\alpha)^{15}N$ reaction (Q-value=3.979 MeV) over a wide energy range, most of which are today obsolete. For a full history of this reaction see the compilations in refs. [40, 41, 42] and the more recent ref. [43] and references therein. A selection of the most recent measurements is summarised in Table 3.2, toghether with other measurements investigating the same compound nucleus, ^{19}F. The measurements are in relatively good agreement at energies above $E_p = 160$ keV, though tensions between different datasets have been reported [43]. At lower energies, closer to those of astrophysical interest in AGB stars, the only direct data available are those from ref. [44]. In addition to the direct data in Table 3.2, the THM was employed to study a few resonances below $E_p = 1$ MeV, and in particular the low energy $E_p = 20$ keV resonance.

From an astrophysical point of view, the reaction rate is dominated by two broad resonances at energies ranging from $E_p \simeq 600$ to 850 keV depending on

Table 3.2 *A selection of the most recent measurements involving the ^{19}F compound nucleus. The energies are reported in the CM frame for $^{18}O(p,\alpha)^{15}N$. The angles are in the laboratory frame.*

Reaction	Energy range [keV]	Angle [deg]	**Reference**
^{18}O(p,α)^{15}N	70 – 886	90, 135	[44]
^{18}O(p,α)^{15}N	220 – 660	Integrated	[45]
^{18}O(p,α)^{15}N	590 – 1670	Several	[46]
^{18}O(p,α)^{15}N	330 – 940	165	[47]
^{18}O(p,p)^{18}O	570–1340	90,140	[48]
^{15}N(α,α)^{15}N	< 340	Several	[49]

the reference (see ref. [43]) as well as a narrow and very intense resonance at $E_p = 151$ keV. These three resonances all have the same $J^\pi = 1/2^+$ and give rise to a complex interference pattern. In addition to these three resonances an extremely weak ($\omega\gamma \simeq 10^{-19}$ eV) $E_p = 20$ keV state could play a key role in the determination of the reaction rate at astrophysical temperature. Other resonances are generally narrow and less relevant from an astrophysical point of view. Table 3.3 shows the current situation below $E_p = 1$ MeV.

Table 3.3 *A selection of the $\omega\gamma$ values of the resonances in $^{18}O(p,\alpha)^{15}N$ at energies below $E_p = 400$ keV. a) Distorted Wave Born Approximation. b) Trojan Horse Method*

E_p [keV]	$\omega\gamma$ [eV]	Uncertainty	Reference	Method
20	$6^{+17}_{-5} \times 10^{-19}$	-	[42]	DWBA[a)]
	$8.3^{+3.8}_{-2.6} \times 10^{-19}$	$\sim$40%	[50]	THM[b)]
95	$(1.6 \pm 0.5) \times 10^{-7}$	31%	[44]	Direct
	$(1.76 \pm 0.33 \times 10^{-7}$	19%	[50]	THM[b)]
151	0.17 ± 0.02	12%	[44]	Direct
	0.167 ± 0.012	7%	[51]	^{1}H(^{18}O,α)^{15}N
216	$(2.3 \pm 0.6) \times 10^{-3}$	26%	[44]	Direct
334	0.057 ± 0.010	18%	[44]	Direct

3.2.2 Aims of the present study

The aim of this study was to carry out a direct investigation of the cross-section of the ^{18}O(p,α)^{15}N reaction at energies accessible by the LUNA-400 accelerator (see section 4.1), that is to say below $E_p = 400$ keV. We planned to extend the direct measurements to energies lower than those reported in ref. [44] and to reduce the uncertainty in the low-energy cross-section. Furthermore, we intended to study all the accessible resonances and the $E_p = 151$ keV resonance in particular. Finally,

the resonance at $E_{\mathrm{p}} = 95$ keV has recently been the subject of some debate, and the recent ref. [52] claimed theoretical issues arise from the comparison of the α– and the γ–width of this state. We planned to pay particular care in the measurement of this last resonance. Because of the numerous datasets available, including some on reactions involving the same compound nucleus ^{19}F, the final analysis was planned to be carried out exploiting the R-matrix technique described in the previous chapter. Previous R-matrix fits involving the ^{19}F nucleus were performed in refs. [43, 48, 45] among others, but these fits generally consider a very limited number of datasets (often just one) and do not take full advantage of the predictive power of the R-matrix technique. In summary, our aims were:

- to scan the excitation function of the ^{18}O(p,α)^{15}N resonance from $E_{\mathrm{p}} =$ 400 keV to the lowest accessible energies
- to re-measure the strength of the $E_{\mathrm{p}} = 151$ keV resonance in ^{18}O(p,α)^{15}N
- to re-measure the other energetically accessible resonances in ^{18}O(p,α)^{15}N and in particular that at $E_{\mathrm{p}} = 95$ keV
- to analyse and reduce the data employing the R-matrix technique

Chapter 4

Experimental Investigation

This chapter describes the setup that was designed and purpose-built by the workshop of the University of Edinburgh, School of Physics and Astronomy in order to measure both the ^{17,18}O(p,α)^{14,15}N nuclear reactions. Because of the very low counting rates expected, the main requirement for this experiment was to maximise the detection efficiency. In order to reduce the natural background from cosmic rays, the experiment was carried out at the underground LUNA-400kV accelerator located at the Laboratori Nazionali del Gran Sasso, Italy. Section 4.1 and section 4.2 describe the experimental apparatus, including the detectors, and the electronic chain used. The calibration of the detector and the measurements of the thin foils used to protect silicon detectors from elastically scattered beam particles are detailed in section 4.3. Section 4.4 describes the simulations and measurements performed to obtain the efficiency of the setup. Section 4.5 contains all details on the targets, including target preparation, thickness measurement and target degradation measurement. The final commissioning tests are described in section 4.6 and the quantitative advantage of moving underground to perform charged-particle spectroscopy is described in section 4.7. For the technical details of how data were extracted from experimental spectra, see apprendix A. Commissioning results have been published in ref. [53].

4.1 Experimental setup

The experimental campaign was carried out in direct kinematics, detecting the alpha particles produced by the ^{17,18}O(p,α)^{14,15}N nuclear reactions. A proton beam was accelerated by the underground LUNA-400kV accelerator [54, 55] at typical beam intensities $I = 100 - 200$ μA. The beam was steered through two slits and a quadrupole (Fig. 4.1) before arriving on a solid Ta_2O_5 target. Targets were enriched in either ^{17}O or ^{18}O and supported by a water-cooled Ta backing which stopped the beam and acted as a Faraday cup (see later). See section 4.5 and ref. [56] for more details on the targets.

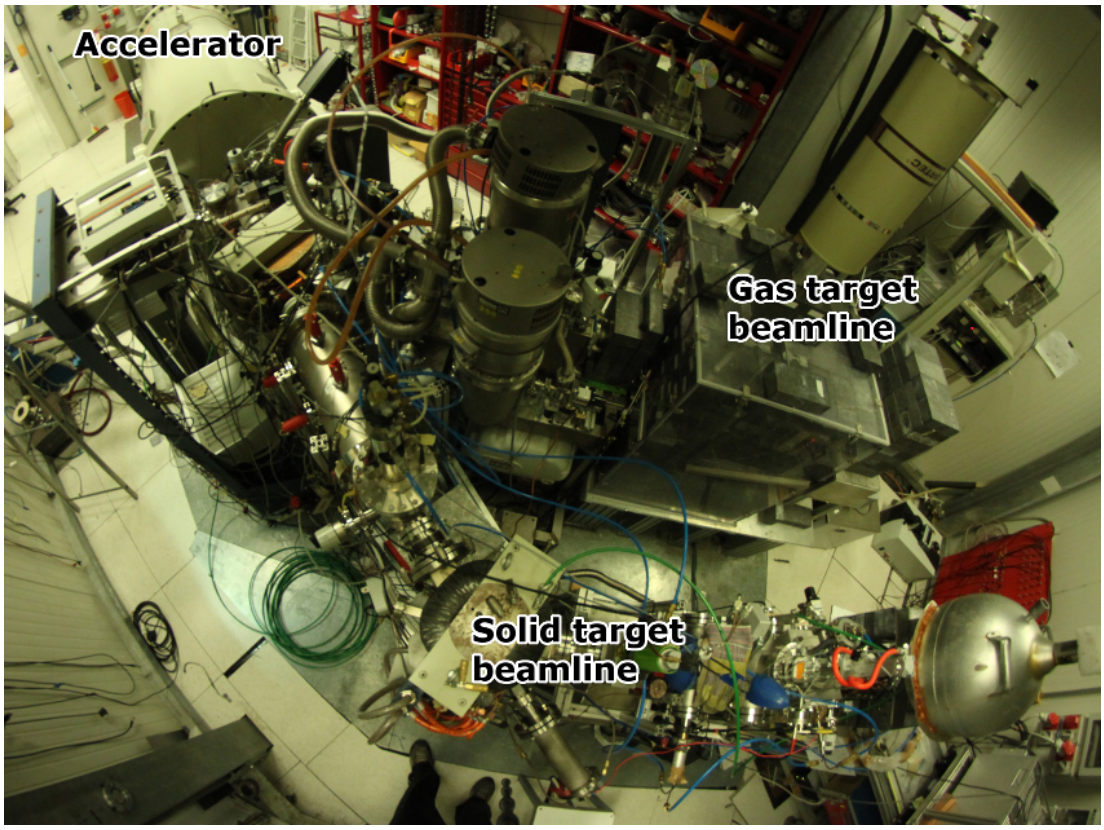

Figure 4.1 *A picture of the accelerator room, showing the accelerator (top left), the gas target beamline (top), and the solid target beamline used in this experiment (bottom). The scattering chamber (not visible) is mounted at the end of the solid target beamline, in the bottom-right of the picture.*

Targets were mounted in the centre of a reaction chamber consisting of two concentric domes, an outer one in aluminium and an inner one in copper. Alpha particles produced by the reaction were detected at backward angles with respect

Table 4.1 *The detectors used during the two experimental campaigns. $^{17}O(p,\alpha)^{14}N$ and $^{18}O(p,\alpha)^{15}N$ refer to the status of the detectors during the experimental campaigns aimed at measuring either reaction. See text for details.*

Detector	Thickness	Angle	^{17}O(p,α)^{14}N	^{18}O(p,α)^{15}N
#1	700 μm	135°	OK	OK
#2	300 μm	135°	OK	OK
#3	300 μm	135°	OK	OK
#4	300 μm	102.5°	Noisy towards the end	OK
#5	300 μm	102.5°	OK	OK
#6	700 μm	102.5°	Stopped working	Not working
old #7	700 μm	135°	Noisy towards the end	Replaced detector #8
new #7	700 μm	135°	Not present	Broke towards the end
#8	150 μm	102.5°	Data discarded	Removed

to the beam direction by an array of eight Canberra PIPS silicon detectors housed in the outer aluminium dome (Fig. 4.2). All detectors had an area of 900 mm^2, an ultra-thin dead layer (<50 nm) and a typical resolution of 40 keV FWHM at the 5.486 MeV ^{241}Am peak. Detectors were arranged in two rows: four detectors were placed[1] at 135° ("upper row"), and four at 102.5° ("lower row"). Detectors #1,2,3 and #5 were used for both experimental campaigns. Detector #4 started suffering from strong electronic noise towards the end of the ^{17}O(p,α)^{14}N experimental campaign, but was usable throughout the ^{18}O(p,α)^{15}N experimental campaign. Detectors #6 and #7 stopped working towards the end of the ^{17}O(p,α)^{14}N experimental campaign. Detector #8, the thinnest one, always suffered from electronic noise. Data from this detector were discarded. At the start of the ^{18}O(p,α)^{15}N experimental campaign, detector #7 was replaced with a new, working detector while detector #8 was replaced with the former #7. The new detector #7 was damaged by the beam toward the end of the ^{18}O(p,α)^{15}N experimental campaign and stopped working. See Table 4.1 for a summary.

The inner copper dome shown in Fig. 4.3 was mounted concentric to the aluminium dome. It had three purposes: to prevent carbon deposition on the target, to suppress the secondary electrons and to support the foil protecting the detectors. Carbon deposition on the target can occur when carbon impurities in the vacuum introduced by the oils of the vacuum pumps are captured by the beam and transported downstream. To prevent this phenomenon, the copper

[1] Angles are given in the laboratory frame, but are not significantly different in the CM frame for either reaction.

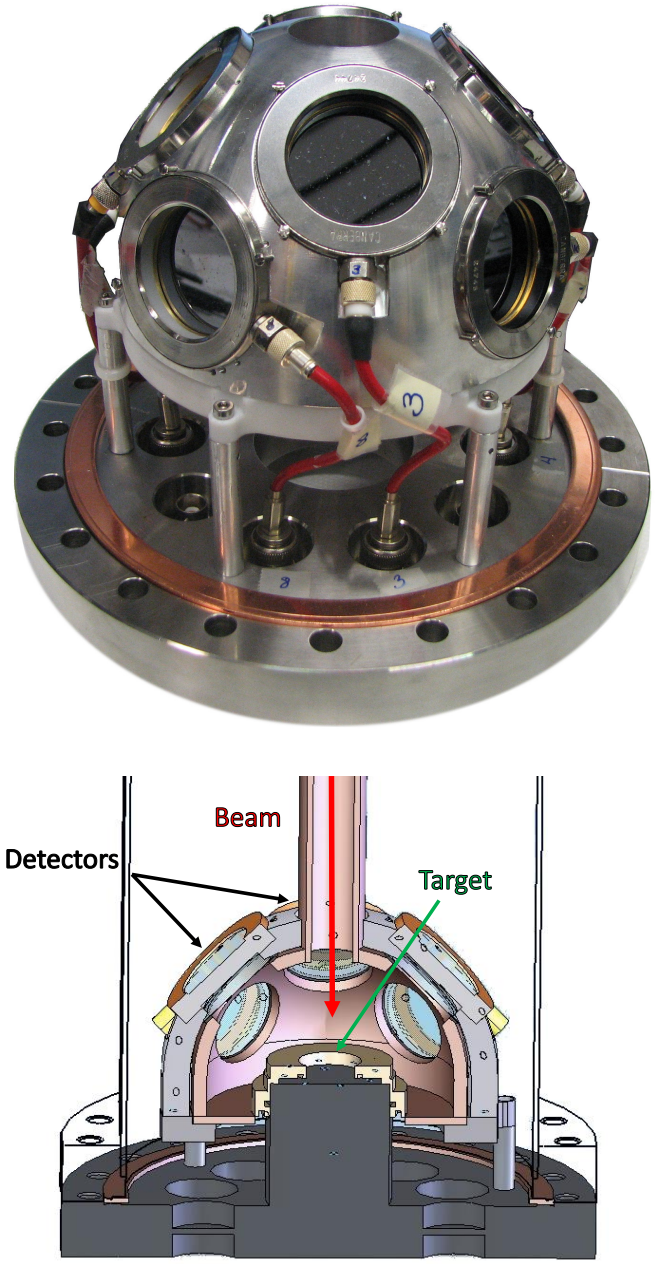

Figure 4.2 *(top) A picture of the reaction chamber with the eight silicon detectors mounted on the outer aluminium dome. The beam enters from the hole in the top. (bottom) A cut-away CAD render of the reaction chamber, showing the inside.*

dome was placed in thermal contact with the cold finger of the beamline. The cold finger is a copper pipe kept at liquid nitrogen temperatures ($\sim$ 80° K). Carbon impurities carried by the beam were frozen and captured by the cold finger or the copper dome, and no carbon deposition was observed on the targets during the measurement.

To suppress secondary electrons, the copper dome was biased at -200 V. The current reading for the experiment was performed using the Ta_2O_5 target as a Faraday cup and integrating the current read. This current is a flow of electrons that travels from the ground to the target to balance the charge deposited by the beam of protons (H^+). For each proton that hits the target, one electron flows inside. In addition to this electron current, however, secondary electrons may be produced by the protons in the target. If one of these secondary electrons escapes from the target, a new electron has to flow inside the target to balance the charge, leading to a double-counting of some protons. Biasing the copper dome with a negative potential produces an electric field that repels escaping electrons back onto the target, avoiding misreading of the beam current.
Finally, the third purpose of the copper dome was to house the foils used to stop the flux of protons elastically (back-)scattered off the solid target and onto the detectors. Because of the high beam intensities ($\sim 100\mu$A) these scattered protons could have increased the dead time, polluted the energy spectra and eventually damaged the fragile silicon detectors. More information about these foils is given in section 4.3.
During data taking the setup was kept under high vacuum (10^{-7} mbar) by a turbomolecular pump backed by a root pump. Whenever the targets degraded and had to be replaced (see section 4.5), the vacuum was broken and the chamber was flushed with N_2 gas to avoid water vapour condensation on the cold copper dome. After replacing the target, the pumps were restarted.

4.2 Electronic chain

The signals generated in the eight detectors were analysed though a standard electronic chain, sketched in Fig. 4.4. Each detector was connected to a pre-amplifier (Cooknell EC572) with 10 mV/MeV gain setting with 50 Ω load. A BNC PB-4 pulser was connected to the TEST input of the pre-amplifier to monitor gain stability and dead time. After the pre-amplifier the signal was split in two. The first half was processed through an amplifier (EG&G Ortec 855 Dual Spectroscopy Amplifier) with 1.5 μs shaping time and 40 dB (= 100×) gain. The overall gain was therefore roughly 100 × 10 mV/MeV = 1 V/MeV. The shaped signal was sent to an Analogue to Digital Converter module (Silena 9418/6V ADC). The ADC had a sharp threshold at 48 channels, corresponding to roughly 65 keV, depending on the detector.

Figure 4.3 *A picture of the copper dome, with the aluminized Mylar foils mounted. The beam enters through the hole in the top, while the target is inserted from the bottom.*

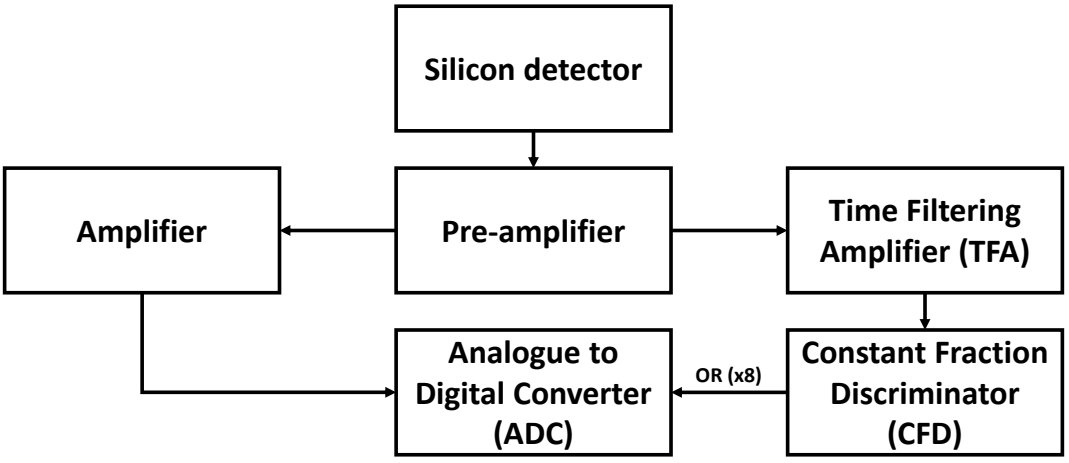

Figure 4.4 *A simplified sketch of the electronic chain employed in the investigation.*

The other half of the signal was sent through a Time Filter Amplifier (EG&G Ortec 863 Quad TFA) with 500 ns integration and differentiation times. The outputs of the eight TFAs were sent to an eight-channel Constant Fraction Discriminator (EG&G/ESN CF8000 Octal CFD) which performed a logic OR on the eight signals and sent a trigger to open the gate of the ADC. Thresholds

values of the CFD and were usually between 50 and 100 mV ($\simeq$ keV) depending on detector.

In addition to the Silena ADC, the Data Acquisition System (DAQ) consisted of a CAEN V560N scaler and a Motorola MVME 2434 PowerPC CPU. The scaler acquired the number of triggers sent by each detector, the number of total and accepted triggers, the real run time with a 1 ms precision, and the charge as supplied by the current integrator of the beamline. The charge recorded had a nominal random uncertainty[2] of $\pm 3\%$ and a nominal systematic uncertainty of $\pm 2\%$.

The Motorola CPU, which performed the data acquisition, was connected via an ethernet cable to a Sun Solaris workstation running the MIDAS interface package [57]. Data was acquired in list-mode: whenever a trigger was sent, the value of all scalers and all ADC channels with valid data were written to disk. This allowed me to analyse how quantities of interest (e.g. event rate in a given detector) varied over the course of an experimental run. One quantity of particular interest is the multiplicity of an event, i.e. the number of detectors with a signal over the energy threshold of the ADC. For instance, a pulser event should have a multiplicity of eight if eight detectors are connected. The expected counting rates were low ($\ll$ 1 kHz per detector) and only one alpha particle is emitted per reaction. Unless otherwise specified, events with multiplicity equal to the number of detectors were always discarded. These events included pulser counts as well as occasional bursts of electronic noise affecting the whole setup. I developed a simple Monte Carlo simulation in order to quantify the probability of the occurrence of a high-multiplicity signal event, and I found that the probability was vanishingly small ($\ll 0.1\%$) for realistic rates. Therefore no correction to the data was required for a high-multiplicity cut. High-multiplicity here means multiplicity equal to the number of working detectors, which did change over the course of the campaigns (Table 4.1).

Data were acquired in parallel and the dead time was common for all eight detectors. The rates varied during the campaign from a few signals per minute at low energies up to a hundred Hz at resonant energies. Dead time was not a major source of uncertainty, and was treated according to the model in ref. [58]

$$\frac{\text{live time}}{\text{dead time}} = 1 - n\tau \tag{4.1}$$

[2]This random uncertainty will always be added in quadrature to the Poisson uncertainty in the number of counts in this work.

where n is the trigger rate sent to the ADC (trigger per second) and τ is the characteristic event processing time of the setup used. I estimated $\tau = 37$ μs from a combination of ADC conversion time, polling and gate width (2 μs). The model in Eq. 4.1 works under the condition $n \ll 1/\tau \simeq 30$ kHz, which was always true for both experimental campaigns. Assigning an uncertainty to the dead time is not straightforward. Assuming the model holds, the uncertainty depends on τ. However, even assigning a very conservative uncertainty of $\pm$ 10 μs to τ, the final impact on live time ratios for rates lower than 1 kHz is smaller than 1% and negligible compared to other sources of uncertainty. All data presented in this work were corrected for dead time using the model in Eq. 4.1 and the uncertainty on the dead time was neglected. The model in Eq. 4.1 was tested during the commissioning (section 4.6) by comparing the measured strength of the E_{p}=151 keV resonance in ^{18}O(p,α)^{15}N for different estimated dead time values, up to 20%. The measured strength was in agreement with the reported value in ref. [51] at all dead times values. Therefore, the model in Eq. 4.1 can be considered reliable.

4.3 The protective foils

Thin foils were mounted in front of each detector in order to stop the intense flux of beam protons elastically scattered off the target [59]. Foils had to be sufficiently thick to stop the protons, yet thin enough to allow the alpha particles (produced by the reaction) to reach the detectors with detectable energies. Since both reactions studied had positive Q-values, the energy of the alpha particles at production was always higher than the energy of the beam protons. However, the energy loss of charged particles in matter is proportional to Z^2_{particle} [58], which means it is four times higher for alpha particles than it is for protons of the same energy. Simulations employing TRIM [11] were carried out in order to optimise the foil thickness and material.

For the ^{18}O(p,α)^{15}N campaign, because of its high Q-value (3.979 MeV), finding a suitable thickness and material was relatively straightforward. Commercially available (Goodfellow [60]) aluminised Mylar foils, nominally 5.4$\pm$0.5 μm thick, were chosen. According to TRIM simulations, less than 1 in 10^6 simulated protons at E_{p}=360 keV (the highest energy used in the experiment) would pass through the foils. Alpha particles from the ^{18}O(p,α)^{15}N reaction should instead be detected, after the foils, at approximately 2 MeV. To perform an

independent measurement of the thickness of the foils, small (2×2 cm^2) samples from these foils were measured in a dedicated set-up. A single silicon detector was placed under vacuum (10^{-6} mbar) in front of a triple-peak alpha source. Data were acquired with and without a foil sample in between the detector and the radioactive source, and the energy shift observed in the three peaks was used to calculate the thickness of the foil sample. This thickness was found to be 5.0μm on average, in agreement within the manufacturer's nominal 10% tolerance. The alpha peak from the ^{18}O(p,α)^{15}N reaction, expected at 2.2 MeV, was in any case always visible above the background, and precisely defining a ROI *a priori* was not required.

The situation was significantly more complex for the ^{17}O(p,α)^{14}N reaction, for which the Q-value is 1.192 MeV only. At backward angles, alpha particles are emitted with energies as little as $E_\alpha \simeq 1$ MeV. One of the main objectives of the ^{17}O(p,α)^{14}N experimental campaign (chapter 5) was the measurement of the E_p=70 keV and the E_p=193 keV in the same experimental conditions. Therefore the foils used had to be thick enough to stop protons up to E_p=193 keV resonance while still letting the alpha particles through with detectable energies[3]. According to TRIM simulations, aluminised Mylar foils around 2.4 μm thick would have been suitable for the study of this reaction. Less than 1 in 10^6 simulated protons would survive through the foils and the alpha particles produced by the $E_\mathrm{p} = 70$ keV ($E_\mathrm{p} = 193$ keV) resonance would be detected, after the foils, with an energy around E_α=200 keV (E_α=250 keV).

Mylar foils, nominally 2.0 μ thick, were bought from DuPont [61] and a nominally 0.4 μm aluminium layer was deposited on top by Lebow Company [62]. Samples of the foils were measured using the same procedure described previously, and the *average* thickness found agreed with the nominal one. The inhomogeneity of the small foil samples measured was estimated at a conservative $\pm$0.1 μm. The uncertainty due to the foil inhomogeneity roughly translates to a $\pm$40 keV uncertainty in the detected energy of the alpha particles for the E_p=70 keV resonance, which is not negligible. Since aluminised Mylar foils are extremely fragile they can only be used once, and therefore they cannot be reliably measured before or after mounting them in the chamber.

In order to estimate the expected energy for the alpha particles generated by the E_p=70 keV resonance, the E_p=193 keV resonance in ^{17}O(p,α)^{14}N was measured. In spite of the TRIM simulations predicting that no protons would leak through

[3]Changing the foils in between the two measurements would have introduced systematic uncertainties in the determination of the ROI.

the foils, the counting rate in the spectra of the detectors was very significant up to 250–300 keV detected energy, masking the alpha peak from the E_{p}=193 keV, expected at $E_{\alpha} \simeq 250$ keV. The origin of this beam-induced background was never completely obvious, and the phenomenon was most likely due to a combination of effects:

1. Inhomogeneity of foils. If any part of the foil is significantly thinner than the average value, even in a small region, low-energy protons could leak through this thinner region and hit the detector. Note that realistically we can only measure the average thickness of the foils mounted.

2. Proton pile-up. If many protons are able to pass through the foils with low energies, even too low to be detected, they might pile-up in the gate of the ADC and generate a signal. TRIM simulations indicated than less than one proton in 10^6 should survive, but the model used in TRIM may not be reliable to one part in one million, especially at low energies.

3. Secondary electrons. Even if the protons are completely stopped in the foils, secondary electrons[4] may be produced by the ionisation process as described in section 4.1. These secondary electrons may exit the foils and pile-up as above. The secondary suppression bias applied to the copper dome would accelerate electrons *away* from the dome, which in this case means towards the detectors.

In order to reduce this effect, thin stainless steel collimators were mounted in front of each detector. These collimators, shown in Fig. 4.5 were 0.8 mm thick disks, with a circular 1 cm^2 aperture in the middle and completely stopped incident protons and alpha particles. The geometric efficiency of the detectors was clearly reduced by the collimators, but so was the pile-up probability. The geometric efficiency is linearly proportional to the active area while the pile-up probability has at least a quadratic dependency on the active area, since pile-up requires multiple particles hitting a detector at the same time. We were able to sacrifice approximately 90% of the efficiency of the setup in return for less pile-up, which allowed us to clearly detect the alpha peak from E_{p}=193 keV resonance (see Chapter 5 for details).
The discrepancy between the TRIM simulation and the experimental results just described is evidence that TRIM simulations with an average measured foil

[4]Also known as δ electrons

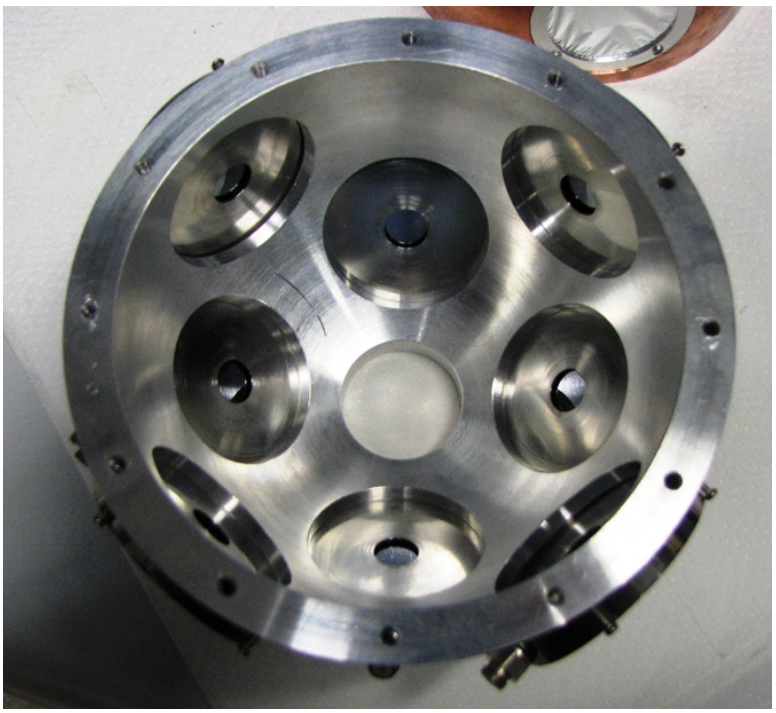

Figure 4.5 *A picture of the aluminium dome seen from the inside with the collimators mounted in front of each detector. The beam enters from the large hole in the middle.*

thickness are unreliable when studying large energy losses of charged particle through passive materials, as reported *e.g.* in ref. [31]. In order to obtain a precise estimate of the thickness of the foils, and in turn a precise estimate of the ROI, an iterative calibration procedure was developed. This procedure employed the alpha peak from the two resonances at E_{p}=193 keV in ^{17}O(p,α)^{14}N ($E_\alpha \sim 250$ keV) and at E_{p}=151 keV in ^{18}O(p,α)^{15}N ($E_\alpha \sim 2.2$ MeV). Using the average foil thickness as a starting value, the procedure consisted in the following steps:

1. For a given foil thickness, calculating the expected energies of the alpha particles after the foils
2. Defining a two-point calibration using one of the two alpha peak energies obtained and the offset from a pulser walkthrough [5]
3. Inferring the energy of the other alpha peak from the calibration

[5] A pulser walkthrough consists in determining the channel corresponding to various pulser amplitudes, and extrapolating the results to find the channel corresponding to pulser amplitude zero to obtain the offset of the calibration. It also verifies the linearity of the electronic chain. A pulser walkthrough is independent of the foil thickness.

4. Comparing the energy obtained in point 3 with that expected from SRIM

5. Repeating steps 1–4 for different foil thickness until the difference in step 4 is minimised

The results from this procedure are shown in Fig. 4.6. In that figure, the procedure above was carried out using the peak of the E_p=151 keV resonance in step 2) and that of the E_p=193 keV resonance in step 3), as well as assuming a thickness of 0.4 μm for the aluminium and optimising the Mylar layer. The Mylar layer was assumed to be facing the beam. No significant differences were found when: a) fixing the Mylar thickness and varying the aluminium's instead; b) simulating the aluminium layer facing the beam; c) exchanging the role of the two alpha peaks (point 3); and d) any combination of the three. Note however that fixing the Mylar layer to 2.0 μm and optimising the aluminium thickness gave a non-physical negative thickness for detector #6, indicating some issues with either the detector or the foil. Detector #6 stopped working shortly after the calibration, and was never used again.

The thickness values obtained with this procedure are the *effective* thickness, in the sense that they reproduce correctly the expected energies for the alpha particles. Whether the "real" thickness of a given foil is that shown in Fig. 4.6 is beyond the scope of this procedure. The dead layer of the silicon detectors can be safely neglected as it is very thin (<50 nm [63]), and it is accounted for within the effective thickness of the foil. The calibration obtained for the detectors, which is tied to the thickness of the foils, should be considered reliable only in the energy range of the alpha particles employed in this procedure, namely 0.1 – 2.2 MeV. After carrying out this procedure, the effective thickness values were employed in a second TRIM simulation to determine the expected ROI of the alpha peak from the E_p=70 keV resonance. Results are shown in Table 4.2. The centroid was taken from the simulation, while the width of the ROI was taken from the alpha peak of the E_p=193 keV resonance. Each detector has a different ROI because the energies, after the foils, are physically different.

4.4 Simulations

Two GEANT4-based [64] simulations (A and B) were performed with the aim of estimating the efficiency of the setup. Details of simulations A and B can

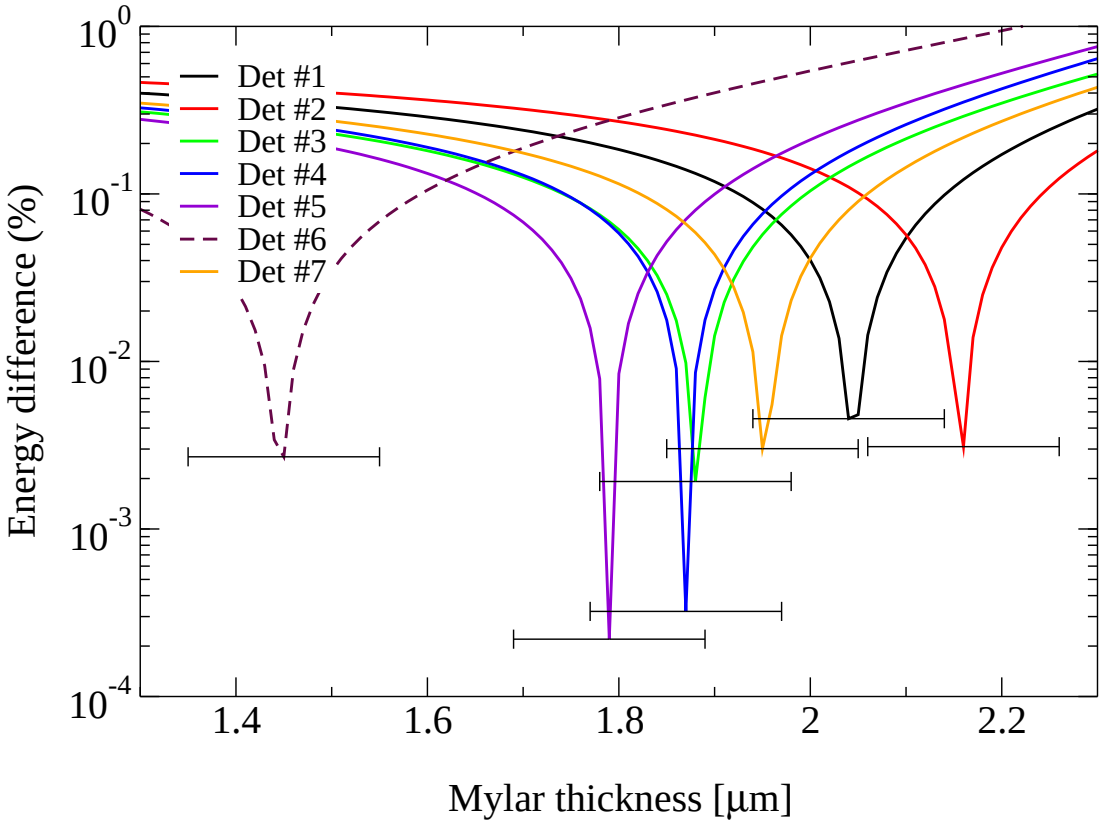

Figure 4.6 *Difference between (simulated) TRIM energies and measured energies as a function of thickness of the Mylar foils employed in the experiment, detector by detector. The aluminium layer is assumed to be 0.4 µm thick. The horizontal error bars are set to 0.1 µm and indicate the inhomogeneity of the foils. Detector #6 stopped working shortly after these measurements. Detector #7 indicates the old detector #7 (Table 4.1). See text for details of the minimisation procedure.*

be found in refs. [59, 65] respectively. The two simulations were performed independently and cross-checked against each other. Simulation A made use of the LSC [66] wrapper for GEANT4 to generate the simulation code, while simulation B employed GEANT4 directly. This section will only give a brief overview and the final results. The simulations included the two domes, the detectors, the protective foils, the target and the target holder. The setup was simulated both with and without the collimators described in section 4.3. Alpha-particle sources with energies from 1 to 10 MeV were placed in the centre of the target to mimic the effect of the two nuclear reactions. For all energies, a clear peak could be observed in every detector and the ratio of the counts in the peak over the total number of particles generated was taken as the efficiency. In this work efficiency will refer to the geometric efficiency, since silicon detectors have

Table 4.2 *Energy intervals defining the ROIs for the E_p=70 keV resonance in $^{17}O(p,\alpha)^{14}N$ for the eight detectors. Minimum (maximum) energy indicates the lower (upper) bound of the ROI.*

Detector	Minimum energy [keV]	Maximum energy [keV]
#1	160	240
#2	110	230
#3	180	290
#4	150	270
#5	190	280
#6	Not working	Not working
#7	170	270
#8	Not working	Not working

nearly 100% intrinsic efficiency [58, 63] for particle detection. The results for the two simulations are presented in Table 4.3. For the simulations, the uncertainty is set at 5% to reflect the accuracy with which the dimensions of the components of the setup[6] were known. Note that without the collimators, the efficiency of the lower row detectors is smaller than that of the upper row detectors because of the geometric shadow effects of the target holder: the bevelled edge of the target holder frame stops a fraction of the particles emitted (Fig. 4.2).

Table 4.3 *Individual efficiencies for the detectors in the upper and lower row, as obtained through different methods. R is the ratio between the efficiency values without and with collimators. See text for details.*

	Efficiency [%] without collimators	Efficiency [%] with collimators	ratio R
UPPER ROW			
Simulation A [59]	2.3 ± 0.1	0.20 ± 0.01	11.5 ± 0.2
Simulation B [65]	2.3 ± 0.1	0.21 ± 0.01	11.0 ± 0.6
^{241}Am α source	1.9 ± 0.3	0.18 ± 0.03	10.4 ± 0.5
Thick-target yield			10.1 ± 0.2
LOWER ROW			
Simulation A [59]	1.5 ± 0.1	0.20 ± 0.01	7.5 ± 0.4
Simulation B [65]	1.5 ± 0.1	0.19 ± 0.01	7.9 ± 0.4
^{241}Am α source	1.5 ± 0.2	0.19 ± 0.03	7.6 ± 0.4
Thick-target yield			8.7 ± 0.3

The two simulations were tested against the counting rate of a calibrated ^{241}Am

[6] In particular the distance between the target and the detector and the actual shape of the target holder

alpha-particle source. However, because of geometric constraints the alpha-particle source could not be placed exactly in the position of the target and the results obtained were not conclusive. The ratio R of the efficiency of the setup without collimators over that of the setup with the collimators was calculated for the simulations, the radioactive source measurements, and using the thick-target yield of the well-known resonance at E_{p}=151 keV in ^{18}O(p,α)^{15}N (see Table 3.3) using an ^{18}O-enriched target (see section 4.5). Note that the same ^{18}O-enriched target was employed for the two thick-target measurements, and that the ratio R is therefore obtained without the need to assume or measure a strength for the E_{p}=151 keV resonance.

The agreement between the simulations of the setup and the experimental measurements is excellent if the collimators are mounted, and still acceptable without collimators (Table 4.3). One possible explanation for this outcome is that since the active area of the silicon detectors is better defined with the collimators mounted, the impact of the uncertainties in the dimensions of the components of the setup (*e.g.* the actual angular aperture of the detectors) is significantly reduced. The efficiency of the setup *with* the collimators was taken from the GEANT4 simulation A [59] because of its excellent agreement with the experimental data. The efficiency of the setup without the collimators was obtained from the product of the simulated efficiency of the setup *with* the collimators and the ratio R obtained from the in-beam measurement. Since the two thick-target measurements were performed on the same target, the ratio R depends only on the yield (counts/charge) and not on, e.g. the stopping power. In addition, the thick-target yield measurements were acquired in exactly the same geometry as the rest of the in-beam data, unlike the radioactive source measurements.

In conclusion, the efficiency for the setup *with* the collimators was $0.20 \pm 0.01\%$ for both the upper and the lower row, while the efficiency of the setup *without* the collimators was $(2.02 \pm 0.10)\%$ for the upper row and $(1.74 \pm 0.10)\%$ for the lower row. The uncertainties in the efficiency with the collimators are set to a conservative 5% to reflect the uncertainty in the dimensions of the reaction chamber. The uncertainty in the efficiency without the collimators is given by summing in quadrature the 5% uncertainty in the simulations and the statistical uncertainty in the ratio R, which in turn derives from the Poisson uncertainty in the counts and a 3% uncertainty in the charge integrated.

The simulations assume that the beam hits the centre of the target and that all detectors are operational. If the beam is off-centre, one may intuitively expect

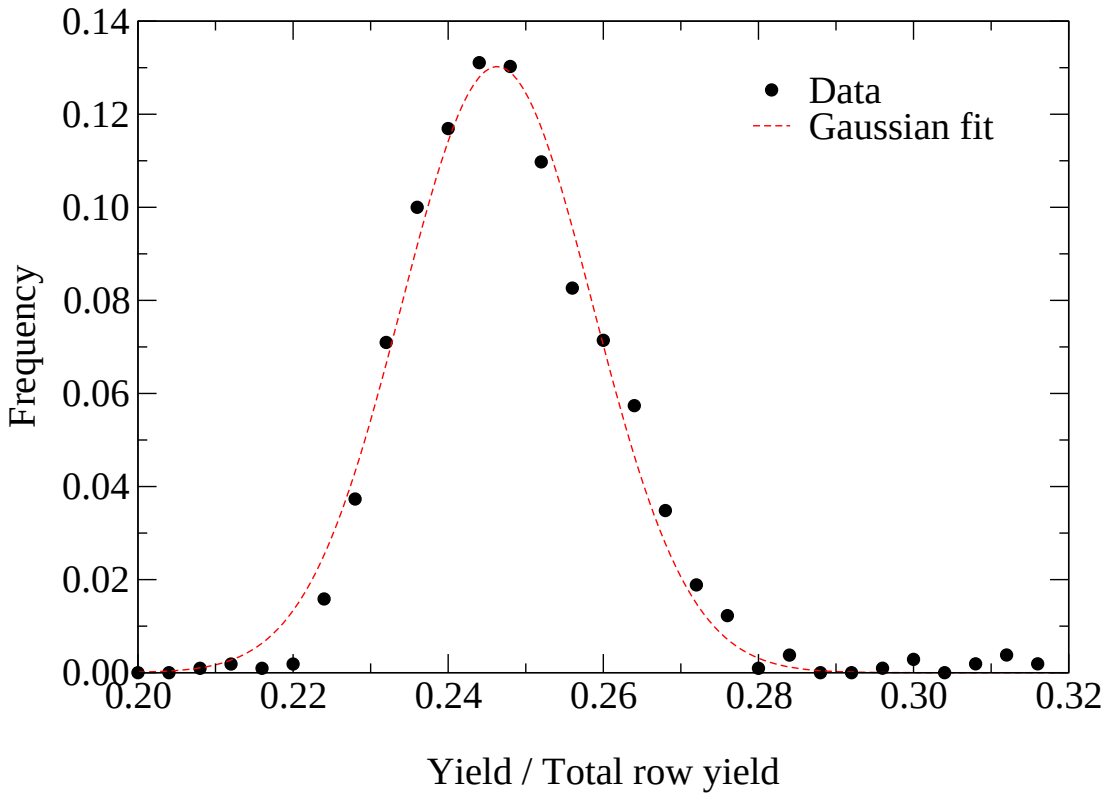

Figure 4.7 *Relative efficiency of an individual detector in the upper row as determined from the yield ratio (individual detectors yield over total upper-row yield). The distribution is Gaussian-like and can be modelled as such, with an average relative efficiency for an individual detector equal to about* $(25 \pm 1)\%$, i.e. *1/4 of the total.*

higher counting rates (i.e. higher effective efficiencies) from those detectors closer to the beam, and lower counting rates for detectors farther away. The two simulations confirmed this behaviour and showed that the increase in efficiency in one detector is compensated by the loss in efficiency in another in the same row. Thus, the overall efficiency for both rows remains constant as long as all detectors are operational. However this was not the case during the experiment as shown in Table 4.1. Assessing the position of the beamspot on the target and correcting the efficiency would involve significant uncertainties. Instead, I considered all the experimental runs acquired with four working detectors in the upper row for the E_{p}=151 keV resonance in $^{18}\mathrm{O}(\mathrm{p},\alpha)^{15}\mathrm{N}$ in thick-target yield conditions, and plotted the *relative* efficiency, that is to say the number of counts in a single detector over the total counts for the entire row. Since there are four detectors, one would intuitively expect this relative efficiency to be 25% or 1/4 of the total for each given detector. As shown in Fig. 4.7 the relative efficiency is distributed along a Gaussian-like distribution centred at 0.25. More

quantitatively, fitting the data with a Gaussian distribution results in an effective efficiency of $(25 \pm 1)\%$. Therefore, in principle, for all experimental runs where one or more detectors were missing the uncertainty on the efficiency should have been increased taking into account this additional source of error. However, this additional uncertainty turned out to be negligible compared to the other sources of systematic uncertainty in all cases.

4.5 The Ta_2O_5 targets

4.5.1 Target preparation

The method to produce the targets used during the experimental investigation of the ^{17,18}O(p,α)^{14,15}N reactions was originally developed during the campaign aimed at measuring the ^{17}O(p,γ)^{18}F reaction at LUNA [67, 68] and details on the target characterisation performed at the time can be found in ref. [56]. Isotopically enriched Ta_2O_5 targets were produced by anodic oxidation of a tantalum backing. Tantalum was chosen as a backing for its purity[7], good eletrical conductivity and stability under beam. Tantalum backings were first cleaned in an acid bath [56] to further decrease the surface contaminants from other elements, in particular fluorine. The backings were then placed in a liquid solution containing water, enriched either in ^{17}O or ^{18}O or both, and an electrolyte (KI) to improve the electrical conductivity of the liquid solution. A gold-plated anode was placed at a set distance over the liquid solution and given a negative bias with respect to ground, while the tantalum backing served as the cathode. The thickness of the Ta_2O_5 thin layer depends on the voltage, the distance and the length of the process. After production, the targets were tested under proton beam bombardment. Fig. 4.8 shows a picture of a target after being dismounted.

Six target batches were produced employing different enriched-water solutions, resulting in different ^{17}O/^{18}O isotopic abundances. In order to precisely determine the isotopic abundances of the targets, one target for every batch was sent to the Laboratori Nazionali di Legnaro, Italy for Secondary ion mass spectroscopy (SIMS) analysis as described in ref. [56]. For the target stoichiometry (*i.e.* Ta:O ratio), we employed the 0.39 value obtained experimentally in ref. [56] for all

[7]Lack of contaminants from other elements, especially light elements on which the beam may react producing beam-induced background.

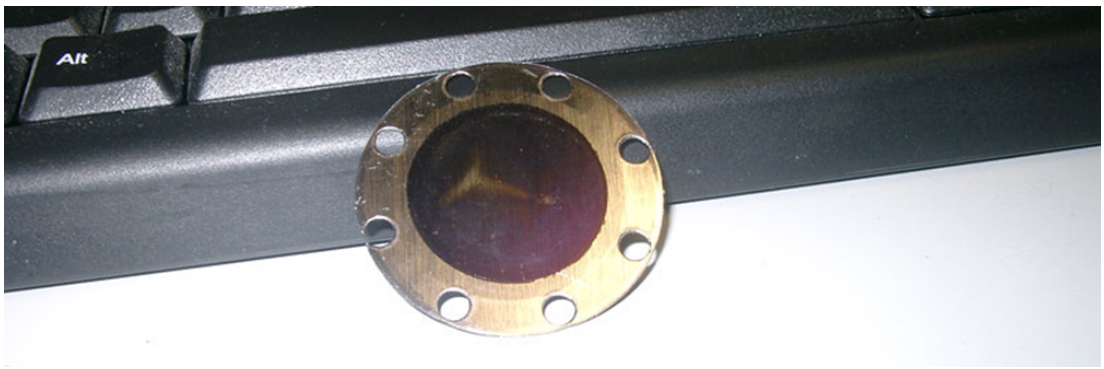

Figure 4.8 *A picture of a target after being dismounted from the beamline. The purple colour is due to the thin-film effect. The golden star-shaped mark is the beamspot.*

batches. See Table 4.4 for more information on the six batches.

Table 4.4 *The isotopic abundances of the six batches of targets used in the two experimental investigations, "# targets" indicates the number of targets produced for a specific batch. For every batch, the isotopic abundances have been obtained from SIMS analysis [56] performed on a single target from that batch.*

Batch	# targets	^{18}O isot. abundance	^{17}O isot. abundance
1	6	4.3±0.1%	84.4±0.4%
2	6	5.2±0.2%	81.3±0.6%
3	3	7.7±0.2%	78.4±0.6%
4	5	6.7±0.2%	77.8±0.6%
5	9	93.1±0.5%	-
6	19	91.7±0.6%	-

4.5.2 Target thickness measurements

The thickness of a target is a critical parameter to determine how to extract nuclear physics information from the experimental data acquired. For instance, if the aim is to carry out a thick-target yield measurement of a resonance, the target has to be significantly thicker than the resonance width (Section 2.2). Targets from batches 1 – 5 were employed for the commissioning of the setup and for the ^{17}O(p,α)^{14}N experimental campaign, which involved the measurement of three resonances in thick-target yield conditions. The three resonances were the E_{p}= 70 and 193 keV in ^{17}O(p,α)^{14}N and the E_{p}= 151 keV in ^{18}O(p,α)^{15}N. Out

of these three, the E_{p}= 70 keV state has the largest total width ($\Gamma \simeq 130 \pm 5$ eV [69]) and to ensure thick-target yield conditions, 5 keV at $E_{\mathrm{p}} = 200$ keV was chosen as the target thickness.
Targets from batch 6 were instead employed during the ^{18}O(p,α)^{15}N experimental campaign. In this investigation, the study was focused on both the resonant and the non-resonant components of the cross-section. Part of the investigation was carried out using ∼5 keV thick targets again. However, when measuring a resonance at E_{p}= 95 keV in ^{18}O(p,α)^{15}N, an unexpected behaviour was observed in the yield, which was attributed to the presence of a resonance wider than the thickness of the targets used. For this reason, ∼15 keV thick targets (for 200 keV protons) were produced and employed in the investigation at energies below $E_{\mathrm{p}} \simeq 140$ keV. See Chapter 6 for further details.
In order to monitor the target thickness and stability with beam, all targets were produced with a small amount of ^{18}O-enriched water allowing us to perform frequent thick-target resonance scans at E_{p}= 151 keV of the ^{18}O(p,α)^{15}N reaction. A scan of the resonance was performed immediately after mounting the target and typically every 5 C of charge and just before dismounting. A set of scans performed on one target is shown in Fig. 4.9.

Each of these scans was fitted with an empirical function to extract the resonant energy, the height of the plateau, and the thickness of the target:

$$f(E) = H \frac{1}{\left[1 + \exp\left(\frac{E_{\mathrm{R}} - E}{\delta_L}\right)\right]} \frac{1}{\left[1 + \exp\left(\frac{E - E_{\mathrm{R}} - \Delta E}{\delta_R}\right)\right]} \tag{4.2}$$

where H is the height of the plateau, E_{R} is the resonant energy in the laboratory frame, E is the beam energy, ΔE is the thickness of the target in energy units (the same units as E), and $\delta_{L,R}$ are two empirical parameters that account for the straggling at the target boundaries in the rising and falling front respectively. Eq. 4.2 is closely related to Eq. 2.11 and was successfully employed in previous investigations [68] to fit the same type of targets. In Fig. 4.9, the units on the y-axis are chosen so that the value of the parameter H in Eq. 4.2 gives the strength of the resonance in eV. This was achieved simply by using Eq. 2.11, where the efficiencies are those calculated in Section 4.4 and the stopping power provided by SRIM [11]
Resonant energies extracted from these fits are plotted in Fig. 4.10. Carbon deposition was observed on two groups of target, which have been omitted from Fig. 4.10. The first group consists of two targets, which were mounted during,

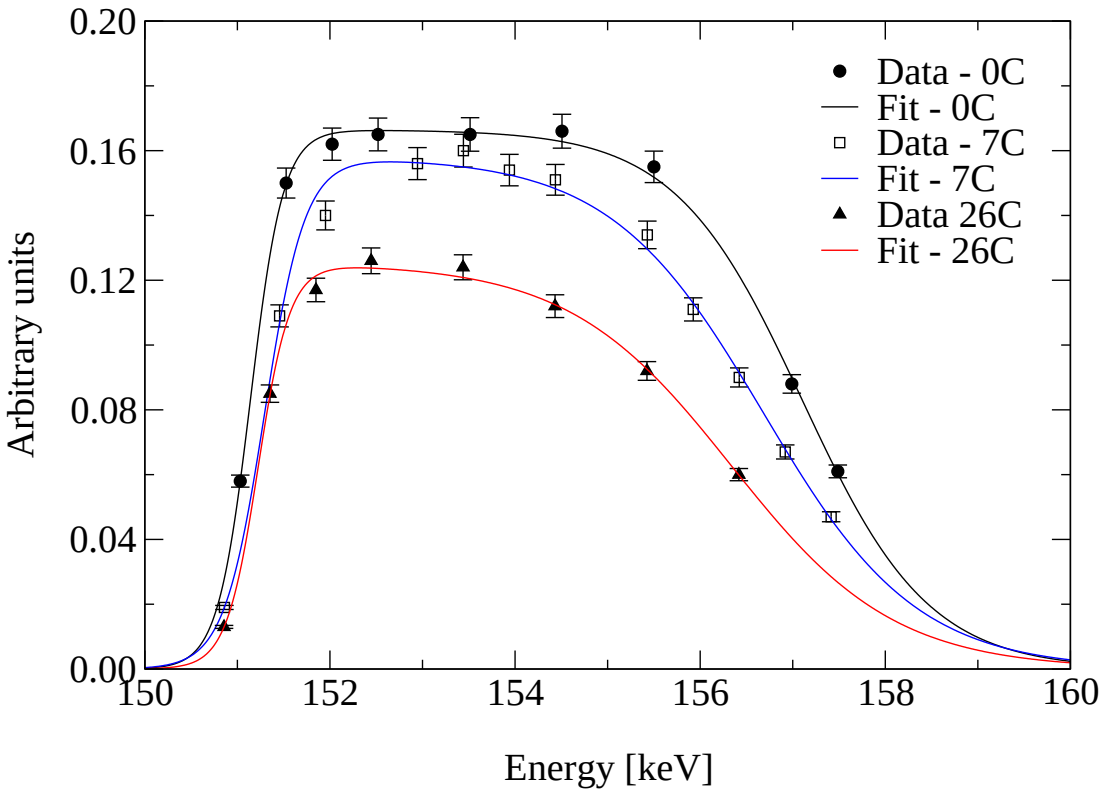

Figure 4.9 *A set of measurements of the E_p=151 keV resonance in the $^{18}O(p,\alpha)^{15}N$ reaction in thick-target yield conditions. Error bars are a combination of Poisson statistic and random uncertainty on the charge deposited. Fits to the scan using Eq. 4.2 are shown. Note that the shift in the rising front is within the uncertainties of the fit.*

and immediately after, a carbon-based spray sealant was used to fix a leak in the chamber. The carbon residues were eventually eliminated from the chamber after flushing it with nitrogen a few times. The second group consists of three targets which were produced with enriched-oxygen water that was contaminated with carbon. The contamination was likely due to residuals of tap water incorrectly used to clean the target production station. Aside from these targets, no evidence of carbon deposition was observed. The error bars in Fig. 4.10 are statistical only, and derive from the fit. The scatter of the data in Fig. 4.10 is essentially Gaussian, as expected. However the systematic uncertainty in the energy of the beam (ΔE_p = 0.3 keV [54]) dominates over the statistical uncertainty. The average resonant energy value was $E_p = 151.2 \pm 0.3_{syst}$ keV[8], which is in excellent agreement with the literature value $E_p = 150.9 \pm 0.1$ keV reported in ref. [51].

[8]The statistical uncertainty in the resonant energy is just $\pm 0.002_{stat}$ eV

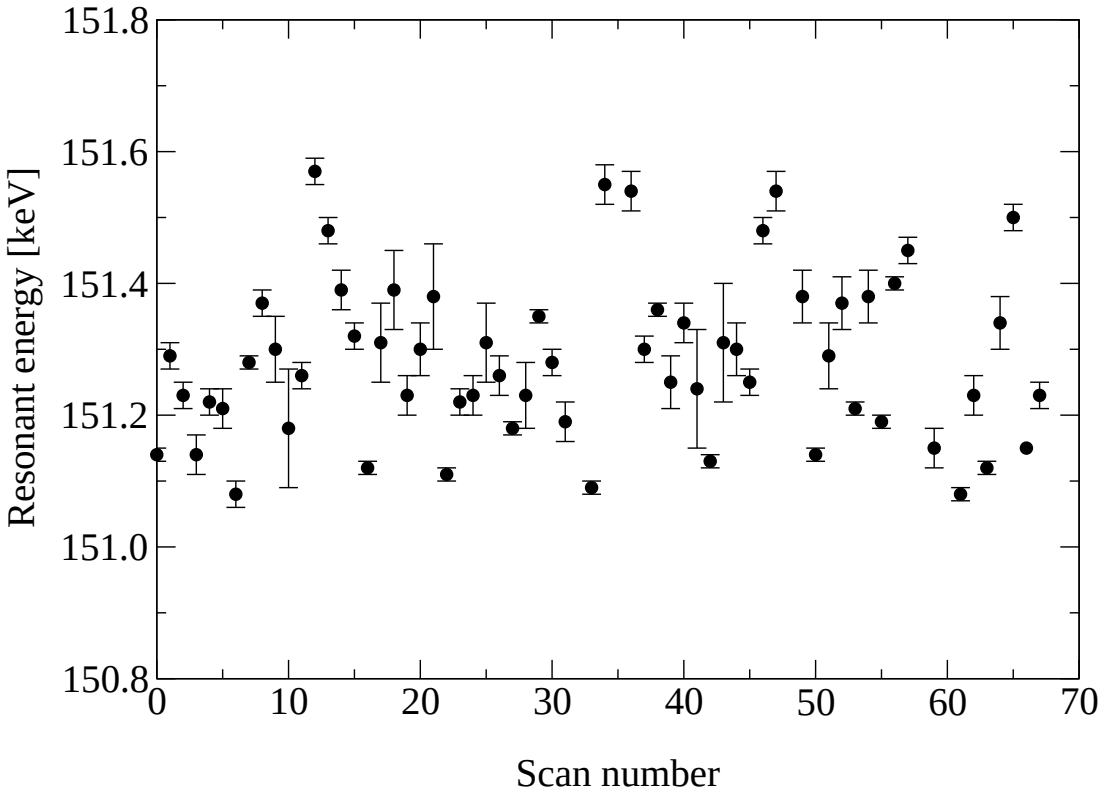

Figure 4.10 *Resonant energy for the E_{p}=151 keV in $^{18}O(p,\alpha)^{15}N$ as measured during the two experimental investigations. The uncertainties shown derive from the fits. Note that the systematic uncertainty in the beam energy is 0.3 keV, which dominates over the statistical uncertainties shown.*

4.5.3 Target degradation

Qualitatively, we observed that the targets degraded as charge was accumulated on them. I performed some analyses in order to assess how often the target had to be changed and to quantitatively investigate the impact of the degradation of the targets under beam on our results. First, I plotted the relative heights of the plateau from Eq. 4.2 against the charge deposited on the target. Relative heights here are the heights H of the plateau obtained fitting Eq. 4.2 to the resonance scan of a target irradiated with a set amount of charge, divided by the same quantity obtained for the same "fresh" target, i.e. before irradiation. The amount of charge deposited on the target while performing the resonance scan is negligible ($\ll$ 1 C). A linear model can be employed to parametrise the degradation in heights of the targets as shown in Fig. 4.11. The slope parameter of this line of best fit (reduced chi-square $\tilde{\chi}^2 = 4.3$) corresponds to a degradation of (0.48 ± 0.05) % per C of charge on target. This linear function is just an

empirical, approximate model, and is not expected to result in a statistically excellent fit. A reduction of the height of the plateau could be linked to either a change in the stoichiometry of the target or a change in the abundance of the ^{18}O content. SIMS analyses performed on two used targets indicated that the isotopic enrichments shown in Table 4.4 decrease after beam bombardment. Only two targets could be analysed with SIMS after beam bombardment, which may give a skewed picture of the real target degradation. Therefore, to model the degradation of all targets I opted to employ the linear model presented that fits all targets used.

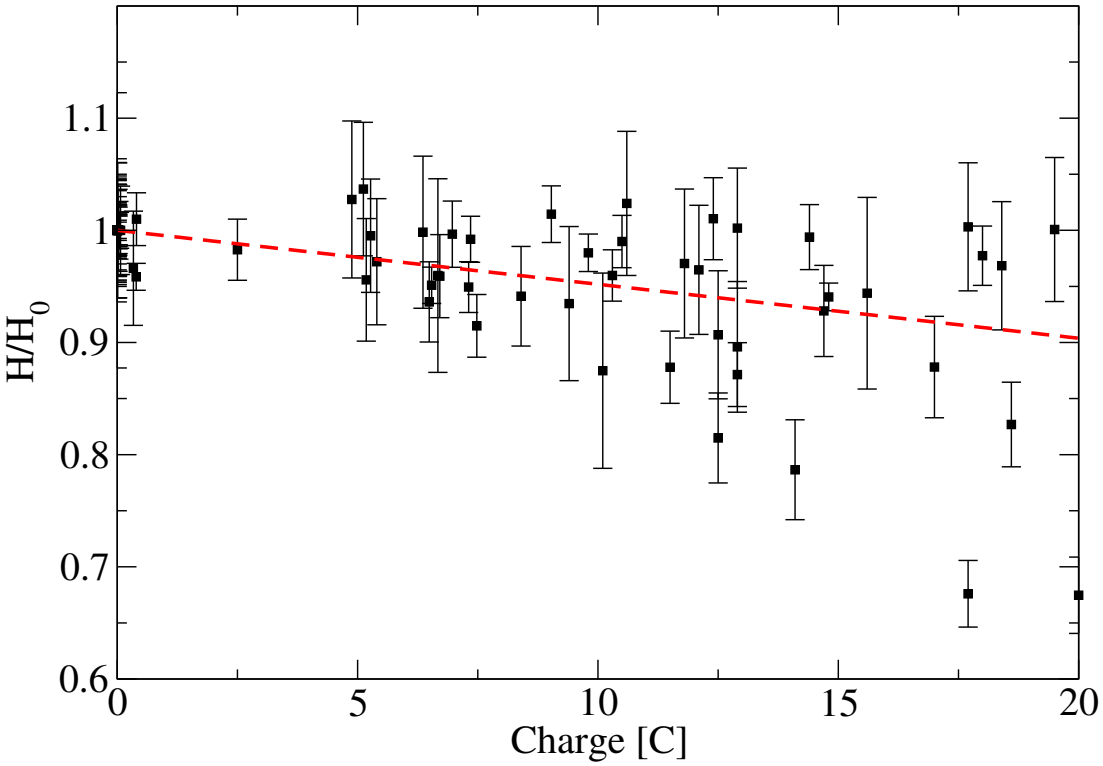

Figure 4.11 *Relative plateau height of the targets employed for the two experimental investigations shown as a function of the charge deposited on the target. Relative height refers to the ratio of actual height H and the height measured on the fresh target H_0. Uncertainties shown are statistical only. The best fit is shown as a dashed red line.*

In addition to the reduction in height of the plateau, we observed a reduction in the thickness of the targets with charge deposited. I analysed this effect to quantify the amount of charge that could be safely deposited on a target on average. A reduction in thickness is typically due to the target being sputtered away by the beam. Specifically, the protons sputter the light ^{18}O atoms, either

outside of the target or further inside, reducing the effective target thickness. Note thickness value does not affect the derivation of resonance strengths measured in thick-target yield conditions as long as the thick-target yield conditions are satisfied 2.2. To quantify this reduction, the relative thickness of the targets was plotted against the charge deposited. Relative thickness is, just like before, the actual thickness over the thickness of the fresh target. The data, shown in Fig. 4.12 was again approximated with a linear function ($\tilde{\chi}^2 = 8.2$) with a linear function, for which the degradation in thickness of the target is approximately $(0.53 \pm 0.4)\%$ per C. The statistical quality of the fit is relatively poor, but note again that this is just a single-parameter empirical model and cannot reproduce accurately the real physics of the target degradation.

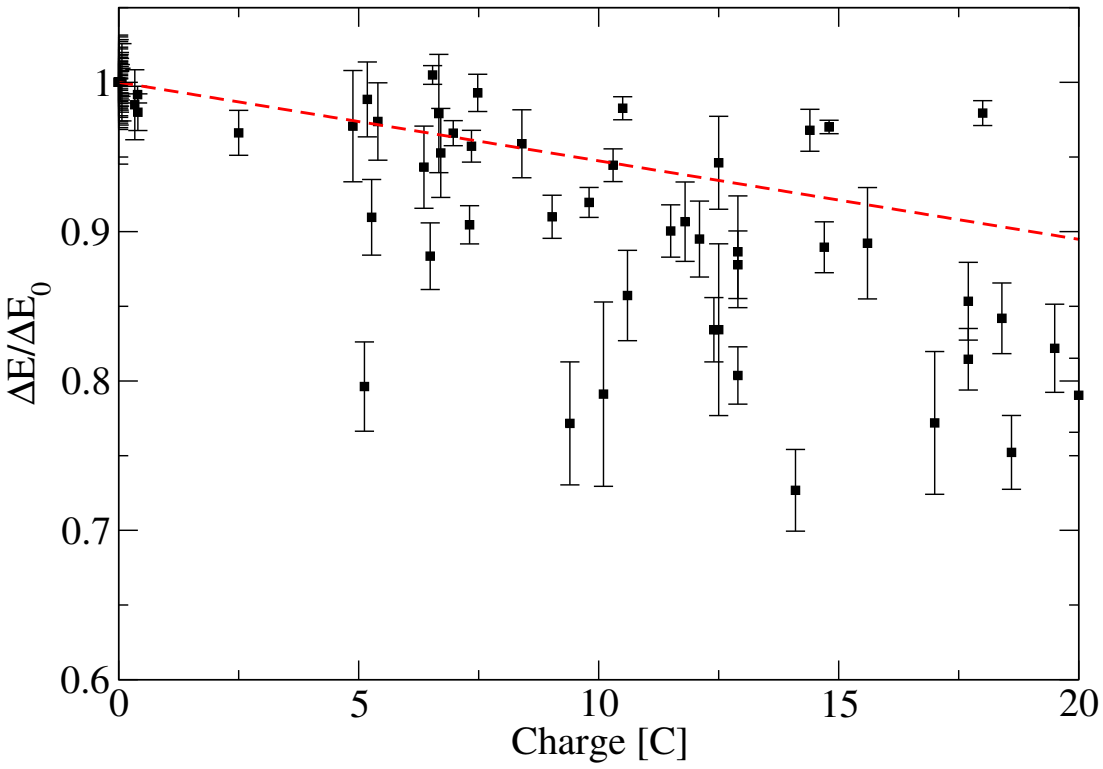

Figure 4.12 *Relative target thickness (actual thickness ΔE over fresh target thickness ΔE_0) as a function of deposited charge on the target. Uncertainties shown are statistical only. The best fit is shown as a dashed red line.*

Targets were dismounted after 20 C of charge, thus both the model for the degradation of the height and that for the degradation of the thickness were only approximated with a linear function up to 20 C of charge deposited. At 20 C the degradation of the target is approximately 10% in both plateau height and thickness, a modest correction that has small uncertainties compared to those of

the stopping power (see e.g. Table 4.5).

4.6 Commissioning

The final commissioning of the setup consisted in an absolute measurement of the cross-section of the $E_{\mathrm{p}} = 151$ keV resonance in the ^{18}O(p,α)^{15}N reaction. Recall that units in the fits in Fig. 4.9 have been chosen so that the plateau height parameter H in Eq. 4.2 is just the $\omega\gamma$ value of the resonance being investigated. A weighted average of the H values (= resonance strengths) for fresh targets only was calculated batch by batch. The results are shown in Fig. 4.13, against the literature value in ref. [51]. The weighted average of the six values is $164.2 \pm 0.9_{\mathrm{stat}} \pm^{12.1}_{11.7\ \mathrm{syst}}$ meV. This final average as well as the six batch averages obtained are in excellent agreement with $\omega\gamma = 167 \pm 12$ meV reported in ref. [51]. See table 4.5 for the sources of uncertainty. The excellent agreement between the results gave us confidence that the setup had been successfully commissioned.

Table 4.5 *Uncertainty budget for the $\omega\gamma$ of the E_{p}=151 keV resonance strength, $\omega\gamma$, in the $^{18}O(p,\alpha)^{15}N$ reaction. Statistical uncertainty refers to the random sources of error (Poisson and charge integration). The other sources of error are systematic. See appendix A for details on the tail asymmetry.*

Source	Percent uncertainty
Statistical	±0.6%
Charge	±2.0%
Tail asymmetry	+2.0%
Stopping power	±4.0%
Efficiency	±5.5%

4.7 Background reduction underground

The benefits of moving underground in order to reduce the background in scintillators and solid-state detectors for gamma spectroscopy experiments are very well known (e.g. refs. [54, 55]). However the effects of an underground environment on charged particle spectroscopy experiments with silicon detectors are not as well-established. Previous studies performed in the Laboratori

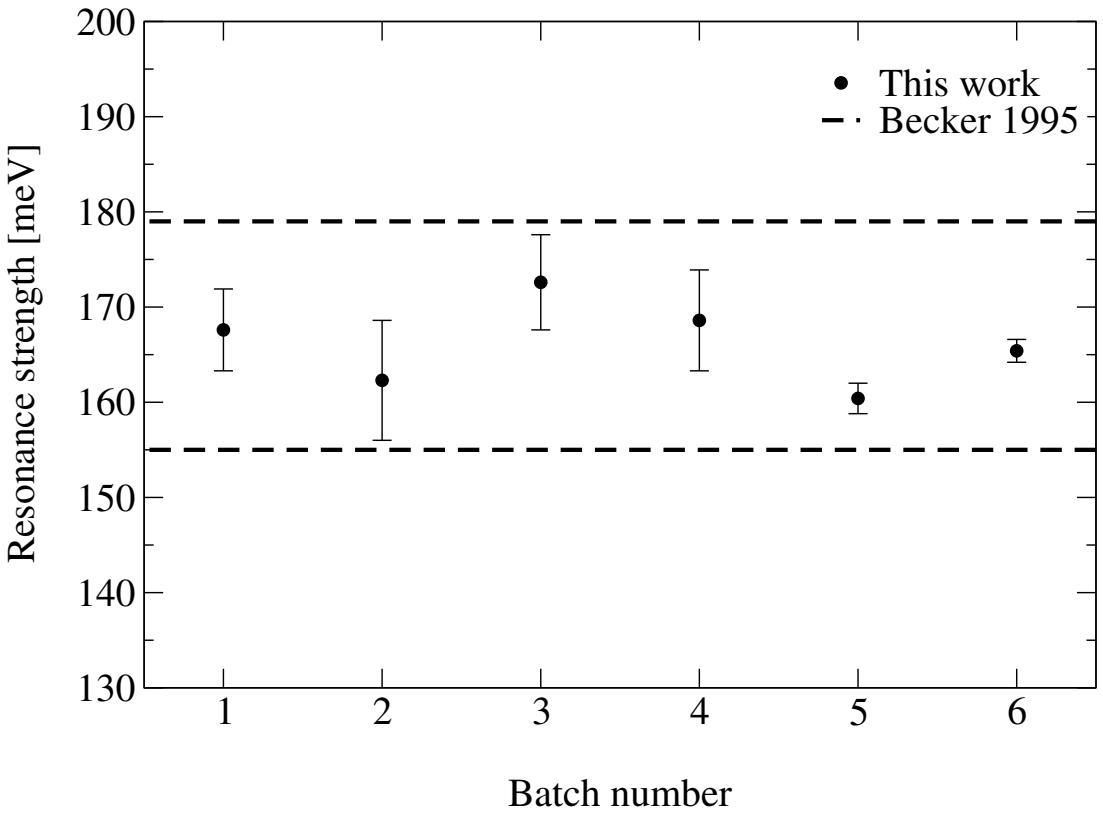

Figure 4.13 *Weighted average of the strength of the $E_p = 151$ keV resonance in the $^{18}O(p,\alpha)^{15}N$ reaction as obtained from targets of the six batches used. Error bars include uncertainties in charge deposited and isotopic abundances, as well as statistical uncertainties. The six $\omega\gamma$ values are in excellent agreement with that reported in Becker 1995 [51].*

Nazionali del Gran Sasso [70, 71] indicated a somewhat significant reduction at detected energies above 500 keV. However the background suppression in the region below 500 keV, of particular interest in the $^{17}O(p,\alpha)^{14}N$ campaign, had never been investigated in detail to my knowledge. In order to quantify this background reduction, I carried out a systematic comparison of the background in the setup described in this chapter. Natural background data was acquired underground in Gran Sasso and overground in Edinburgh. Both underground and overground, background measurements were performed with and without a partial 5 cm lead shield around the setup, shown in Fig. 4.14. During these background tests, detectors #1 through #5 were working and their summed spectra are shown in Fig. 4.15, with rates given in Table 4.6.

The four spectra can be broadly divided in three energy regions. In the region below 2 MeV roughly, the background has an exponential-like trend and is

Figure 4.14 *The experimental setup with the partial lead shield used for the measurements (left) underground in Gran Sasso, mounted on the LUNA second beamline, and (right) overground in Edinburgh.*

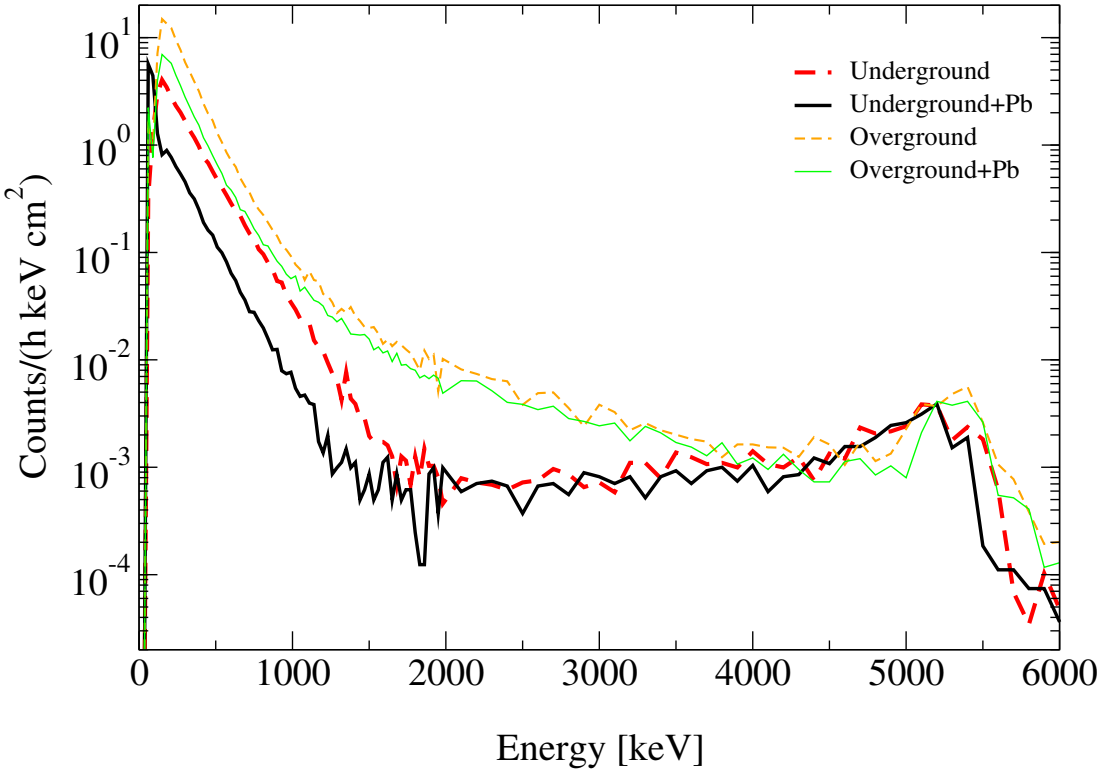

Figure 4.15 *Comparison of natural background observed underground in Gran Sasso and overground in Edinburgh, with and without a partial lead shield. The spectra shown were obtained by summing calibrated spectra of the working detector (#1–5). The peak around 5 MeV likely arises from intrinsic alpha activity of the silicon detectors.*

reduced both by the underground environment and by the presence of the partial lead shield. This behaviour is consistent with Compton-generated electrons due to environmental gamma activity or from high-energy charged particles (e.g. cosmic muons). The lead shield appears to be more effective underground than overground, probably because deep underground high-energy charged particles are essentially absent. Therefore, compared with overground, a larger fraction of the low-energy background is due to gamma rays, which a lead shield is especially suitable to suppress. In particular, in the ROI for the $E_{\rm p}$=70 keV resonance in the ^{17}O(p,α)^{14}N reaction (E_α=200 keV see section 4.3) the reduction in natural background is as much as a factor of 15 between unshielded overground and shielded underground.

In the region between 2–4 MeV, the background seems to be strongly suppressed by the underground location, but not by a lead shield and the physical origin of the natural background in this region is not immediately obvious. The tail from the peak at 5 MeV plays a role, which is especially prominent underground. In the region of interest for the signal of the ^{18}O(p,α)^{15}N reaction ($E_\alpha \simeq$2.2 MeV), the background reduction is approximately a factor of 20.

Finally, in the energy region above 4 MeV and below the dynamic range limit of 6 MeV, the background is not reduced underground or by the presence of a lead shield. The most likely physical source of the prominent peak at 5 MeV is intrinsic activity of the detector. In other words, a small amount of a radioactive isotope unstable to alpha-decay could be present in the bulk of the detector, as previously proposed in ref. [71]. It is worth mentioning explicitly that 5 MeV is a very common energy for alpha-decaying isotopes and, given the resolution of the detector, it is not possible to identify the isotope in question.

These results confirm the significant advantages in moving underground to perform alpha spectroscopy experiments employing silicon detectors, even at very low energy ($<$ 1 MeV) where no data existed before.

Table 4.6 *(Top) Background rates in 10^{-3} counts/(h keV cm^2) for the shielded and unshielded setups, underground at LUNA (UG) and overground in Edinburgh (OG). At energies below 180 keV, contributions from electronic noise cannot be excluded. (Bottom) Background suppression factors with respect to overground unshielded background.*

ROI [MeV]	0.18–0.4	0.4–0.7	0.7–1.2	1.2–2.0	2.0–3.0	3.0–4.0	4.0–6.0
OG	157.9	25.89	3.139	0.414	0.107	0.041	0.037
OG+Pb	74.39	12.96	1.886	0.302	0.084	0.036	0.029
UG	41.52	9.358	1.276	0.061	0.015	0.021	0.030
UG+Pb	11.17	2.212	0.251	0.018	0.014	0.017	0.026
OG	1	1	1	1	1	1	1
OG+Pb	2	2	2	1	1	1	1
UG	4	3	2	7	7	2	1
UG+Pb	14	12	13	23	8	2	1

Chapter 5

The ^{17}O(p,α)^{14}N campaign

The primary objective of this experimental campaign was the measurement of the astrophysically important E_p=70 keV resonance. The experimental setup was commissioned as detailed in the previous chapter. In particular, the Regions Of Interest (ROIs) for the E_p=70 keV resonance were obtained using an effective minimisation procedure, based on the energy of the alpha peaks originating from the E_p=193 keV resonance in ^{17}O(p,α)^{14}N and the E_p=151 keV resonance in ^{18}O(p,α)^{15}N.

The first part of this chapter presents a new absolute measurement of the strength of the relatively well-known (chapter 3) E_p=193 keV resonance in ^{17}O(p,α)^{14}N, performed as an additional commissioning test. The rest of the chapter describes in detail the experimental campaign aimed at measuring the E_p=70 keV resonance, including the analysis framework employed (sections 5.2.2), the data taking procedure (section 5.2.5), and the data quality tests (sections 5.2.6 and 5.2.7). The calculation of the resonance strength value of the E_p=70 keV resonance is performed in section 5.2.8, and our updated rate of the ^{17}O(p,α)^{14}N is given in section 5.3.

Results from this chapter have been published in refs. [53, 72].

5.1 The E_p=193 keV resonance

A weighted average of all previous measurements of the E_p=193 keV resonance in ^{17}O(p,α)^{14}N results in $\omega\gamma = 1.67 \pm 0.17$ meV [31]. Based on this value and

Eq. 2.11, the expected counting rate in the setup with the collimators (section 4.3) for a single detector was

$$\frac{N_\alpha}{Q} = \omega\gamma \frac{\eta W \lambda_r^2}{2\epsilon_r^{\text{eff}}} e \simeq 1\,\text{cnt}/\mu\text{C} \simeq 100\,\text{cnts/s} \tag{5.1}$$

where N_α is the number of detected events, Q is the charge (in μC), $\eta = 0.02$ is the efficiency, W is a parameter accounting for the angular distribution, $\lambda_r^2 = 2.36 \times 10^{-27}\,\text{m}^2$ is de Broglie's wavelength squared at the resonant energy in the CM frame, $\epsilon_r^{\text{eff}} = 3.28 \times 10^{-18}\,\text{eV}\,\text{m}^2/\text{atoms}$ is the effective stopping power in the CM frame and $e = 1.60 \times 10^{-19}\,\text{C}$ is the fundamental charge. A typical beam intensity of $I = 100\mu\text{A} = 100\mu\text{C/s}$ has been assumed. The coefficients W were calculated using the results from ref. [29], in which they were determined experimentally. Thanks to a rate as high as 100 counts/s per detector, a single target from batch #5 (Table 4.4) was sufficient to acquire the final data for the E_p=193 keV resonance. This target was the representative target from batch #5 to be sent for SIMS analysis. A sample spectrum of the alpha peak of the E_p=193 keV resonance is shown in Fig. 5.1, where the fitting functions are those described in appendix A. These fitting functions were deemed unreliable in this case because the tail of the alpha peak is completely covered by the low-energy beam-induced background. Thus, rather than extracting the number of counts from the fits shown, a simple integral of the peak was used to estimate the number of counts. An asymmetric +2% uncertainty was added to the integral to account for the contribution of the unseen low-energy tail. See appendix A for further details.

A thick-target scan of this resonance, shown in Fig. 5.2, was performed in order to extract the $\omega\gamma$ from Eq. 2.11. A fit of the height of the plateau was performed using Eq. 4.2, and the resonance strength was obtained using the same parameters as in Eq. 5.1. All four upper row (135°) detectors were working at the time of this measurement, but only two of the lower row (102.5°) detectors were operational. In order to reduce the systematic uncertainty due to the two missing detectors (see section 4.4), only data from the upper row were considered. The increase in statistical uncertainty due to this choice is negligible. Finally we obtain $\omega\gamma = 1.68 \pm 0.03_\text{stat} \pm 0.12_\text{syst}$ meV, in excellent agreement with the value reported in ref. [31]. The uncertainty budget is reported in Table 5.1.

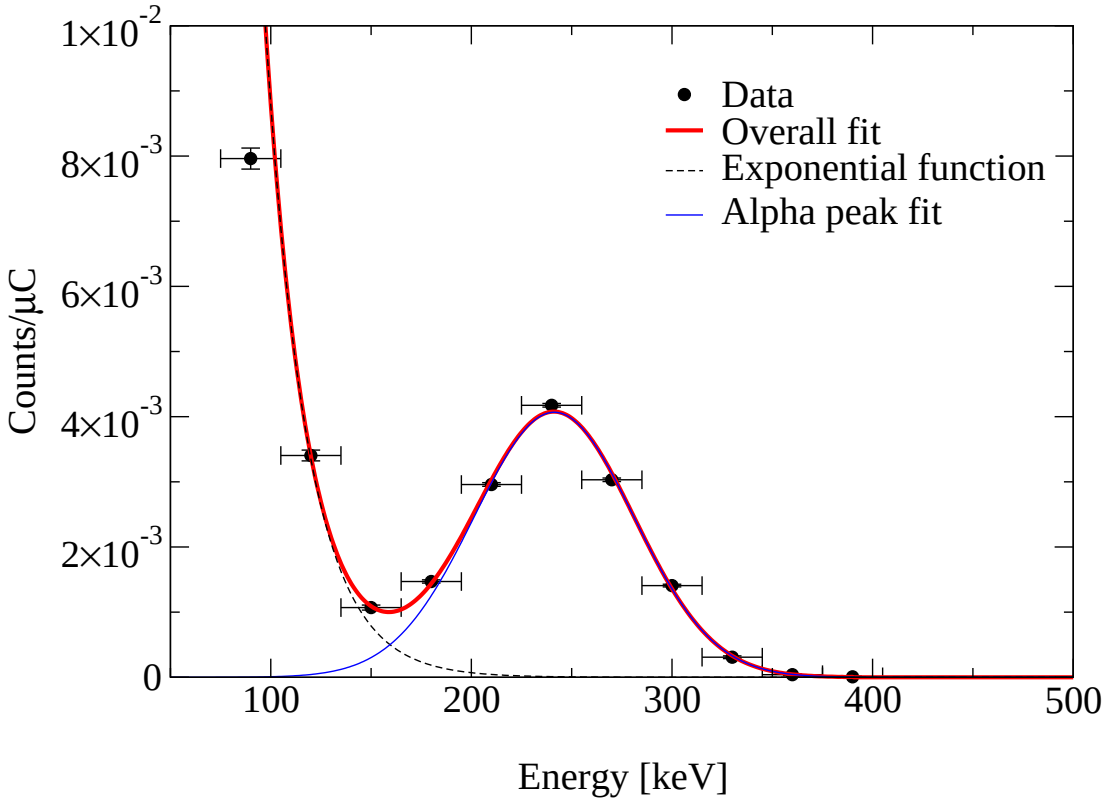

Figure 5.1 *A typical spectrum acquired at E_p=193 keV, showing a prominent alpha peak for the E_p=193 keV resonance in $^{17}O(p,\alpha)^{14}N$. Vertical error bars are statistical only, horizontal error bars show the bin size (30 keV). The fitting functions are described in detail in appendix A. Note however that the number of counts in the peak N_α was obtained from a simple integration. See text and appendix A for details.*

Table 5.1 *Uncertainty budget for the $\omega\gamma$ of the E_p=193 keV resonance in $^{17}O(p,\alpha)^{14}N$. Only data from upper row detectors is considered. Statistical uncertainty refers to the random sources of error (Poisson and charge integration). The other sources of error are systematic.*

Source	Percent uncertainty
Statistical	±1.9%
Charge	±2.0%
Tail asymmetry	+2.0%
Stopping power	±4.0%
Efficiency	±5.0%

5.2 The E_p=70 keV resonance

Previous investigations [33, 39] suggested that the strength of the E_p=70 keV in $^{17}O(p,\alpha)^{14}N$ was of the order of a few neV. Five detectors (#1–5 and #7)

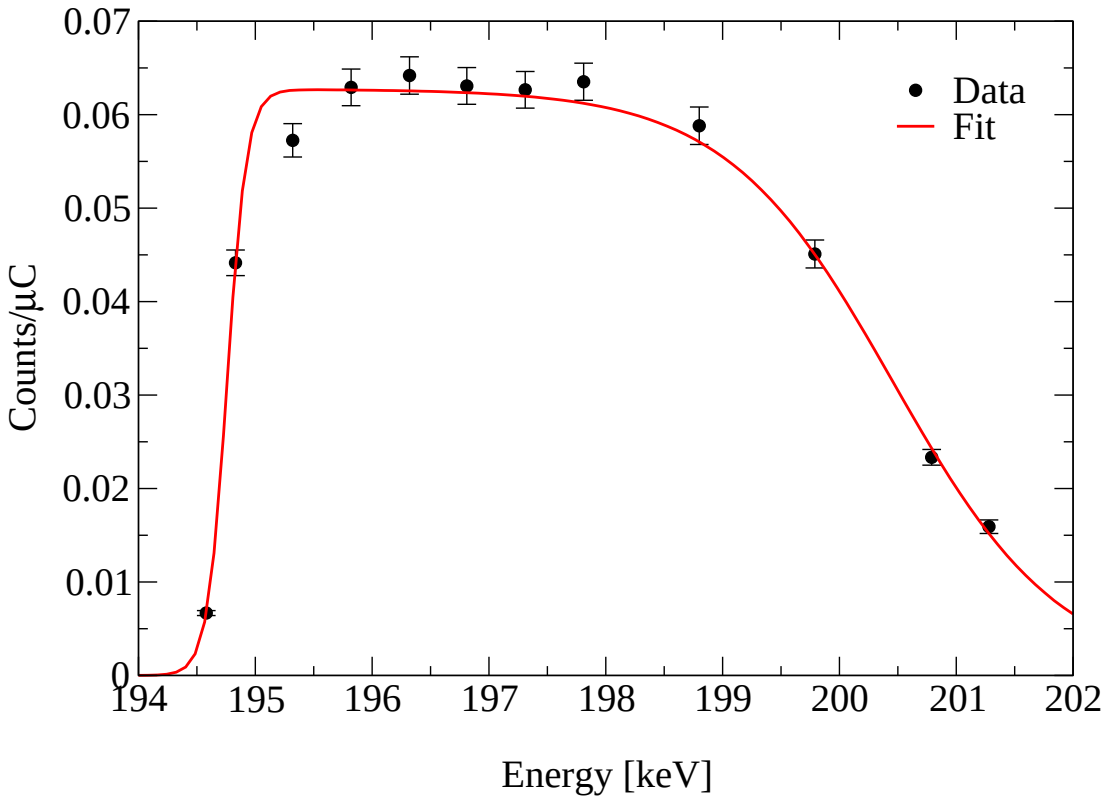

Figure 5.2 *The thick-target yield scan of the E_p=193 keV resonance in $^{17}O(p,\alpha)^{14}N$, performed with a 5 keV thick target. This is the first complete scan of this resonance, as previous investigations [31] were hampered by the beam-induced background at high beam energies.*

were working by the time the data taking for this resonance started, and in order to maximise the detection efficiency, the collimators were removed. Employing Eq. 2.11 to obtain an estimate equivalent to that in Eq. 5.1, one finds a counting rate of the order of ∼2 counts/h for the entire setup, depending on the adopted literature value for the strength. Knowing the expected detection energy of the alpha particles produced by the resonance (sec. 4.3) and the natural background (sec. 4.7), one could expect a total natural background of the order of ∼70 counts/h in the region of interest. Based on these estimates, the signal to background ratio was expected to be as low as 1:35.

5.2.1 The choice of foils

In light of this extremely low signal to background ratio, it is now worth re-assessing the decision of measuring the E_p = 193 keV and E_p = 70 keV resonances using the same foils taken in section 4.3. In principle one possible

solution to improve the signal to background ratio could have been to reduce the thickness of the foils mounted in order to increase the detected energy of the alpha particles and reduce the natural background in the ROI (section 4.7). However, three potential issues were found with this approach. First, as explained in section 4.3, changing the foils would have changed the ROI for the $E_{\rm p}$=70 keV resonance. While in principle one could determine the ROI using other reactions at suitably lower proton energies as in ref. [33], employing the $E_{\rm p}$=193 keV resonance in ^{17}O(p,α)^{14}N was deemed the most accurate way. Second, reducing the thickness of the foils could introduce a scattering-induced background as seen at $E_{\rm p}$ = 193 keV at lower proton energies, and in particular at $E_{\rm p}$ = 70 keV. Reliably predicting this scattering-induced background is extremely difficult because of the inhomogeneity of the foils, and even a few spurious beam-induced counts per hour would be enough to mask the weak signal. Third, in order to monitor the status of the target, the $E_{\rm p}$=151 keV resonance in ^{18}O(p,α)^{15}N was frequently measured. To be able to carry out this vital check of the stability of the setup, one would in any case have to mount foils thick enough to protect the detectors from $E_{\rm p}$=151 keV protons. However, at the time of the start of the data taking, the thinnest *commercially available* foils capable of stopping $E_{\rm p}$=151 keV protons were nominally of the same thickness as those used to measure at $E_{\rm p}$=193 keV. Ultimately the decision taken in section 4.3 was not changed, and 2.0+0.4 μm aluminised Mylar foils were employed throughout the entire experimental campaign. Carrying out the measurement overground using these 2.4 μm foils would have been impossible, as the signal to background ratio could have been as low as 1:500 (recall the factor 15 background reduction underground, sec. 4.7). In other words by mounting foils comparatively thicker than those used in other campaigns [33], we exploited the low natural background in Gran Sasso to reduce the systematic uncertainties in the measurement.

5.2.2 Target degradation

In order to extract a resonance strength from the data, I will consider several experimental runs acquired with different targets in different degradation conditions (sec. 4.5). In principle, one could use Eq. 2.11 to obtain a resonance strength, and since we will be considering several experimental runs at the same

time, one possible way to proceed would be to write

$$\omega\gamma_{\text{best}} = \frac{\Sigma_i^N (\omega\gamma)_i Q_i}{\Sigma_i^N Q_i} = \frac{\Sigma_i^N \left(\frac{N_\alpha \epsilon e}{\eta W \frac{\lambda^2}{2} Q} \right)_i}{\Sigma_i^N Q_i} \tag{5.2}$$

where Q is the charge deposited on the target (in Coulomb), N_α is the number of alpha particles detected, ϵ is the stopping power, e is the fundamental charge, η is the efficiency, W is a parameter that accounts for angular distributions, $\frac{\lambda_r^2}{2}$ is de Broglie's wavelength in the CM frame at the resonant energy, and the sum over i is performed on N experimental runs. If one can assume that the stopping power, the efficiency, the angular distribution and de Broglie's wavelength are constant over the N runs, one can rewrite Eq. 5.2 as

$$\omega\gamma_{\text{best}} = \frac{\epsilon e}{\eta W \frac{\lambda^2}{2}} \frac{\Sigma_i^N \frac{N_{\alpha,i}}{Q_i}}{\Sigma_i^N Q_i} = \frac{N_{\alpha,\text{tot}} \epsilon e}{\eta W \frac{\lambda^2}{2} Q_{\text{tot}}} \tag{5.3}$$

which can be intuitively understood as the resonance strength of the "sum" or "combination" of all runs. Formally, it is the average weighted over the charge. However, since the targets degrade we cannot make the assumption that leads to Eq. 5.3.

One possible solution would be to consider different stopping powers for each experimental run. To account for target degradation one would effectively increase the value of ϵ, thus increasing $N_\alpha \epsilon$. This would have the same effect as having a higher "real" N_α that was not observed because the target was degraded. However, even in the simplest case, N_α is obtained as the number of counts in the ROI on-resonance minus the natural background, normalised in time. Since the signal from the reaction is extremely weak, it is possible for the value of N_α to be negative due to statistical fluctuations and it does in fact happen in some experimental runs. If we increase the value of ϵ and N_α is negative, the value of $N_\alpha \epsilon$ will decrease, not increase. This would have the effect of reducing the number of counts in degraded targets, which is not physical. One could in principle discard the experimental runs that result in a negative N_α, but this would clearly bias the result towards higher values of $\omega\gamma$ in a way that is difficult to assess quantitatively.

Instead, we can proceed as follows. First, we (safely [1]) assume that the stopping power of different oxygen isotopes ϵ_x is the same. With this assumption, the

stopping power can be written as

$$\begin{aligned}\epsilon &= \frac{m_{17}}{m_\mathrm{p}+m_{17}}\left(\epsilon_{17}+\frac{n_{18}}{n_{17}}\epsilon_{18}+\frac{n_{16}}{n_{17}}\epsilon_{16}+\frac{n_\mathrm{Ta}}{n_{17}}\epsilon_\mathrm{Ta}\right)\\ &\simeq \nu\left[\epsilon_{17}\left(\frac{n_{17}}{n_{17}}+\frac{n_{18}}{n_{17}}+\frac{n_{16}}{n_{17}}\right)+\frac{n_\mathrm{Ta}}{n_\mathrm{O}}+\frac{n_\mathrm{O}}{n_{17}}\epsilon_\mathrm{Ta}\right]=\nu\left(\frac{\epsilon_{17}}{A_{17}}+S\frac{\epsilon_\mathrm{Ta}}{A_{17}}\right)\\ &= \frac{\nu}{A_{17}}(\epsilon_{17}+S\,\epsilon_\mathrm{Ta}) \quad (5.4)\end{aligned}$$

where $\nu = \dfrac{m_{17}}{m_\mathrm{p}+m_{17}}$, n_x is the number of nuclei of species x in the target. $S = \frac{n_\mathrm{Ta}}{n_\mathrm{O}}$ is the stoichiometry and $A_{17} = \frac{n_{17}}{n_\mathrm{O}}$ is the isotopic abundance of ^{17}O. Eq. 5.4 allows us to rewrite the resonance strength in Eq. 4.2 as

$$\omega\gamma = \frac{N_\alpha \dfrac{\nu}{A_{17}} e}{\eta W \frac{\lambda^2}{2} Q} = \frac{N_\alpha}{QA_{17}}\left[\frac{\nu e(\epsilon_{17}+S\epsilon_\mathrm{Ta})}{\eta W \frac{\lambda^2}{2}}\right] = \frac{N_\alpha}{QA_{17}}C \quad (5.5)$$

where C is the expression in the square parentheses. If there was no degradation, C could be considered constant for the three beamtimes. To account for target degradation, we introduce an additional degradation coefficient D between 0 and 1, where 0 represents a fresh target and 1 is a target with no ^{17}O left. Thus Eq. 5.5 becomes

$$\omega\gamma = \frac{N_\alpha}{QA_{17}(1-D)}C \quad (5.6)$$

D parametrises all sources of degradation in the target. Therefore, we are *not* assuming that the stoichiometry does not change over time. Rather, S in Eq. 5.5 can be thought of as the stoichiometry for a fresh target. All the effects of S or A_{17} changing - or any other phenomenon affecting the yield - are absorbed by D. In turn, the coefficient D is obtained from the empirical fit presented in section 4.5. We can now introduce an effective charge parameter k

$$k = QA_{17}(1-D) \quad (5.7)$$

this effective charge allows us to write the best resonance strength as the weighted

average over the effective charge k as opposed to the charge Q. Namely

$$\omega\gamma_{\text{best}} = \frac{\Sigma_i^N (\omega\gamma)_i k_i}{\Sigma_i^N k_i} = C\frac{N_{\alpha,\text{tot}}}{k_{\text{tot}}} \tag{5.8}$$

Note how by employing the effective charge we no longer have to deal with the issue of the statistical fluctuations of the single runs. Even if $N_{\alpha,i}$ is negative for a given run, as long as $N_{\alpha,\text{tot}}$ is positive we are able to correctly account for target degradation and different target isotopic enrichments through the effective charge. If $N_{\alpha,\text{tot}}$ is negative, we cannot claim a resonance (or an open reaction channel) exists in the first place.

5.2.3 Testing the resonance strength estimator

I tested the estimator of the $\omega\gamma$ value obtained in Eq. 5.8 in order to prove its reliability using Monte Carlo simulated data with realistic parameters. Specifically, I randomly generated the number of counts in the signal ROI for a large number of sets of ten runs each. Each run had random (but realistic) values for the current, target degradation, isotopic enrichment, and runtime. In particular, note the signal rate $R = 11$ counts/C and the background rate $B = 73$ counts/h. For each run, the number of events in the signal ROI was obtained as

$$N_{\text{events}} = N_{\text{nat.bkg}} + N_\alpha = P(Bt) + P(RQA_{17}(1-D)) \tag{5.9}$$

where B is the background rate (counts/h), t is the runtime, $R = \frac{N_\alpha}{k}$ is the signal rate (counts/C), Q is the charge deposited, A_{17} is the ^{17}O isotopic abundance and D is the degradation coefficient that appears in Eq. 5.7. P(x) is either equal to x, or a Poissonian random distribution with mean x.

First, I assumed P(x)=x and verified that the signal rate R obtained from the simulated data via Eq. 5.8 was the starting signal rate. Note that for these simulated data, the constant C that appears in Eq. 5.8 is arbitrary, and was set to one. The second step was to introduce statistical fluctuations by taking P(x) to be a Poissonian distribution. I also added a 3% Gaussian uncertainty on the real charge and a 1.3% Gaussian uncertainty on the real background rate to mimic the actual uncertainties in the experiment. I assumed no uncertainties in

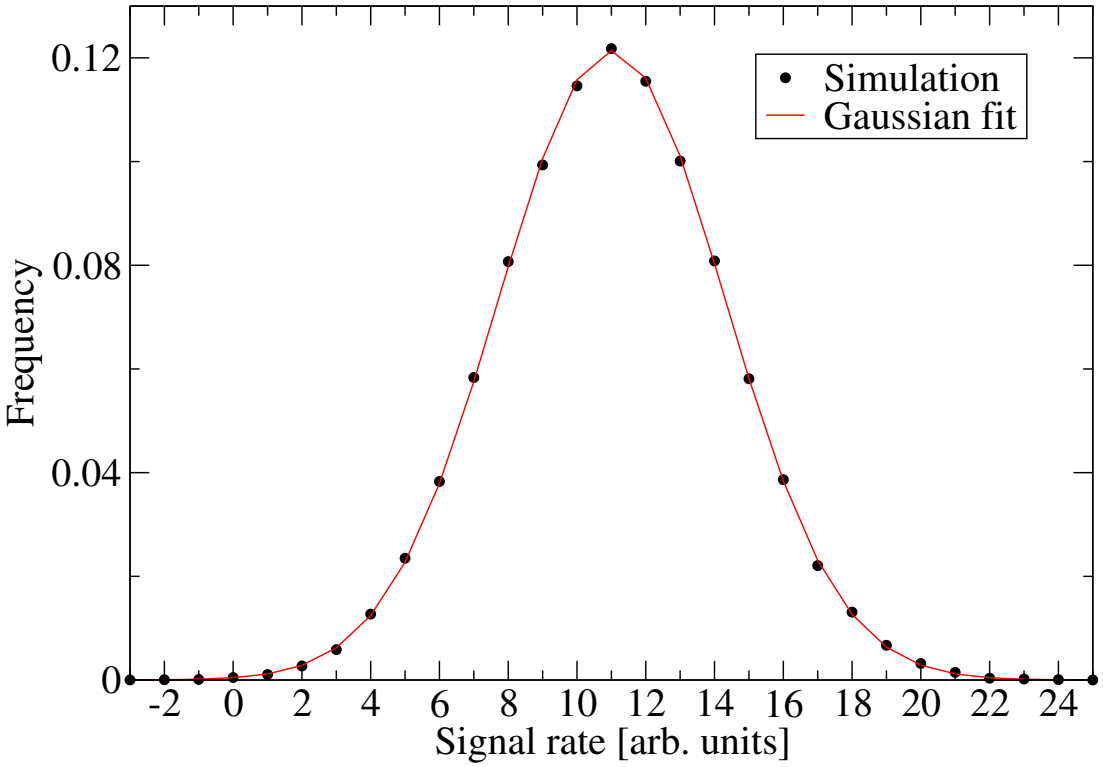

Figure 5.3 *Signal rate (black dots) obtained using Eq. 5.8 on simulated data. The maximum of the Gaussian curve coincides with the signal rate used to generate the data, proving that the estimator used is unbiased. See text for details.*

t, A and D. Fig. 5.3 shows the best signal rate value of 100 000 sets of 10 runs each produced by the simulation, as calculated from Eq. 5.8. The distribution is clearly Gaussian and the estimator used appears to be unbiased [73, 74], since the maximum coincides with the starting signal rate of R. This result proves that the estimator obtained in this section is reliable. Eq. 5.8 will be used in the next sections of this chapter to extract the resonance strength from the experimental data.

5.2.4 Angular distribution

Aside from the number of detected alpha particles $N_{\alpha,\mathrm{tot}}$, the only missing component in Eq. 5.8 is the angular distribution coefficient W=W(θ) which enters the definition of the C coefficient. For the case of the E_p = 193 keV resonance (Section 5.1), we were able to employ the Legendre coefficients obtained from a fit to experimental data in ref. [29]. However, no such measurements exist for

the E_p = 70 keV resonance because of its weakness. In order to calculate the W coefficient, I used an R-matrix fit to the data of the ^{17}O(p,α)^{14}N reaction, previously shown in Fig. 2.1. The data comes solely from ref. [24], except for the E_p = 193 and 70 keV resonances which I added (not fitted) using the parameters shown in Table 5.2.

Table 5.2 *Parameters used to calculate the angular distribution of the E_p=70 and 193 keV resonances in $^{17}O(p,\alpha)^{14}N$. For the E_p=70 keV resonance, the alpha particle width Γ_α was taken from ref. [69], and the proton width Γ_p was taken from ref. [33]. For the E_p=193 keV resonance, the widths were taken from refs. [31, 75].*

E_p	J^π	Γ_p	Γ_α
70 keV	1-	22 neV	130 eV
193 keV	2-	4 meV	13.3 eV

After obtaining the final resonance strength values for these two resonances (Sections 5.1 and 5.2.8) I used the new proton widths to repeat the fit, but found no influence on the angular distributions, as expected. While the resonance strength does not directly influence the angular distribution of a given resonance, what could potentially change is the fractional contribution from different resonances with different angular distributions at a given beam energy. However, since both the E_p = 70 and 193 keV resonances are isolated, contributions from the tails of other resonances are negligible. See Fig.17

Fig. 5.4 shows the angular distributions obtained from the AZURE2 [76] R-matrix calculation at E_p = 70 and 193 keV, as well as the angular distribution proposed in ref. [29] based on experimental results at E_p = 193 keV. The angular distributions are almost isotropic in both cases. For the E_p = 193 keV resonance, the agreement between the fitted and experimental angular distributions is quite good. The purpose of this comparison is to test the reliability of an R-matrix calculation to extract angular distributions for this reaction and at these energies. Based on the agreement, we can conclude that the angular distribution at E_p = 70 keV should be reliable as well. I decided to assign a conservative uncertainty of 20% to the Legendre coefficients derived from the R-matrix fit to reflect the small discrepancy observed at E_p = 193 keV. However, since the distribution is essentially isotropic, this 20% uncertainty on the Legendre polynomials is completely negligible with respect to the other systematics (Table 5.7). Ultimately, the W=$W(\theta)$ coefficient will be computed from the AZURE2 R-matrix fit and the uncertainties will be neglected.

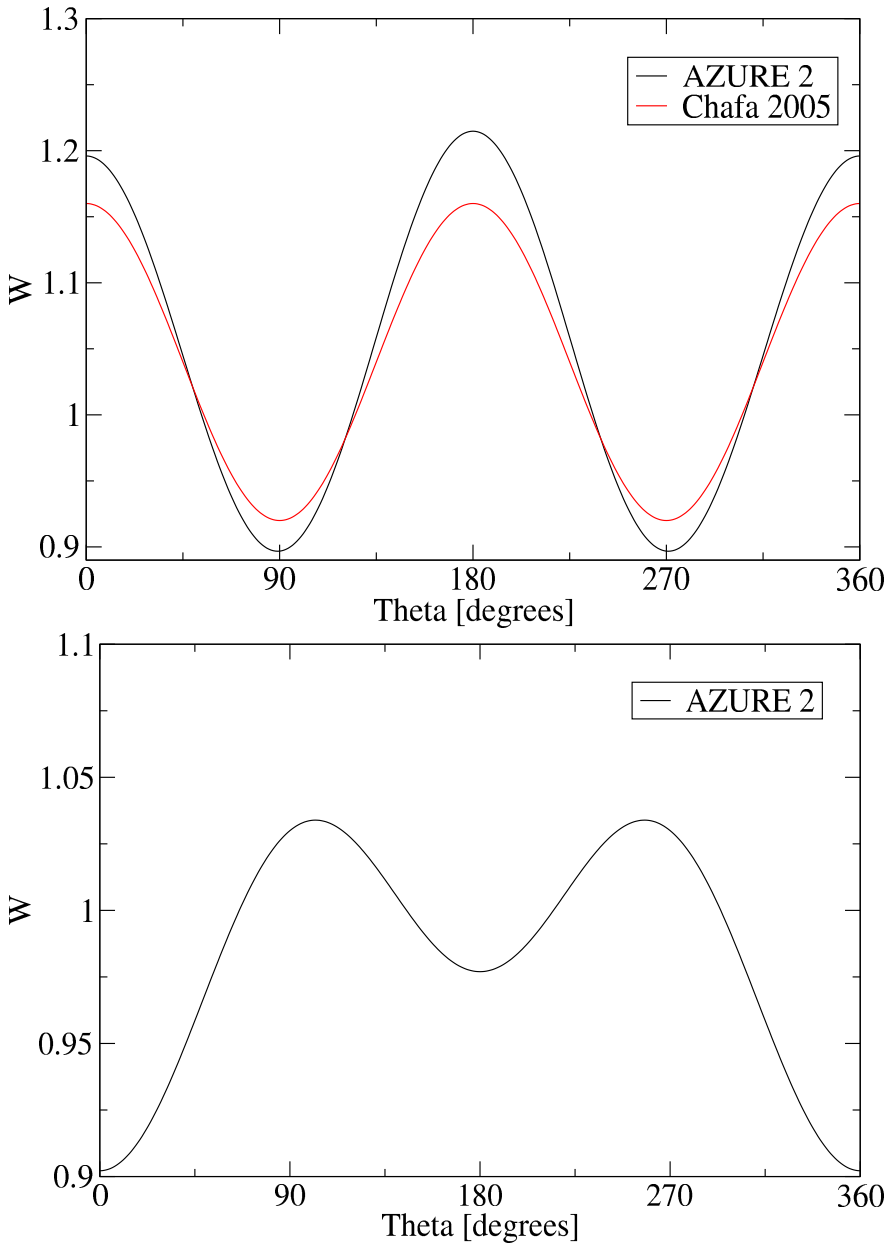

Figure 5.4 *The W=W(θ) angular distribution factor for the E_p = 193 keV resonance (top) and E_p = 70 keV resonance in $^{17}O(p,\alpha)^{14}N$ reaction (bottom). All quantities are in the CM frame. Chafa 2005 refers to the angular distribution fitted proposed in ref. [29]. See text for more details.*

5.2.5 Data taking procedure

In order to investigate the E_p=70 keV resonance, data were acquired in three different conditions. First, data were acquired "on-resonance" at E_p=71.5 keV, well within the expected thick-target yield plateau of the resonance. Second,

data were acquired "off-resonance" at E_p=65 keV in order to investigate potential sources of beam-induced background. Finally, "background" data were acquired without beam in order to assess the contribution of the natural background in the ROI of the resonance. Data were acquired during three experimental beamtimes. The first beamtime lasted from November to December 2013. The second beamtime took place from March to April 2014 in the same conditions of the first. This second beamtime ended with all aluminised Mylar foils breaking during a venting procedure. Foils were replaced using material from the same sheet from which the old broken foils had been cut. The third beamtime took place in April 2014, and while it was planned to measure the new foils at the end of the third beamtime, the foils broke again when venting before their thickness could be precisely determined. Therefore, we do not have a precise and reliable value for the expected energy of the alpha particles during the third beamtime. For this reason, it was not possible to identify a ROI in most detectors during the third beamtime, and I was only able to salvage data from Detector #5 and #7. Data from the other detectors failed most of the cross-checks presented in this chapter (e.g. section 5.2.6) and were ultimately discarded. From this point on, only detectors #5 and #7 will be considered for the third beamtime. Conservatively, data from the third beamtime were not employed to obtain the final resonance strength value. See Table 5.3 for information on the amount of data collected.

Table 5.3 *Data acquired for the E_p=70 keV in three experimental conditions: on resonance (E_p=71.5 keV), off-resonance (E_p=65 keV) and background (beam off). See text for details.*

	Background	Off-resonance	On-resonance
Beamtime	Accepted / Total	Accepted / Total	Accepted / Total
First	131 / 132 h	34 / 34 C	72 / 81 C
Second	86 / 87 h	23 / 41 C	34 / 56 C
Third	82 / 82 h	23 / 24 C	38 / 38 C

Data were acquired in list-mode during several experimental runs. Each run was divided into 20-minute long[1] "fragments" to assess the stability of the observables. The 20 minutes intervals were chosen as a compromise between having sufficient statistics in each fragment to pinpoint potential issues, and limiting loss of good data in case a fragment had to be discarded. For each detector four ROIs were considered (Fig. 5.5)

[1]Before dead time correction

1. **ROI 0** is the energy region below the signal ROI, and is expected to be dominated by electronic background. The counting rate in this ROI was used to study the electronic and scattering-induced backgrounds in the setup

2. **ROI 1** is the signal ROI, as defined in section 4.3

3. **ROI 2** is an energy region starting from the upper limit of ROI 1 with the same energy width as ROI 1. This ROI was used as a control sample.

4. **ROI B** is an energy region from 2.5 to 4.0 MeV, selected to include counts from the beam-induced background peak from ^{11}B(p,α)2α. The counting rate in this ROI was used to study the behaviour of the boron contamination in the target.

The energies of these ROIs are reported in Table 5.4. The rates (counts/h and counts/C) in these four regions of interest were studied across fragments acquired in the same experimental conditions (*e.g.* on-resonance) for a given beamtime. Fragments corresponding to known experimental issues (*e.g.* loss of beam on target) were discarded. Fragments with rates several (>5 sigma) standard deviations from the average values in any ROI were discarded. The remaining data were accepted for further analysis. See Table 5.3 for details.

Table 5.4 *Regions Of Interest (ROIs) considered for data acquired during the E_p=70 keV resonance investigation. Values are in keV. See text for details.*

Detector	ROI 0	ROI 1	ROI 2	ROI B
#1	< 150	160–240	250–330	2500-4500
#2	< 120	130–230	240–340	2500-4500
#3	< 170	180–290	300–410	2500-4500
#5	< 180	190–280	290–380	2500-4500
#7	< 180	190–270	280–360	2500-4500

5.2.6 Potential background sources

Because of the low signal to noise ratio, an in-depth study of the potential sources of background in the signal ROI was required. As an example, Fig. 5.5 shows the overlap between the time-normalised spectra acquired for Detector #1 during

the first beamtime in the three experimental conditions: on-resonance (E_p = 71.5 keV), off-resonance (E_p = 65 keV) and background (beam off). From the excellent agreement of the natural background spectrum with the other two, it is apparent that the primary source of events in the signal ROI is the natural background. The only features of note are the two peaks from ^{6}Li(p,α)^{3}He around 1-2 MeV and the ^{11}B(p,α)2α wide peak inside ROI B. None of these three peaks are close to the signal ROI (∼200 keV), but charged particle peaks may have low-energy tails due to straggling. These tails could affect the number of counts in the signal ROI.

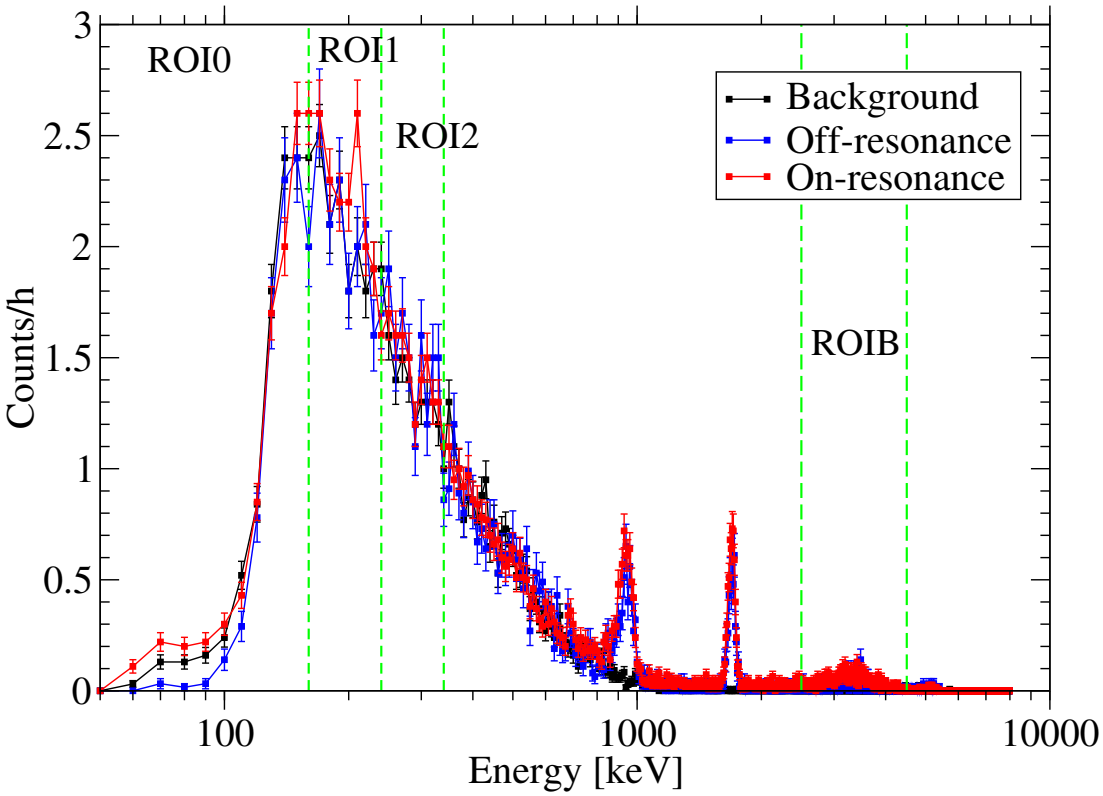

Figure 5.5 *Overlap between the time-normalised spectra acquired on-resonance, (E_p = 71.5 keV), off-resonance (E_p = 65 keV) and during background runs (no beam). Note the logarithmic scale on the energy axis. The main source of events appears to be the natural background. Data from Detector #1 during the first beamtime are shown, other detectors and beamtimes have similar behaviours. Uncertainties shown are statistical only. See text for details on observed peaks.*

It is worth noting explicitly that since there is experimental evidence of ^{11}B contamination it is safe to assume that ^{10}B is also present. Since ^{10}B(p,α)^{7}Be has Q-value = 1.146 MeV which is very close to that of ^{17}O(p,α)^{14}N (Q-

value=1.192 MeV) one could potentially expect some beam-induced background in the signal ROI due to ^{10}B contamination. However, since the mass of ^{7}Be is smaller than that of ^{14}N, the alpha emission energy is only E_α=710-750 keV depending on the angle of emission[2] for ^{10}B(p,α)^{7}Be, against E_α=1 MeV for the ^{17}O(p,α)^{14}N reaction. After the foils, the detected energy of the alpha particles from ^{10}B(p,α)^{7}Be should be less than $\sim$100 keV and should not affect the signal ROI.

Natural background can be measured and subtracted from the data on-resonance and off-resonance after normalisation in time. However, other sources of background such as reactions on target contaminants like Boron are not straightforward to subtract. In order to study the potential influence of beam-induced reactions on the signal ROI, I performed several correlation tests between the ROIs defined in Table 5.4. The aim of these correlation tests was to determine whether a variation in the counting rate (counts/C) in a ROI which is known to be affected by a given background source has any appreciable effect on the signal ROI. Specifically, I compared the Charge-Normalised Background-Subtracted (CNBS) number of counts in different ROIs. The CNBS rate is obtained as

$$\mathrm{CNBS} = (C_{beam} - C_{bkg}\frac{t_{\mathrm{beam}}}{t_{\mathrm{bkg}}})\frac{1}{Q} \tag{5.10}$$

where C_{beam} is the number of counts acquired in a given ROI with beam on target for a time t_{beam} and collected charge Q, while C_{bkg} are the number of natural background (beam off) counts acquired in the same ROI, in a time t_{bkg}. CNBS rates can be thought of as the beam-induced event rate.

Fig. 5.6 shows the correlation plots for ROI 0 vs. ROI 1. Recall ROI 0 extends down to the ADC threshold and is potentially affected by electronic noise, while ROI 1 is the signal ROI. The two quantities plotted appear uncorrelated. In particular, note how for Detector #3 (Fig. 5.6 bottom) the CNBS rate in ROI 0 changes over five orders of magnitude, likely because of different electronic noise conditions during the experimental runs. However, the number of counts in ROI 1 remains in good agreement within the experimental uncertainties. This test was repeated for all working detectors and all beamtimes and results are consistent with those shown in Fig. 5.6. These results show that the signal ROI chosen is neither significantly affected by electronic noise issues nor by beam-induced

[2]The precise angle of emission is not trivial to compute as the distribution of the Boron in the target and/or backing is not known.

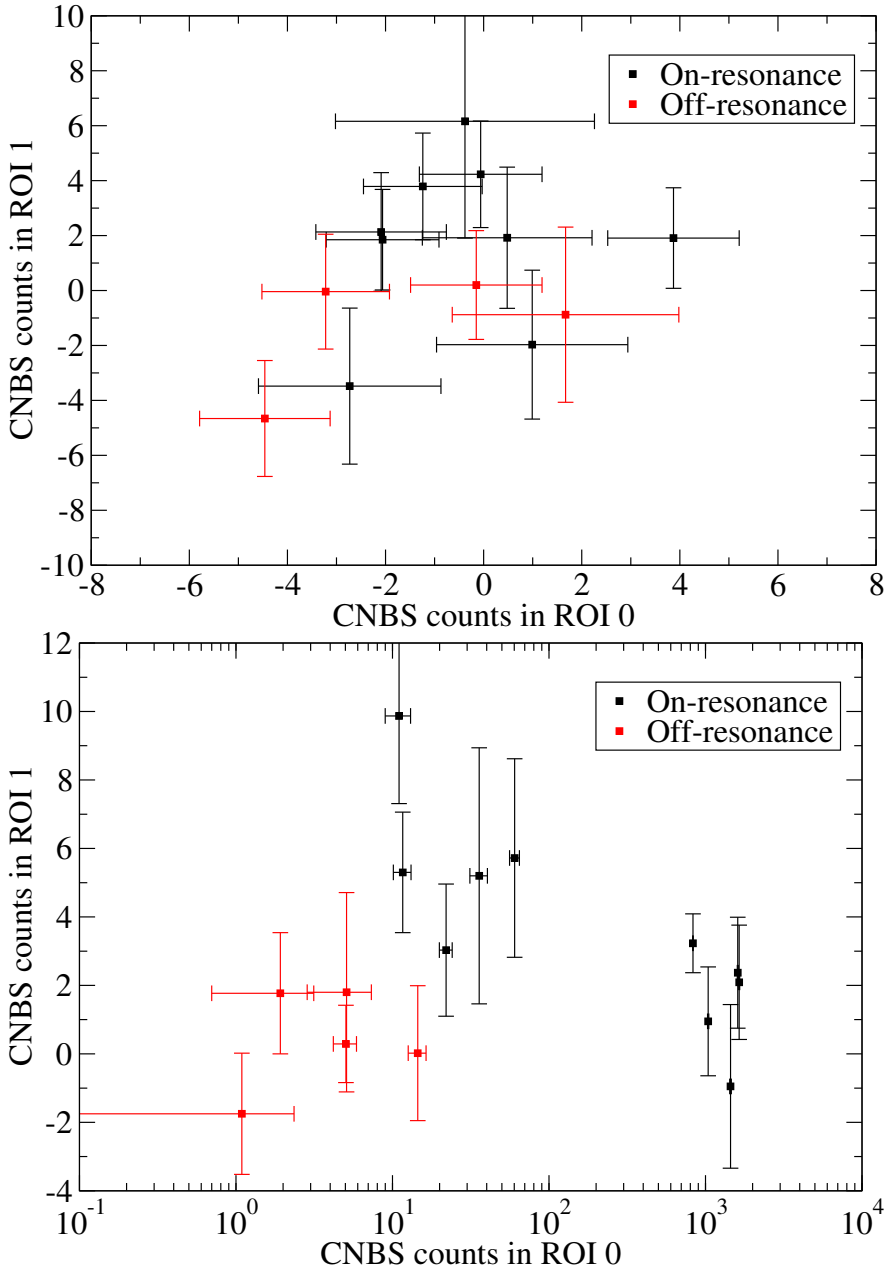

Figure 5.6 *Charge-Normalised Background-Subtracted (CNBS) counts in ROI 1 vs ROI 0 for (top) Detector #1 and (bottom) Detector #3 during the first beamtime. Each point corresponds to one experimental run. Uncertainties shown are statistical only. No correlation can be observed between the CNBS rates in the two ROIs. Other detectors and beamtimes show similar behaviours.*

background.

Fig. 5.7 shows a similar correlation test performed between ROI B, which is set at the energy of the ^{11}B(p,α)2α alpha peak(s) (see Fig. 5.5) and the signal ROI.

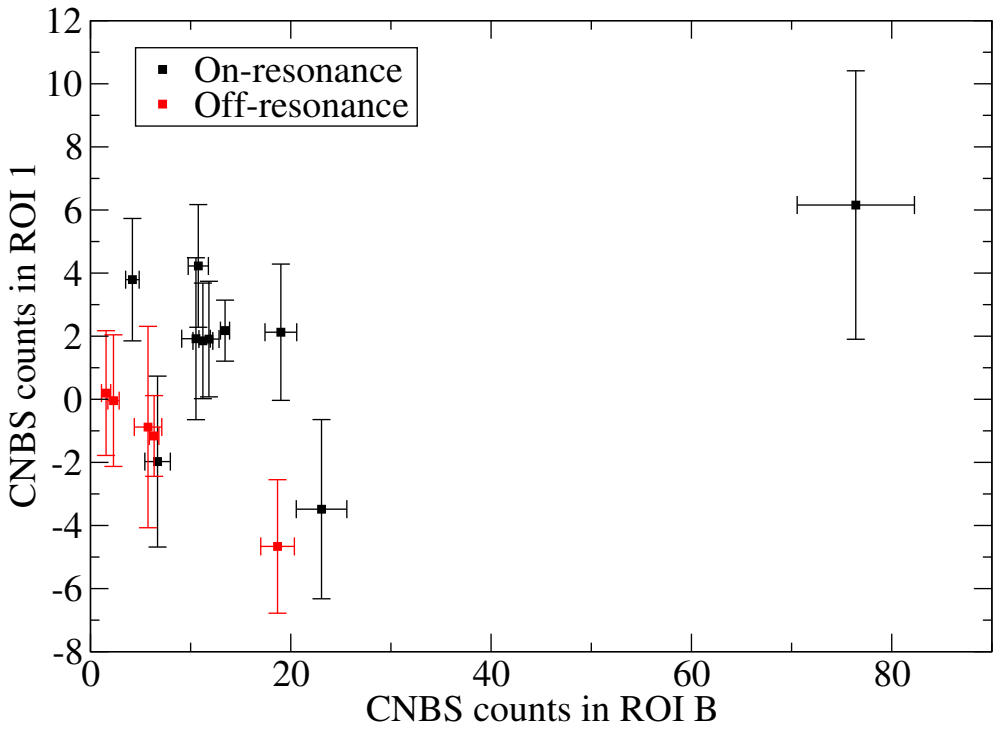

Figure 5.7 *Charge-Normalised Background-Subtracted (CNBS) counts in ROI 1 vs ROI B for Detector #1 during the first beamtime. Each point corresponds to one experimental run. Uncertainties shown are statistical only. No correlation can be observed between the CNBS rates in the two ROIs. Other detectors and beamtimes show similar behaviours.*

No obvious correlations can be observed between the two CNBS rates. Note the data point corresponding to higher boron content is still in good agreement with the other data points within statistical uncertainties. There is no evidence of events due to beam-induced reactions on boron in the signal ROI.

Another potential source of background shown in Fig. 5.5 is the reaction ^{6}Li(p,α)^{3}He. The lithium contamination is primarily due to the undesired after-effects of an unsuccessful test performed to determine the amount of beam lost on the target holder. This test was carried out with a lithium target deposited on a tantalum backing. The beam sputtered part of the lithium on the inner edge of the holder, contaminating the next oxygen target mounted. After cleaning the target holder this lithium contamination was eliminated. For this reason, only a few experimental runs acquired during the first beamtime show a significant lithium content. The CNBS ROI 1 rate of these runs is in excellent agreement with that calculated from runs without lithium contamination. The two lithium-induced peaks are too high in energy to affect the signal ROI, as is also apparent

in Fig. 5.5. Therefore, I decided to include these lithium-contaminated runs in the final calculation of the resonance strength.
In conclusion, from these correlation tests we can conclude that the signal ROI is affected by neither electronic noise nor beam-induced background reactions on obvious contaminants (boron, lithium). The possibility of other, unknown sources of beam-induced background will still be conservatively considered in the rest of this analysis.

5.2.7 Further data quality checks

I performed a few more checks on the quality of the data acquired. The signal ROI on-resonance and off-resonance CNBS rates obtained detector by detector in ROI 1 for the first and the second beamtimes are shown in Fig. 5.8. The same data are also reported in Table 5.5 for comparison. These rates were obtained as the weighted average on the collected charge Q of all data acquired in a given beamtime with a given detector. The off-resonance CNBS rates are always either negative or in agreement with zero within one sigma. This implies once again that there is no evidence for beam-induced background in the region on interest. The on-resonance CNBS rates are consistently higher than the off-resonance ones, indicating the presence of a signal in ROI 1. The last datapoint on the right-hand side in Fig. 5.8 corresponds to the weighted average on the charge across all detectors. In other words, this is the value that one would use in Eq. 4.2 in order to calculate the resonance strength. Finally, note how the on-resonance value is both greater than zero and greater than the off-resonance rate outside of the uncertainties.

Table 5.5 *Charge-Normalised Background-Subtracted (CNBS) rates for the five working detectors and the two first beamtimes. Values are in counts/C. See text for details and Fig. 5.8 for a plot of these data.*

	#1	#2	#3	#5	#7	Sum
1st beamtime						
On-res.	2.2±1.0	2.5±1.0	3.2±0.9	1.3±0.8	1.0±0.9	10.2±2.0
Off-res.	-1.2±1.3	-0.1±1.3	0.3±1.2	-1.0±1.1	-1.5±1.1	-3.6±2.7
2nd beamtime						
On-res.	1.9±1.4	3.2±1.5	1.0±1.3	3.3±1.1	5.2±1.1	14.5±2.9
Off-res.	0.6±1.9	1.8±2.0	0.3±1.7	0.3±1.4	0.3±1.4	3.3±3.8

Another interesting test consisted of comparing the CNBS rate in the low energy

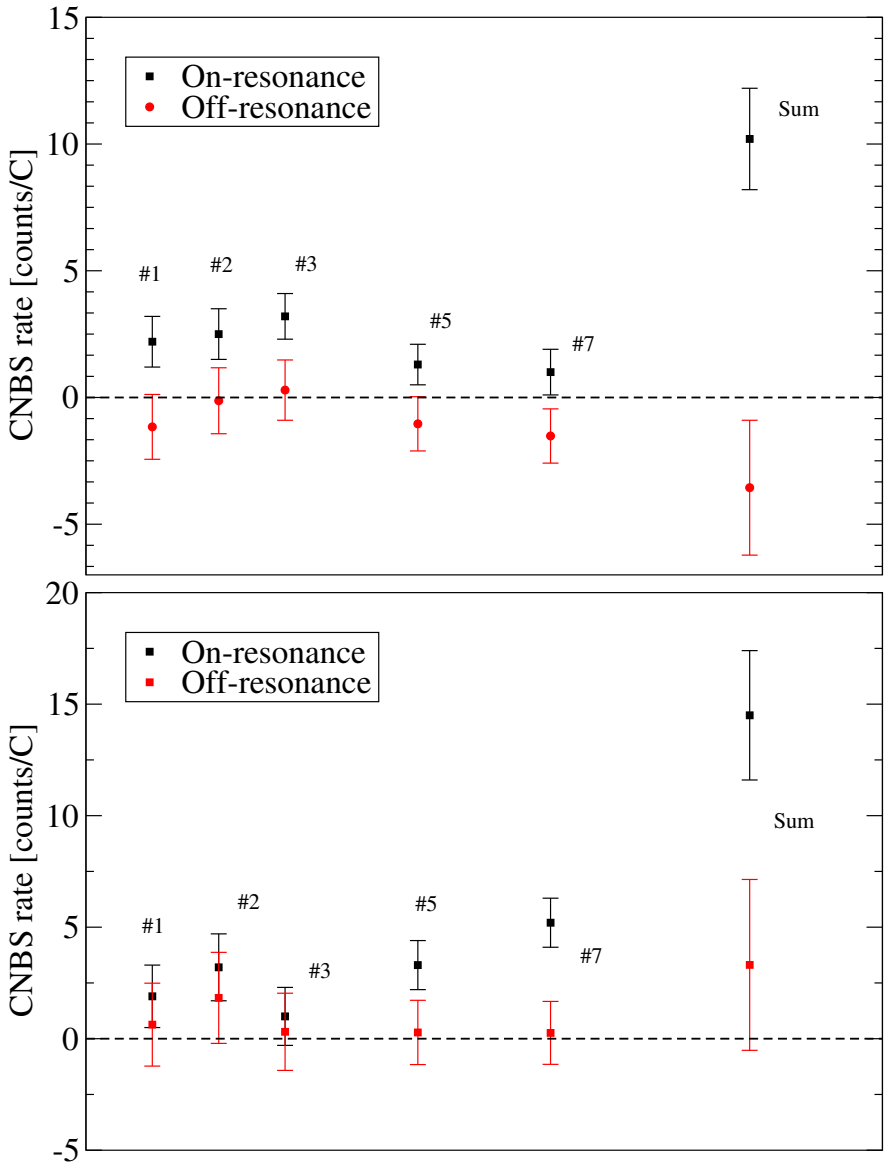

Figure 5.8 *Weighted average on the charge of the Charge-Normalised Background-Subtracted (CNBS) rates for the five working detectors in ROI 1 during the first (top) and second (bottom) beamtime. The detectors shown are #1,2,3,5,7 in this order. The last data point on the right corresponds the CNBS rate obtained from the sum of the counts observed in all detectors. Note the CNBS off-resonance rates (in red) are in agreement with zero, indicating a lack of beam-induced background. See text and Table 5.5 for details.*

half and the high energy half of the signal ROI. The signal ROI was split in two energy regions of the same energy width and the CNBS rate of the left-hand (low energy) region was compared with that of the right-hand (high energy) region. If the signal ROI had not been selected correctly, one could expect different rates in the two halves of the ROI. For instance, if the ROI was too low in energy,

one would expect the low energy half having a lower counting rate than the high energy half. Fig. 5.9 shows the result of this test for the first two beamtimes. The agreement is excellent for the first beamtime, where only detector #7 seems to show some minor issues. For the second beamtime, the two halves of the signal ROI are in good agreement for two detectors (#1 and #5) out of five, and still in rough agreement for the other three. If we assume that the signal is perfectly symmetric in the ROI and that the underlying statistics are Gaussian[3], then we would expect roughly three data points out of five to be in agreement. Neither of these two assumptions is necessarily true, therefore, we can consider the agreement shown for the second beamtime to be acceptable. While this test may not be perfectly conclusive, it is ultimately an important piece of evidence of the quality of the data and a further confirmation of the reliability of the signal ROI.

5.2.8 Resonance strength

Based on the theoretical framework presented in the section 5.2.2 we can use the data accepted after the tests in sections 5.2.5, 5.2.6, and 5.2.7 to calculate the resonance strength. The only missing piece of information in Eq. 5.8 is $N_{\alpha,\mathrm{tot}}$, the number of alpha particles detected during the on-resonance run. As explained in section 5.1, a fit of the alpha peak is unreliable due to the presence of the low energy background and the overlap with the tail of the alpha peak as shown in Fig. 5.1. These issues would be compounded by the lower energy of the alpha peak for the resonance at $E_p = 70$ keV as compared to the resonance at $E_p = 193$ keV.

Just like in section 5.1 as a first approach we will simply integrate the number of counts in the ROI and subtract the time-normalised natural background from the on-resonance. A +2% asymmetric statistical uncertainty will account for the tails of the peak. In order to account for potential sources of beam-induced background, we will repeat this operation for the off-resonance as well. We could then in principle obtain the number of alpha particles $N_{\alpha,\mathrm{tot}}$ as

$$N_{\alpha,\mathrm{tot}} = (C_{\mathrm{on}} - C_{\mathrm{bkg}}\frac{t_{\mathrm{on}}}{t_{\mathrm{bkg}}}) - (C_{\mathrm{off}} - C_{\mathrm{bkg}}\frac{t_{\mathrm{off}}}{t_{\mathrm{bkg}}})\frac{Q_{\mathrm{on}}}{Q_{\mathrm{off}}} \tag{5.11}$$

where C is the number of counts observed in the signal ROI, t is the live time, Q is

[3]This assumption is not completely trivial, and is further explored in section 5.2.8

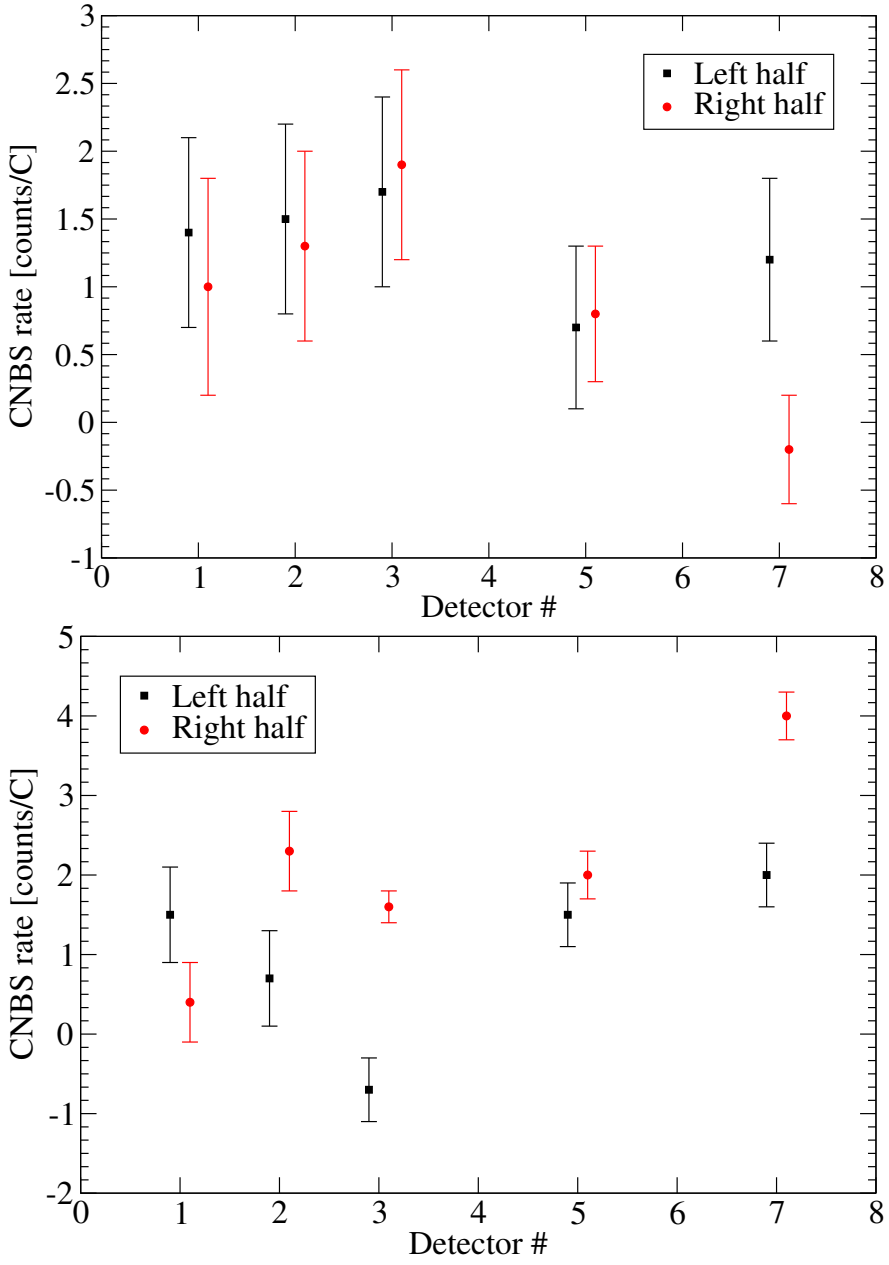

Figure 5.9 *Charge-Normalised Background-Subtracted (CNBS) rates for the left half (low energies, black) and the right half (high energies, red) of the signal ROI for the first beamtime (top) and second beamtime (bottom). The agreement between the CNBS rates in the two halves is excellent in the first beamtime, and acceptable for the second beamtime. Uncertainties shown are statistical only. See text for details.*

the charge acquired, and the three subscripts refer to the quantities observed on-resonance, off-resonance and during background runs. Table 5.6 shows a summary of the data for the three beamtimes. Note once more that the third beamtime

was affected by several experimental issues, and that only two detectors (#5 and #7) passed the stringent tests detailed in sections 5.2.5, 5.2.6, and 5.2.7.

Table 5.6 *Summary of the data acquired on-resonance (E_p = 71.5 keV), off-resonance (E_p = 65 keV) and during background runs (beam off). Shown are the integral of the counts in the signal ROI for the working detectors as well as the sum of those counts, the live time t, the charge Q, the effective charge k and the constant C (see Eq. 5.8). 1st, 2nd and 3rd refer to the three beamtimes.*

	Background			**Off-resonance**			**On-resonance**			
	1st	2nd	3rd	1st	2nd	3rd	1st	2nd	3rd	
#1	2458	1396		1140	682		2460	1203		counts
#2	2501	1659		1194	829		2522	1462		counts
#3	1874	1218		907	591		1986	1028		counts
#5	1341	847	1064	609	412	921	1350	801	1159	counts
#7	1407	810	866	625	394	712	1392	832	909	counts
Sum	9581	5930	1930	4475	2908	1633	9710	5326	2068	counts
t	131	86	82	63	41	62	123	70	82	h
Q				32	17	23	70	33	38	C
k							54	24	28	C
C							0.6	0.6	1.6	neV×C

An issue arises in using Eq. 5.11 to get $N_{\alpha,\text{tot}}$. The quantity $(C_{\text{off}} - C_{\text{bkg}}\frac{t_{\text{off}}}{t_{\text{bkg}}})\frac{1}{Q_{\text{off}}}$, which corresponds to the CNBS off-resonance rate, is negative for the first beamtime as previously shown in Table 5.5. Note the rate is not quite in agreement with zero in Fig. 5.8. In that figure the background of the first and second beamtime were being considered separately. If one considers a single background for the first and second beamtime, which is physically justified since they were taken in the same conditions, the CNBS off-resonance rate is in agreement with zero. From a statistical point of view, this negative result is simply an artefact of taking the difference between two large and similar numbers. However, one could argue that from a physical point of view the CNBS rate cannot be negative, regardless of its uncertainty. Specifically, if one were to use Eq. 5.11 to obtain $N_{\alpha,\text{tot}}$ one would *increase* the number of alpha particles detected after correcting for the off-resonance. This is not physically meaningful and therefore, Eq. 5.11 cannot be used as is. Ultimately since the off-resonance rate for both the first and the second beamtime are in agreement with zero and there is no evidence of beam-induced background, one could simply conclude that the off-resonance

rate is zero and therefore

$$N_{\alpha,\mathrm{tot}} = C_{\mathrm{on}} - C_{\mathrm{bkg}} \frac{t_{\mathrm{on}}}{t_{\mathrm{bkg}}} \tag{5.12}$$

which is an even simpler version of Eq. 5.11. If one uses Eq. 5.12 together with Eq. 5.8 and the values in Table 5.6, one can calculate the resonance strength for each beamtime separately, including separate backgrounds. This results in

- First beamtime: $\omega\gamma = 9.2 \pm 1.4_{\mathrm{stat}} \pm 0.8_{\mathrm{syst}}$ neV
- Second beamtime: $\omega\gamma = 10.4 \pm 0.8_{\mathrm{stat}} \pm 0.6_{\mathrm{syst}}$ neV
- Third beamtime: $\omega\gamma = 8.5 \pm 3.8_{\mathrm{stat}} \pm 0.6_{\mathrm{syst}}$ neV

which are in excellent agreement with each other. In spite of the agreement between the third beamtime and the other two, I conservatively decided to discard data from this third beamtime because of the numerous experimental issues it was affected by. From this point on, only data from the first two beamtimes will be considered in the analysis. The natural next step is to combine[4] the first and second beamtime data to arrive at a resonance strength value $\omega\gamma = 9.7 \pm 1.3_{\mathrm{stat}} \pm 0.7_{\mathrm{syst}}$ neV. The systematic uncertainty budget is reported later in Table 5.7. Fig. 5.10 shows a composite spectrum obtained following the analysis approach just described. Specifically, each bin of the histogram contains the CNBS rate as defined in Eq. 5.12. The shaded region indicates the signal ROI. The on-resonance raw spectrum shows a clear counting excess at energies corresponding to this ROI in the on-resonance, while the off-resonance and the natural background spectra are in excellent agreement. The issue with proceeding in this way is that we are not introducing any uncertainty due to the possibility of a small beam-induced background.

An alternative, more sophisticated way to proceed is to employ the Maximum Likelihood (ML) technique [73, 74], and specifically an analysis method based on the one proposed in ref. [77], section 5.1. A description of this technique is given in Appendix B, and results are presented in Table B.1. Using the N_α value obtained from the ML method in Eq. 5.8 we obtain $\omega\gamma = 10.8 \pm 1.5_{\mathrm{stat}} \pm 0.8_{\mathrm{syst}}$. The systematic uncertainty budget is the same as for the subtraction method (Table

[4]Repeat the analysis without making distinctions between data taken in different beamtimes, *not* average together

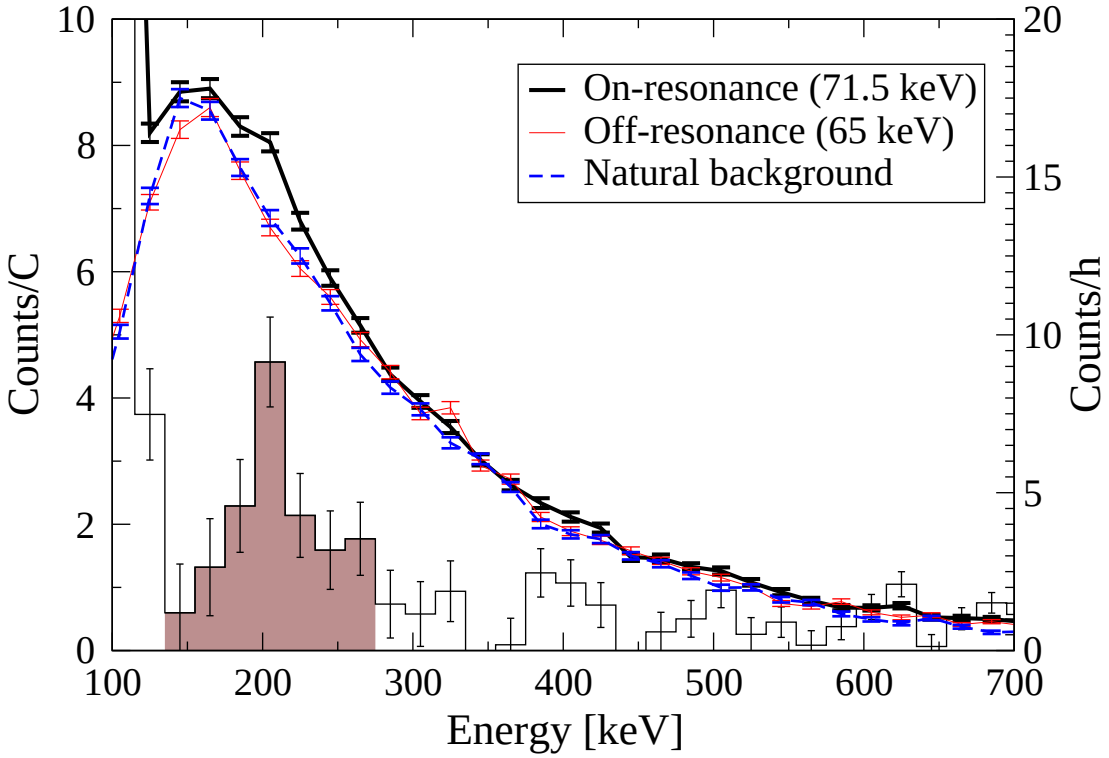

Figure 5.10 *Overlay of on-resonance ($E_{\rm p}$ = 71.5 keV), off-resonance ($E_{\rm p}$ = = 65 keV) and natural background spectra in counts/h (lines are to guide to eye), and the histogram obtained from the bin-by-bin subtraction of the natural background spectrum from the on-resonance spectrum in counts/C.*

5.7). The $\omega\gamma$ value obtained from the subtraction method and the Maximum Likelihood method are consistent, as one would expect. Since the Maximum Likelihood method is more refined and takes into account the possibility of beam-induced background (see Appendix B), I decided to adopt the $\omega\gamma$ calculated with the Maximum Likelihood method as the experimental value of the $\omega\gamma$ for the $E_{\rm p} = 70$ keV resonance.

Before the $\omega\gamma$ can be used to calculate the reaction rate, one has to correct it for electron screening (section 2.5). In this case the screenening correction factor $f_e = 1.15$, and we obtain a bare value of $\omega\gamma_{\rm bare} = 10.0 \pm 1.4_{\rm stat} \pm 0.7_{\rm syst}$. Equivalently, one can express the result in terms of the proton width Γ_p of the $E_x = 5672$ keV in ^{18}F associated with this resonance. Employing the definition of γ (section 2.2), under the assumption $\Gamma_{\rm tot} \simeq \Gamma_\alpha = 130 \pm 5$ eV [69] we find $\Gamma_p = 35 \pm 5_{\rm stat} \pm 3_{\rm syst}$ neV (bare).

Table 5.7 *Uncertainty budget for the $\omega\gamma$ of the E_p=70 keV resonance in $^{17}O(p,\alpha)^{14}N$. The statistical uncertainty refers to the uncertainty derived from the Maximum Likelihood method (Appendix B). The other sources of error are systematic.*

Source	Percent uncertainty
Statistical	±14.2%
Charge	±2.0%
Tail asymmetry	+2.0%
Stopping power	±4.0%
Efficiency	±5.5%

5.2.9 Comparison with previous measurements

Because of the complex history of the measurements of the strength of the E_p = 70 keV resonance, carrying out a comparison between previous measurements and the value obtained in this work is not straightforward. The value obtained here, $\omega\gamma_{bare} = 10.0 \pm 1.4_{stat} \pm 0.7_{syst}$, is approximately a factor of two higher than previous direct measurements, and almost three times higher than previous indirect measurements (see Table 3.1). However, a comparison with indirect measurements is not entirely fair since the method employed is radically different and one could reasonably expect the systematics to be different as well. It would be more interesting to compare the value obtained in this work with the three strengths obtained from the analyses of Blackmon's data [33, 36, 37]. However, no details are available for the second reanalysis [37], and only limited information is present in ref. [36]. Therefore, the only meaningful comparison can be made with the value in the original analysis in ref. [33]. For this analysis, it is known that the fits were carried out assuming Gaussian statistics (i.e. the chi-square technique) which is not appropriate given the low counting rates [36]. Considering this statistical issue, it is not unreasonable to expect the result to be somewhat in disagreement with the value of this work. Compared with previous works, the stringent definition of the signal ROI employed in this work paired with the significant background reduction afforded by the underground environment and the statistical tools employed to extract the resonance strength make the $\omega\gamma$ value obtained in this section arguably the most accurate to date.

5.3 Reaction rate

I computed the reaction rate employing the RatesMC code introduced in section 2.6.3 with same input file used in ref. [78], which was kindly provided by the authors of that work. I only changed the value of the proton width of the $E_x = 5672$ keV state in ^{19}F associated with the $E_\mathrm{p} = 70$ keV resonance in ^{17}O(p,α)^{14}N, which was set to $\Gamma_p = 35 \pm 6$ neV. This is the value derived in our work, where the uncertainty is the combination of the statistical and systematic uncertainties since RatesMC can only accept a single uncertainty value per parameter. Results are shown in Fig. 5.11.

I should note explicitly that in ref. [78] the difference between the results presented in Iliadis 2010 [79] and those in Buckner 2015 [78] is partly ascribed to an updated estimate of an interference between a sub-threshold resonance at $E_\mathrm{p} \simeq -2$ keV and the $E_\mathrm{p} = 70$ keV resonance. However, as also stated in ref. [39], I found no evidence of an appreciable influence of this sub-threshold resonance on the reaction rate. Specifically, removing the sub-threshold resonance or increasing its present upper limit on Γ_p by a factor of 10 had no effect on the reaction rate. Instead, I found that the difference between the results presented in refs. [79] and [78] is due to an updated value of the proton separation threshold of ^{19}F following the recommendation of ref. [80]. The input file used for the calculation of the reaction rate in this thesis work uses this updated proton threshold value.

The result of this work, between 0.01 and 0.1 GK, temperatures relevant for RGB/AGB stars, the difference is around a factor of 2. The difference is solely due to the updated value of the proton width associated with the $E_\mathrm{p} = 70$ keV resonance obtained in this work. This significant increase has several profound implications for the expected abundances of ^{17}O in a number of stellar sites, as discussed in greater detail in chapter 7.

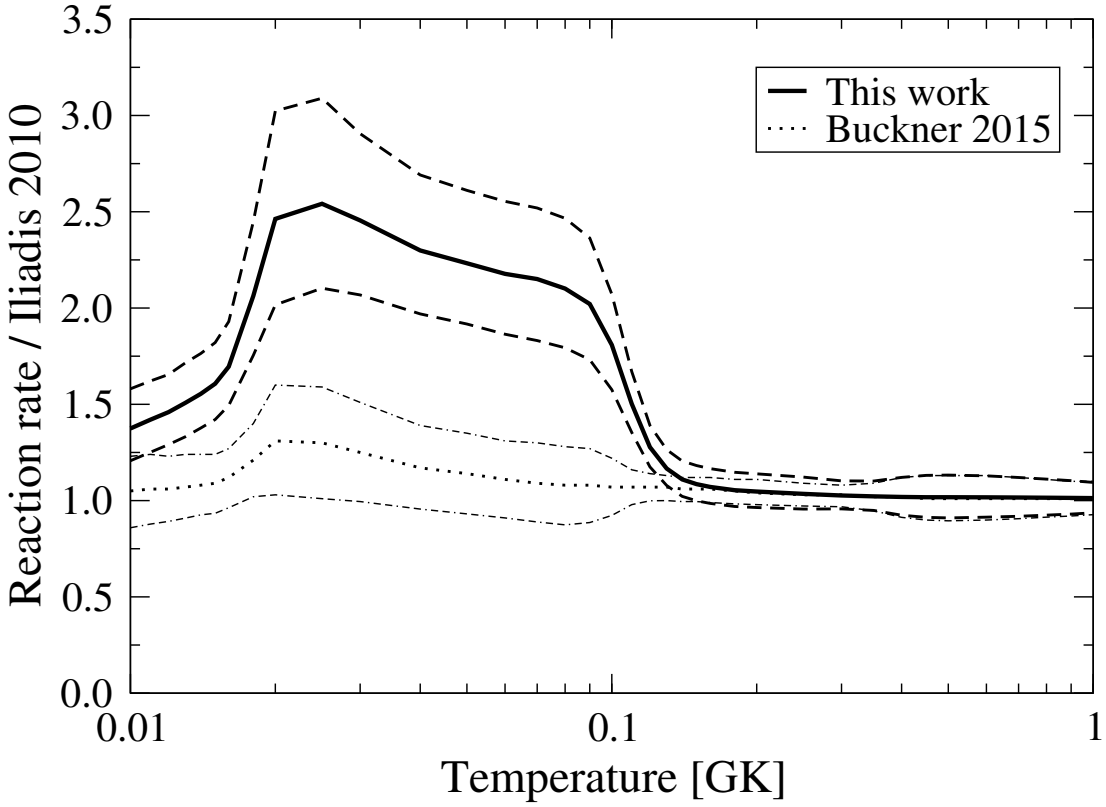

Figure 5.11 *The reaction rate of the $^{17}O(p,\alpha)^{14}N$ reaction, compared with that in Iliadis 2010 (STARLIB) [79]. The thick solid line indicates the reaction rate derived in this work, with the dashed lines indicating the upper and lower limits. The dotted line shows the rate ratio obtained in ref. [78] with the dashed-dotted lines showing the upper lower limits of that value.*

Chapter 6

The ^{18}O(p,α)^{15}N campaign

The main objective of this experimental campaign was the measurement of the excitation function of the ^{18}O(p,α)^{15}N reaction at energies accessible by the LUNA-400kV accelerator ($E_{\rm p} \sim 40 - 400$ keV). Section 6.1 describes the data taking procedure and the steps taken to extract a yield from the experimental spectra. After extracting a yield, three resonances were analysed employing the thick-target yield approximation (section 2.2) and the resonance strength parameters obtained are presented in section 6.1.4. The experimental yield was converted to a cross-section (section 6.1.5) and used in an R-matrix fit (section 6.2.2) together with data from previous investigations (chapter 3). The results of this fit, presented in section 6.2.2, were used to compute an updated astrophysical rate for the ^{18}O(p,α)^{15}N reaction, given in section 6.3.

6.1 Data analysis

6.1.1 Data taking procedure

Data were acquired at the energies of the $E_{\rm p}$=151 keV resonance in ^{18}O(p,α)^{15}N during the commissioning of the experimental setup (Chapter 4) and the measurement of the ^{17}O(p,α)^{14}N reaction (Chapter 5), in a large variety of experimental conditions, including isotopic enrichment, beam intensity and presence of the collimators. The strength of this resonance is given in section 4.6, and is in good agreement with previous investigations [51]. Data for the

^{18}O(p,α)^{15}N reaction at all other proton energies were acquired solely from targets from batch #6 (Section 4.5) and without collimators. Proton energies as high as $E_{\rm p}$=360 keV were reached. Measurements were performed using 5 μm aluminised Mylar foils to remove background due to elastic scattering (Section 4.3). In principle $E_{\rm p}$=360 keV is 40 keV lower than the maximum proton energy achievable by the LUNA-400kV accelerator, but TRIM [11] simulations suggested the foils used would not stop the scattered beam protons above $E_{\rm p}$=360 keV. Since no features of interest (*e.g.* resonances) were expected in the cross-section between $E_{\rm p}$=360 and 400 keV, data acquisition at higher beam energies was not attempted. At low beam energies, the limiting factor was the cross-section which as expected fell sharply because of the hindering effect of the Coulomb barrier. We were able to reach energies as low as $E_{\rm p}$=60 keV, with typical rates of the order of 0.4 counts/C/detector (0.1 counts/h/detector), before the experimental campaign was stopped due to beam time constraints.

All data above $E_{\rm p}$ = 103 keV were acquired on 5 keV targets, while data below $E_{\rm p}$ = 103 keV were acquired on 15 keV thick targets. The thickness is given as the energy loss for 200 keV protons (see Section 4.5). The reason for this choice is that, while first measuring the $E_{\rm p}$ = 95 keV resonance, inconsistent results were observed in the yield employing 5 keV thick targets. At the time of the measurement, these inconsistencies were taken as a potential indication that the (unknown) width of the $E_{\rm p}$ = 95 keV resonance was larger than 5 keV, thus 15 keV thick targets were produced and used instead, resulting in reasonable yields (Fig. 6.2). A re-analysis of the data acquired on the 5 keV thick targets showed that the inconsistencies were due to high target degradation and poor statistics, and a trend consistent with a thick-target profile appeared once target degradation was accounted for. However, by then the experimental campaign had been completed and all data at beam energies below $E_{\rm p}$ = 103 keV were acquired on 15 keV thick targets. Using thicker targets increases the yield (more target nuclei), and "smears" out the cross-section as the reactions occur over a wider energy range. Both these effects will be addressed in Section 6.1.5.

6.1.2 Potential sources of background

Because of the higher alpha particle energies ($E_\alpha \simeq$ 2.2 MeV) as compared with the ^{17}O(p,α)^{14}N reaction study ($E_\alpha \simeq$ 200 keV), natural and beam-induced background were negligible at all but the lowest beam energies. Typical natural background rates in the ROI for the alpha particle peak of the ^{18}O(p,α)^{15}N

reaction were around 0.04 counts/h/detector, corresponding to a reasonable signal to background ratio even at the lowest beam energies (Fig. 6.1). For instance, at E_{p}=60 keV the signal to noise ratio was 5:2. The only source of beam-induced background were the low-energy tails of the broad alpha peak of the ^{11}B(p,α)2α reaction (Fig. 6.1 - bottom). These tails gave a small contribution with respect to the signal peak, which was always clearly distinguishable above the background down to E_{p}=65 keV.

I attempted to study, model and subtract the beam-induced background from ^{11}B(p,α)2α, but ultimately decided against it. The ^{11}B(p,α)2α reaction could in principle proceed either as a two-step process or a one-step process

- Two-step process: ^{11}B+p $\rightarrow$ α_0+^{8}Be $\rightarrow$ α_0 + 2α
- One-step process: ^{11}B+p $\rightarrow$ α + α + α

where the difference is in the way the Q-value=8.590 MeV is divided among the alpha particles in the final state. Experimental evidence [81] currently suggests the two-step mechanism is dominant [81], but the final shape of the alpha peak(s) is difficult to predict because it strongly depends on the interaction energy through the angular distributions [81]. Details are beyond the scope of this work, see instead the recent ref. [81] and references within. Also note that we do in fact observe the ^{11}B(p,α)2α reaction peak changing shapes at different beam energies. Modelling the small contribution of the ^{11}B(p,α)2α reaction in the ROI of the alpha peak of the ^{18}O(p,α)^{15}N would be non-trivial and would introduce model-dependent uncertainties in the final results that are difficult to quantify. Ultimately, I decided to neglect the beam-induced background from ^{11}B(p,α)2α; the uncertainty associated with this choice is negligible compared to the typical uncertainties of the experiment (*e.g.* stopping power and efficiency).

6.1.3 Obtaining the yield

In order to extract a number of detected counts from the experimental spectra, I wrote a program to carry out a simple integration in a ROI centred on the alpha peak. The ROI was typically centred approximately around E_{α}=2.2 MeV and had a fixed width of 0.5 MeV at all beam energies. The energy of the peak depends (weakly) on the beam energy and was adjusted automatically by the

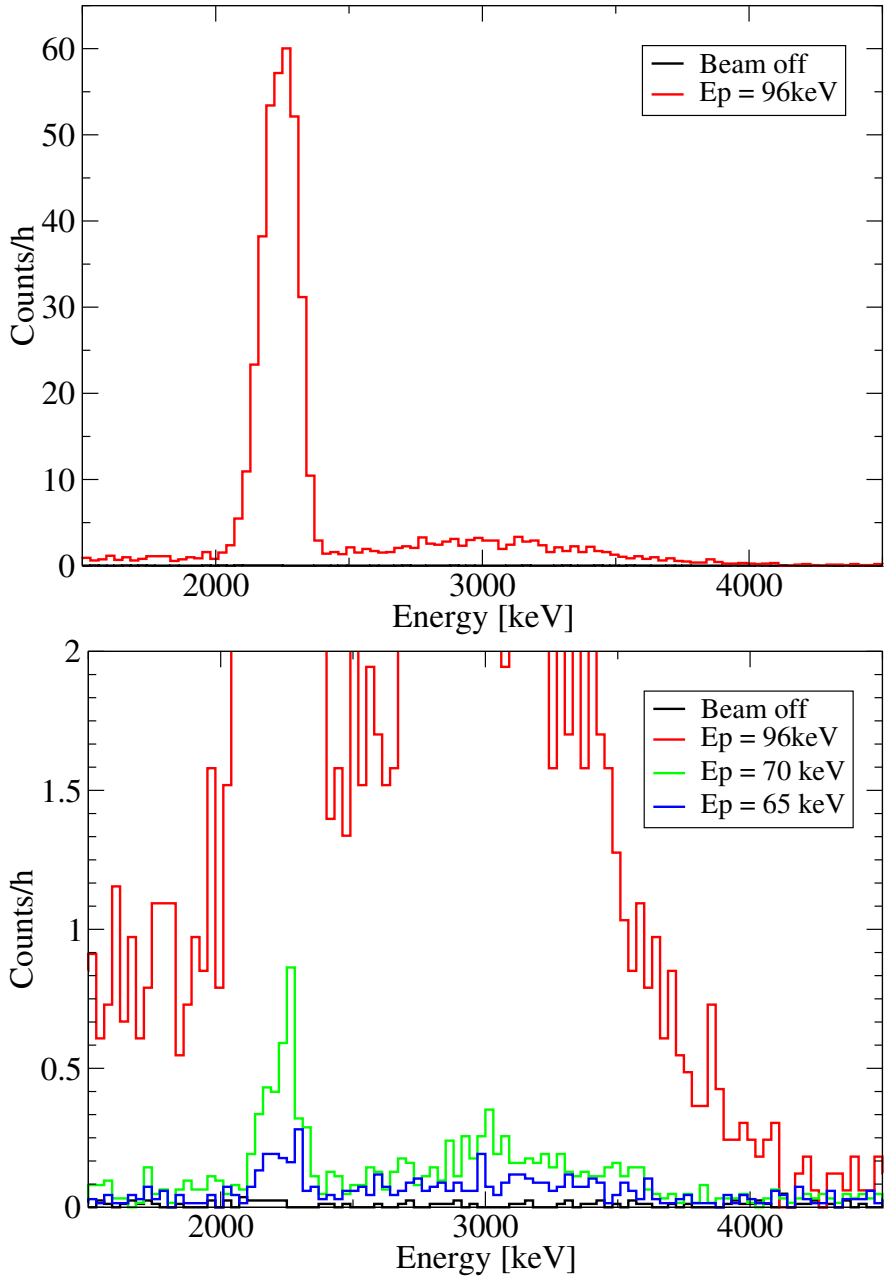

Figure 6.1 *Experimental spectra acquired for the for the $^{18}O(p,\alpha)^{15}N$ reaction at E_p=96 keV (top) and at E_p=96, 70, and 65 keV (bottom). The natural background is too low to be seen in the top figure. Also note the very broad peak of the $^{11}B(p,\alpha)2\alpha$ centred around 3 MeV.*

program. The program was successful at beam energies $95 \leq E_p \leq 360$ keV, but failed to identify the peak consistently at beam energies below 95 keV, for which I manually selected a ROI for the integration instead. At the lowest energy reached of E_p=60 keV, the peak is no longer visible (Fig. 6.1 - bottom) and I employed the same ROI used at E_p=65 keV. After carrying out the integration,

the counts were corrected for the natural background (normalised in time).
If the angular distributions for the ^{18}O(p,α)^{15}N reaction were known, one could obtain the yield using Eq. 2.4. However, not only are the angular distributions not known, they also change with the beam energy as different resonances are excited. In this case, it makes more sense to calculate a differential yield $\frac{dY}{d\Omega}$ employing a straightforward extension of Eq. 2.5, that is

$$\frac{dY}{d\Omega} = \frac{N_D}{N_B \eta d\Omega} \frac{1}{D} \tag{6.1}$$

where N_D is the number of detected (alpha) particles, N_B is the number of (proton) beam particles, $\eta = 1$ is the intrinsic efficiency, $d\Omega$ is the differential solid angle, and D is the yield degradation coefficient introduced in Eq. 5.6. The resulting differential yield as a function of the proton beam energy for upper row detectors ($\theta = 135°$) is shown in Fig. 6.2. The lower row yield ($\theta = 102.5°$ - not shown) is comparable. The resonances previously reported in ref. [44] can be observed at $E_p = 95$, 151, 220 and 330 keV. Furthermore, a previously unobserved pattern in the yield appears just below the $E_p = 151$ keV resonance suggesting the presence of either a new resonance or an interference effect between existing resonances. This "bump" will be studied in greater detail employing the R-matrix technique in Section 6.2.

6.1.4 Thick-target yield profiles

The resonances at $E_p = 95$, 220 and 330 keV show the typical thick-target yield profile (Section 2.2), suggesting that a resonance strength $\omega\gamma$ can be extracted using Eq. 2.11. Unlike the $E_p = 151$ keV resonance, the three resonances at $E_p =$ 95, 220 and 330 keV do not completely dominate the cross-section at the energies at which they are excited. The reaction can proceed either through one of these three resonances, or through a non-resonant mechanism, or through other broad resonances. Therefore, the thick-target yield profile is superimposed on a smooth trend which has to be subtracted in order to extract the $\omega\gamma$ value. For the $E_p =$ 220 and 330 keV resonances this subtraction is relatively straightforward (Fig. 6.3). A second-order polynomial was fitted to the yield at energies higher and lower than the resonance. The polynomial function was then interpolated to the resonance energies and, keeping its parameters fixed, summed to Eq. 4.2 in order to fit the yield profile observed. Results, corrected for electron screening (here,

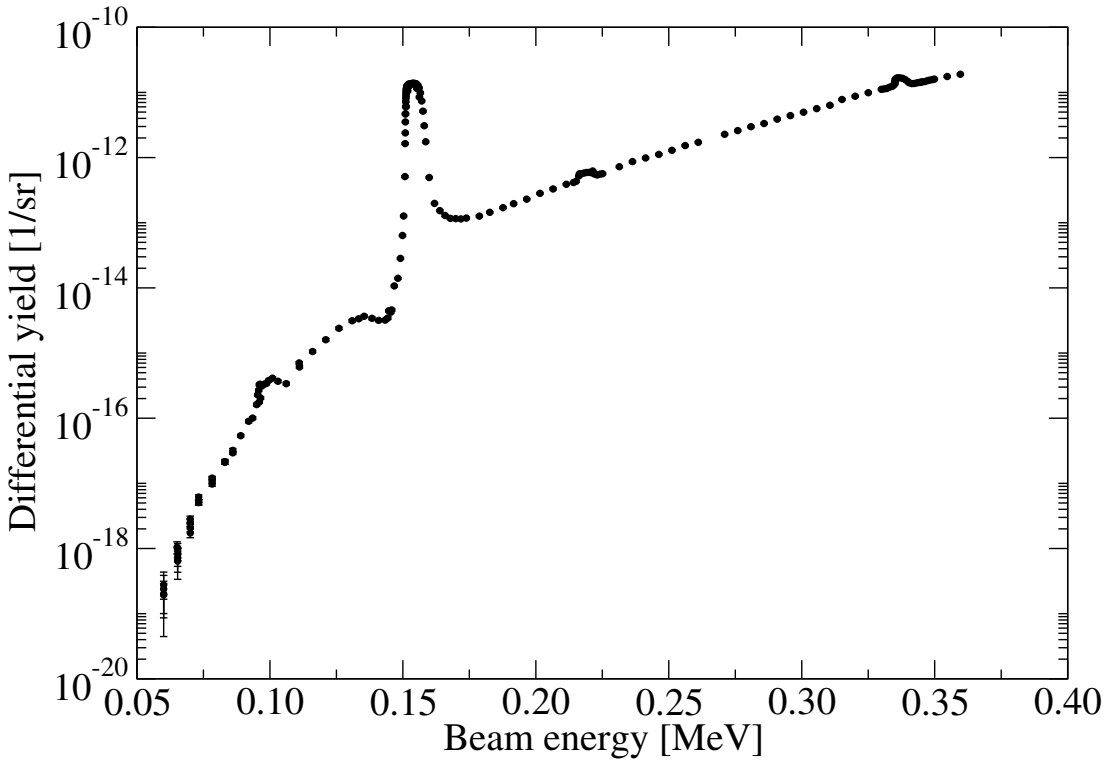

Figure 6.2 *Differential yield of the $^{18}O(p,\alpha)^{15}N$ reaction measured by upper row detectors (135°) as a function of the beam energy in the laboratory frame. Multiple points for a given energy indicate multiple runs acquired at that energy. Statistical errors are too small to be seen except for the lowest beam energies.*

$f_e \simeq 1.01$ – section 2.5), are presented in Table 6.1 and are in good agreement with previous investigations. Note that I only employed data from the three working upper row detectors #1,2 and 3 to reduce the systematic uncertainties like in Section 5.1.

The situation is more complex for the $E_{\rm p}$=95 keV resonance primarily because of the lack of data on 15 keV thick target at energies above the thick-target plateau. The highest energy datapoint available on 15 keV thick targets was acquired at $E_{\rm p}$=103 keV, which is on the falling edge of the profile. Above the resonance, data are only available for 5 keV thick targets, and a simple polynomial fit cannot be carried out. I employed the R-matrix technique to solve this issue. First, I carried out the R-matrix fit described in Section 6.2 excluding data around $E_{\rm p}$=95 keV to obtain the differential cross-section of the ^{18}O(p,α)^{15}N reaction. From the differential cross-section, I calculated the expected differential yield for 15 keV thick targets, using a program similar to the one described in Section 6.1.5. Finally, I subtracted the expected differential yield from data at energies

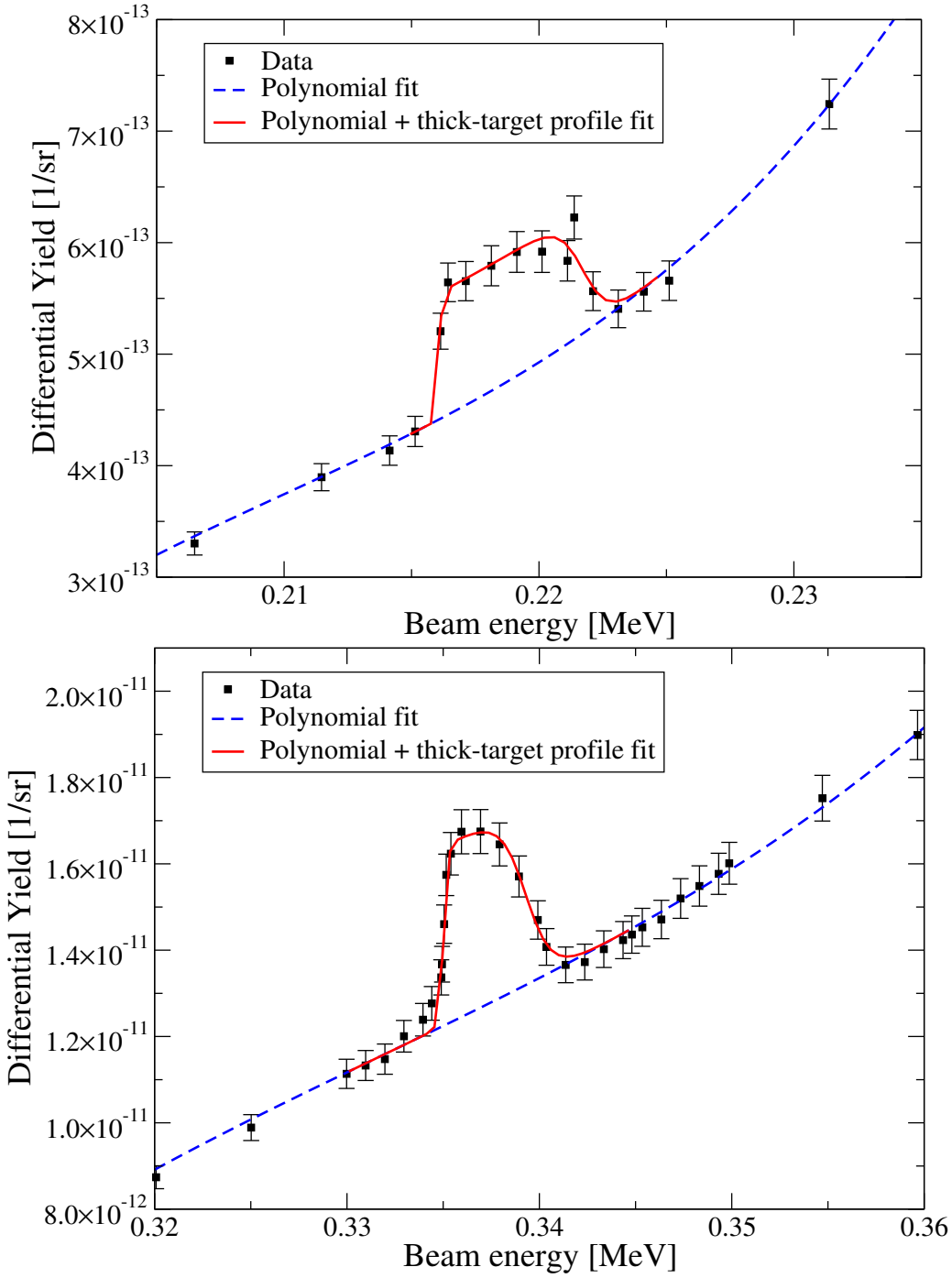

Figure 6.3 *Fits to the thick-target yield profiles of the resonances at E_p=220 and 330 keV (top and bottom respectively), using Eq. 4.2 plus a second-order polynomial. Uncertainties shown are statistical only.*

around the E_p=95 keV resonance and fitted the thick-target yield profile using Eq. 4.2 as shown in Fig. 6.4. The result, after correction for electron screening ($f_e = 1.09$ – section 2.5), is reported in Table 6.1. The $\omega\gamma$ value is approximately an order of magnitude larger than previously reported in refs. [44, 50]. Possible

reasons for this discrepancy will be discussed in Section 6.4 in light of the results in Section 6.2.

Table 6.1 *Results from the thick-target profile fits of the E_p = 95, 220 and 330 keV resonances in $^{18}O(p,\alpha)^{15}N$. For this work, the uncertainty in the resonant energy in the laboratory frame E_r is given by the beam resolution. See Table 6.2 for the uncertainty budget on the $\omega\gamma$ parameter.*

E_p [keV]	E_R [keV]	$\omega\gamma$	Ref.
95	95.2 ± 0.3	$1.73 \pm 0.15_{\text{stat}}\ ^{+0.13}_{-0.12\ \text{syst}}$ μeV	This work
95	95 ± 3	0.16 ± 0.05 μeV	[44]
95	96.6 ± 2.2	0.18 ± 0.03 μeV	[50]
220	216.1 ± 0.3	$2.35 \pm 0.10_{\text{stat}} \pm 0.17_{\text{syst}}$ meV	This work
220	216 ± 1	2.3 ± 0.6 meV	[44]
330	335.0 ± 0.3	$73 \pm 5_{\text{stat}} \pm 5_{\text{syst}}$ meV	This work
330	334 ± 1	57 ± 10 meV	[44]

Table 6.2 *Uncertainty budget for the $\omega\gamma$ values of the E_p = 95, 220 and 330 keV resonances, and for the differential-cross-section data points obtained for the deconvolution procedure of the yield in the $^{18}O(p,\alpha)^{15}N$ reaction. Statistical uncertainty refers to the random sources of error (Poisson and charge integration). The other sources of error are systematic.*

Source	Percent uncertainty
Charge	±2.0%
Tail asymmetry	+2.0%
Stopping power	±4.0%
Efficiency	±5.5%

6.1.5 From yields to cross sections

I followed the procedure described in Section 2.3 in order to extract a differential cross-section from the differential yield obtained in Section 6.1.3. Specifically, I wrote a program to carry out the deconvolution of the yield into a cross-section employing the median energy as the assigned energy (Eqs. 2.18 and 2.19). In order to account for the different thickness of the targets used (5 and 15 keV) as well as the thickness degradation of the targets when subject to beam bombardment (Section 4.5), for every yield data point, the program

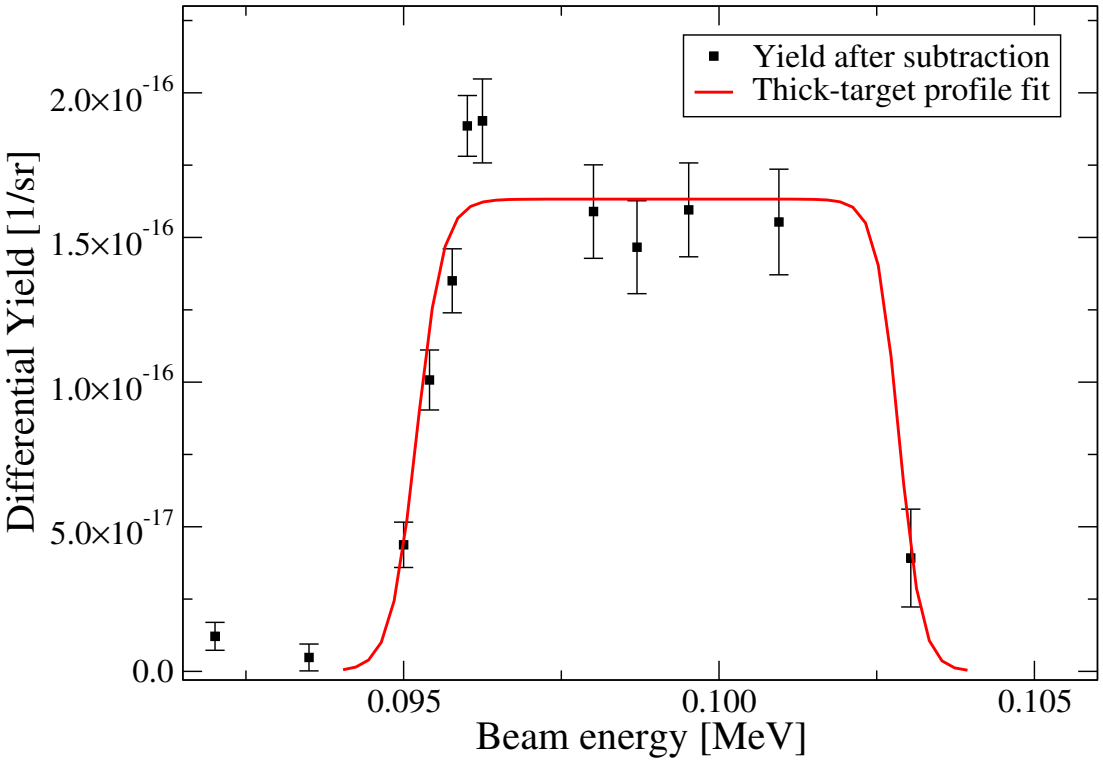

Figure 6.4 *Thick-target profile fit using Eq. 4.2 to the thick-target yield profile of the resonance at $E_p = 95$ keV. The non-resonant yield has been subtracted using a technique based on an R-matrix calculation. The first two points on the left are not included in the fit. See text for details.*

takes as an input the target thickness estimated using the model in Section 4.5. Schematically, the program takes the following steps:

1. Use the thin-target yield approximation (Eq. 2.6) to compute a prior differential cross-section $\frac{d\sigma_{\rm pr}}{d\Omega}$.
2. Correct the prior for the electron screening to obtain a bare prior.
3. For every yield data point i:
   (a) Use the beam energy and the target thickness provided as input (in atoms/cm^2) to compute the energy thickness of the target ΔE_i (in MeV) employing a numerical integration of the SRIM tables [11]
   (b) Use the ΔE_i value derived in the previous step, the prior cross-section $\frac{d\sigma_{\rm pr}}{d\Omega}$ and the stopping power from the SRIM tables in Eq. 2.18 to compute the median energy $E_{m,i}$

(c) Use $E_{m,i}$ and ΔE_i in Eq. 6.2 to obtain the experimental differential cross-section $\frac{d\sigma_{\rm ex}}{d\Omega}(E_{m,i})$. Eq. 6.2 is an extension of 2.19 where the electron screening $f_{\rm e} = f_{\rm e}(E)$ factor is multiplied to the integrand to account for the electron screening in the yield data

$$\frac{d\sigma_{\rm ex}}{d\Omega}(E_{m,i}) = \frac{\frac{dY(E_b)}{d\Omega}}{\int_{E_b-\Delta E}^{E_b} \frac{\frac{d\sigma_{\rm pr}}{d\Omega}(E)}{\epsilon_{\rm eff}(E)} f_{\rm e}(E) dE} \frac{d\sigma_{\rm pr}}{d\Omega}(E_{m,i}) \tag{6.2}$$

4. Calculate the factor M from Eq. 2.15 and use it to compute $(1-M)^2$, the figure of merit for the convergence of the deconvolution procedure. $(1-M)^2$ can be thought as a pseudo-χ^2

5. Consolidate the experimental differential cross-section $\frac{d\sigma_{\rm ex}}{d\Omega}$ by "binning" the data points with the following procedure:

   (a) For every data point, starting with the lowest median energy, check whether there are any other data points with median energies less than 0.3 keV away, where 0.3 keV is the beam resolution. All data points found are placed in one bin

   (b) Calculate the energy of the bin as the average of the median energies and the cross-section of the bin as the average of the cross-sections weighted on the statistical uncertainty

   (c) Restart the consolidation procedure from the lowest energy non-binned data point

6. Use the consolidated cross-section as a new prior and repeat from step (2)

All the integrals are performed numerically using a step-wise procedure. To improve the reliability of the results the quantities to be integrated, *i.e.* the cross-sections and the stopping power, are interpolated using Akima splines[1] from the GNU Scientific Library (GSL) [82]. Furthermore, to reduce the need to interpolate between very different cross-section values, all cross-sections are converted to S-factors in the code. The interpolation of a cross-section is carried out on the S-factor curve, and the result is converted back to a cross-section. The procedure was carried out separately for the working upper row detectors

[1]Akima splines are mathematically more stable than simple linear interpolations and are especially suited for non-monotonic data, see ref. [82, 83] and references within for details.

(#1,2,3) and lower row detectors (#4,5) and the best figure of merit $(1-M)^2$ was obtained after two iterations (see Fig. 6.5). Fig. 6.6 shows the (differential) S-factor for the upper row detectors ($\theta = 135°$) obtained after two iterations, which was adopted as the final results of this procedure, as well as the thin-target prior. The two cross-sections agree at non-resonance energies, where the thin-target approximation is justified, while at resonant energies and low beam energies ($E_m \leq 90$ keV) the thin-target yield approximation breaks down. The S-factor obtained for the lower row detectors ($\theta = 102.5°$ – not shown) has a similar trend.

In order to further check the reliability of this procedure, after performing the R-matrix fit in Section 6.2, I used the R-matrix cross-section as a prior in the procedure described above. The results are essentially the same as those obtained using the thin-target yield approach to generate a prior (see Fig. 6.6). In other words the results of the deconvolution do not depend on the choice of prior cross-section, at least as long as it is reasonable[2].

Finally, for each data point statistical uncertainties were obtained from the statistical uncertainty in the yield, propagated through the deconvolution procedure, while systematic uncertainties were assigned at the end of the procedure (see Table 6.2).

[2]I carried out the procedure described using "unreasonable" priors, including a flat prior and a prior from another reaction. The results are worse than those presented here in terms of $(1-M)^2$ and the final cross-section often shows distinctive "wiggles" around the resonances. However, the correct general trend is usually recovered in a couple of iterations.

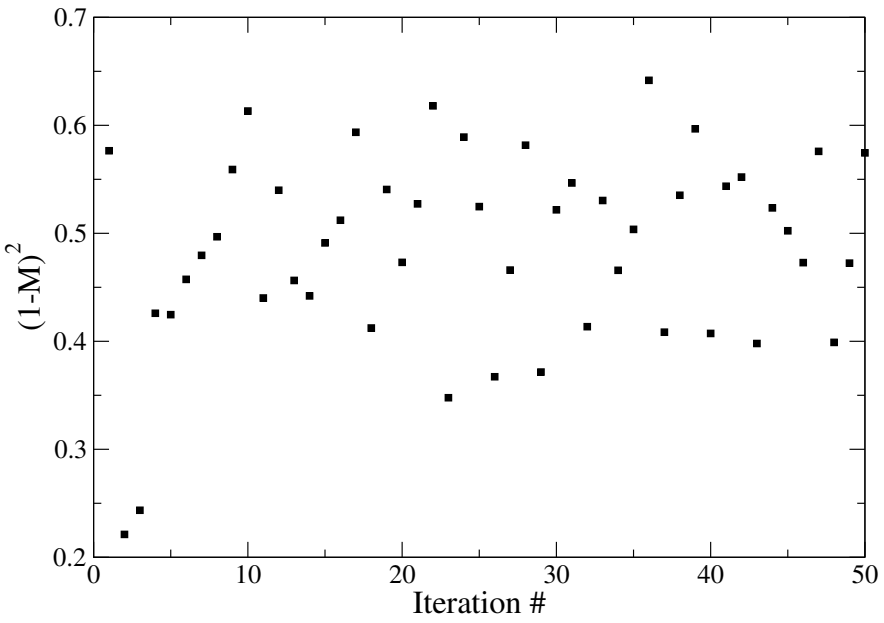

Figure 6.5 *Figure of merit for the convergence of the deconvolution of the upper row detectors ($\theta = 135°$) yield to a cross-section. The M factor is defined in Eq. 2.15. Lower $(1 - M)^2$ values correspond to better deconvolutions.*

6.2 The R-matrix analysis

6.2.1 Preparing the data

In order to calculate a precise value of the rate of the ^{18}O(p,α)^{15}N reaction, I performed an R-matrix fit to data acquired in this work as well as previously published data. Using multiple datasets, acquired with different experimental techniques, allowed me to reduce the systematic uncertainties in the fit and therefore the final uncertainty in the reaction rate. In order to carry out an R-matrix fit I employed two R-matrix programs: AZURE2 [76] and Rmatrix2015 (also known as DREAM) [84]. In addition to the differential cross-section obtained in the previous section, I included in the fit the datasets in Table 3.2 with two exceptions. First, I was unable to fit data on the ^{15}N(α,α)^{15}N reaction from ref. [49] together with the other datasets, possibly because of the poor energy resolution. Even a one-channel R-matrix fit considering just the data from ref. [49] proved to be too challenging to perform in the energy region relevant for this work. Other than the poor energy resolution, the reasons for these issues are not immediately obvious and new data on ^{15}N(α,α)^{15}N at the relevant energies would

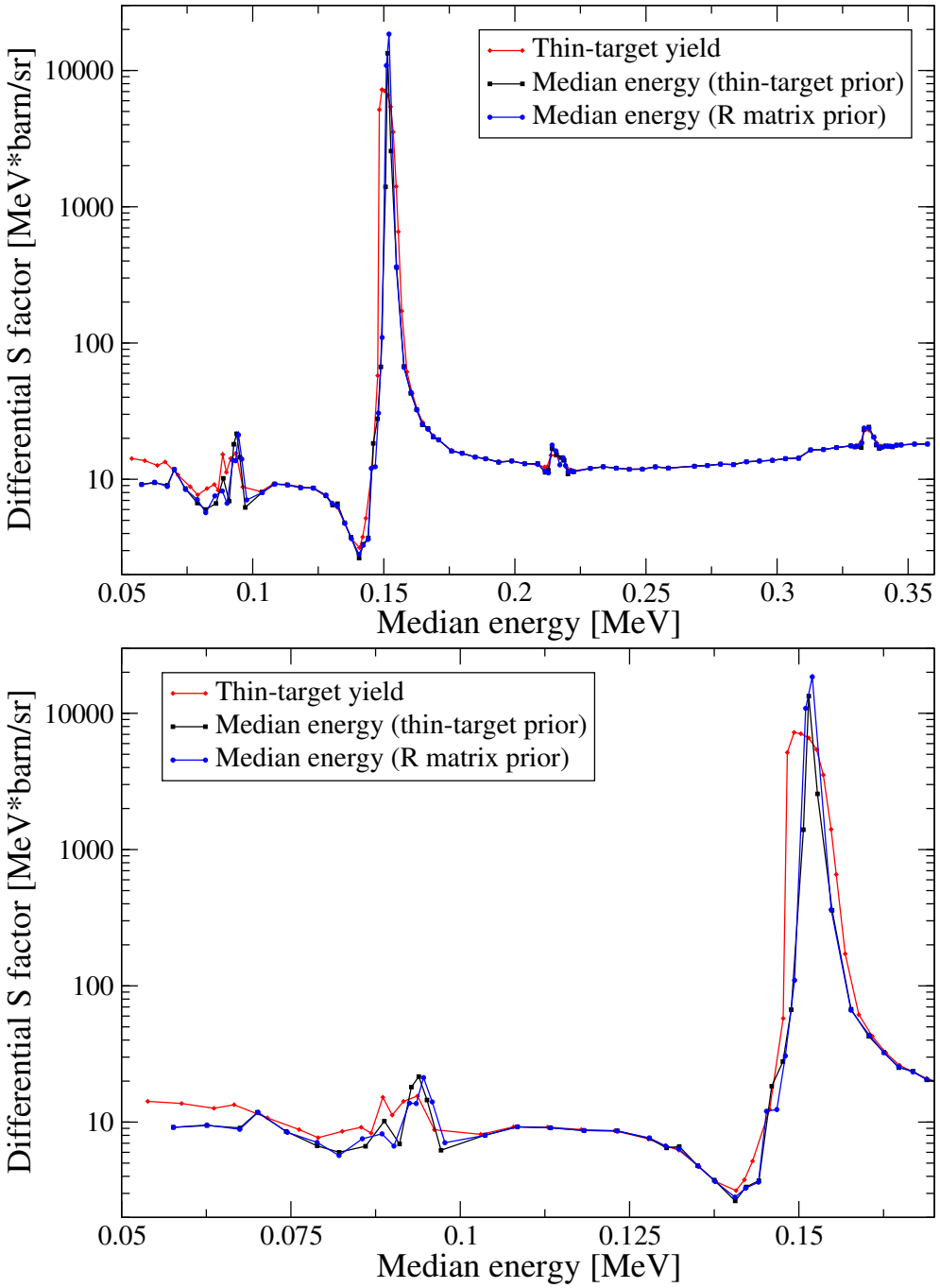

Figure 6.6 *Differential S factor for upper row (135°) detectors obtained through three different approaches. Full energy scale (top) and low energies only (bottom). The results from the two median energy techniques are almost indistinguishable. Uncertainties are not shown. See text for details.*

be needed to solve the problem.

The second exception were data on the ^{18}O(p,α)^{15}N reaction from Lorenz-Wirzba 1978 [44], which were acquired at $\theta = 90°$ and 135° at energies E_{CM} = 70–

886 keV partly overlapping with those of this work (E_{CM} = 50–340 keV). I compared the data acquired at $\theta = 135°$ in this work and in ref. [44], and found an excellent agreement above $E_{\mathrm{CM}} = 170$ keV. However, the trends below $E_{\mathrm{CM}} = 170$ keV are not in good agreement, and especially below $E_{\mathrm{CM}} = 90$ keV there are obvious tensions between the two datasets. The tensions may be a result of the higher background and poorer statistical significance in ref. [44]. To avoid issues with the R-matrix fit, I decided to discard data from ref. [44] (at both angles) below $E_{\mathrm{CM}} = 170$ keV. An alternative approach could have been to increase the uncertainty in these data significantly, but the effect would have been to artificially reduce the χ^2 value, without adding any real constraints to the fit.

The datasets employed in this R-matrix calculation were never published in numerical form. In order to include the data in my fit, I relied on the digitised version of the data provided in the EXFOR [85] database. These data are obtained from digital scans of printed plots and are in general not very reliable; therefore I decided to arbitrarily assign a ±10% uncertainty to all cross-section data points, unless the digitised uncertainty was higher. The uncertainty in the (differential) cross-section of the data points obtained in this work were taken as the sum in quadrature of the statistical and systematic uncertainties. Neither R-matrix program I employed allows the user to define uncertainties in energy. These uncertainties cannot be neglected next to narrow resonances. To account for this additional source of uncertainty, for every data point acquired at LUNA, I interpolated the cross-section 0.3 keV before and after the median energy E_m of the data point, and took the average of the difference as an additional uncertainty in the cross-section, i.e.

$$\Delta_\sigma = \frac{1}{2}\left(|\sigma(E_m) - \sigma(E_m + \delta E)| + |\sigma(E_m) - \sigma(E_m - \delta E)|\right) \tag{6.3}$$

where δE is 0.3 keV, the beam energy uncertainty. This method is an extension of the one proposed in ref. [73] which only works on monotonic (i.e. non-resonant) datasets. The resulting Δ_σ was treated as an additional source of systematic uncertainty and added in quadrature to the others. In general the impact of Δ_σ was larger near resonances. In particular, Δ_σ was larger than the central values of two data points on the rising front of the E_{p}=151 keV resonance. These data points would not have constrained the fit and were discarded. From a physical point of view, the meaning of this large uncertainty is that the precise value of the rising front of the E_{p}=151 keV cannot be found with an energy resolution

better than that of the beam, and therefore the data acquired cannot constrain the R-matrix fit.

6.2.2 Performing the fits

In order to start my R-matrix fit I needed some initial parameters, which I attempted to obtain from the literature. Previous attempts to perform R-matrix fits to the datasets were made, among others, in refs. [43, 45, 48], but they are not completely satisfying for different reasons

- Yagi 1962 [48] performs a fit to data on both ^{18}O(p,p)^{18}O and ^{18}O(p,α)^{14}N, but at the time no data were available below E_{p}=600 keV which is quite far from the energies considered in this work.
- Mak1978 [45] performs an R-matrix fit, but places a background state in between physical ones. This is not physical as a background state (see Section 2.4.4) and compromises the validity of the results.
- La Cognata 2010 [43] does perform a fit to Trojan Horse Method (indirect) data as well as direct data, but details on which states and datasets were considered are incomplete.

I included two channels in my fit, alpha and proton, and employed a channel radius $a = 1.4\times(18^{1/3}+1^{1/3}) = 5$ fm for both. I observed no significant differences in the results using $a = 5.5$ and 6.5 fm, proving that $a = 5$ fm is sufficiently large for the R-matrix approximation to work in this system (section 2.4). I started my R-matrix fit, using rmatrix2015, from the two broad resonances at $E_{\mathrm{p}} \simeq 600$ and 800 keV which are reported [43] to dominate the cross-section down to the energies $E_{\mathrm{p}} = 151$ keV resonance. Both resonances have $J^{\pi} = 1/2^{+}$ and therefore interfere (Section 2.4.3). I used the widths and resonant energies reported in refs. Yagi 1962 [48] and La Cognata 2010 [43] and found that the correct interference sign is clearly negative[3]. Fig. 6.7 shows the contribution of the two resonances at $E_{\mathrm{p}} \simeq 600$ and 800 keV to the (differential) S factor according to the parameters proposed in refs. Yagi 1962 [48] and La Cognata 2010 [43]. The R-matix calculation is compared against data acquired in this

[3]Based on the plots published, the interference sign used in refs. [43, 48] was negative as well.

work by the upper row (135°) detectors as well as data acquired at the same angle in ref. [44].

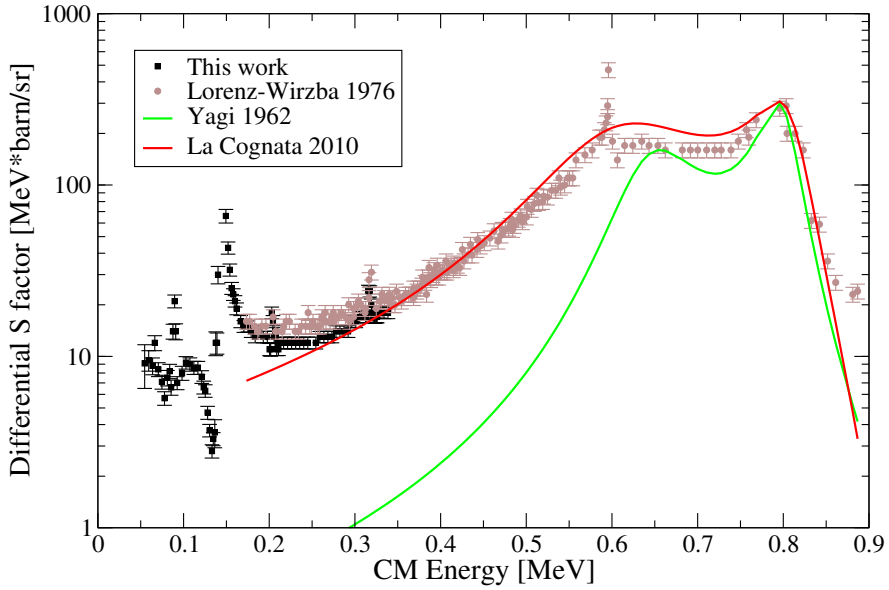

Figure 6.7 *S factor for the $^{18}O(p,\alpha)^{15}N$. Experimental data points come from this work and ref. [44]. The two R-matrix calculations presented were carried out using the parameters proposed in refs. Yagi 1962 [48] and La Cognata 2010 [43]. Two data points for the E_p=151 keV resonance are above 1000 MeV*barn/sr and are not shown for clarity.*

The agreement of the calculation using the parameters in Yagi 1962 is poor below E_{CM} = 600 keV, which is expected since at the time no data below this energy were available. On the other hand, the agreement between the *R*-matrix calculation and the data in Fig. 6.7 is quite good using the parameters in La Cognata 2010. Even though the agreement for other datasets (not shown) is quite poor, I decided to start the *R*-matrix fit with the parameters of La Cognata 2010. My next step was to add the resonance at E_p = 151 keV according to the results obtained in this work. The resonant energy and the proton width are known, but to my knowledge the alpha width is unknown. I optimised the alpha width by hand and obtained the result shown in Fig. 6.8. Note this E_p = 151 keV resonance also has $J^\pi = 1/2^+$ and interferes with the other two resonances already included. The *R*-matrix calculation in Fig. 6.8 assumes a positive sign for the interference, which gave the best match between data and calculations.

While the agreement obviously improves, before trying to fit the other weaker resonances I attempted to improve the situation at low energies, which are still not being reproduced properly, by adding a background state at E_{CM} = 12 MeV

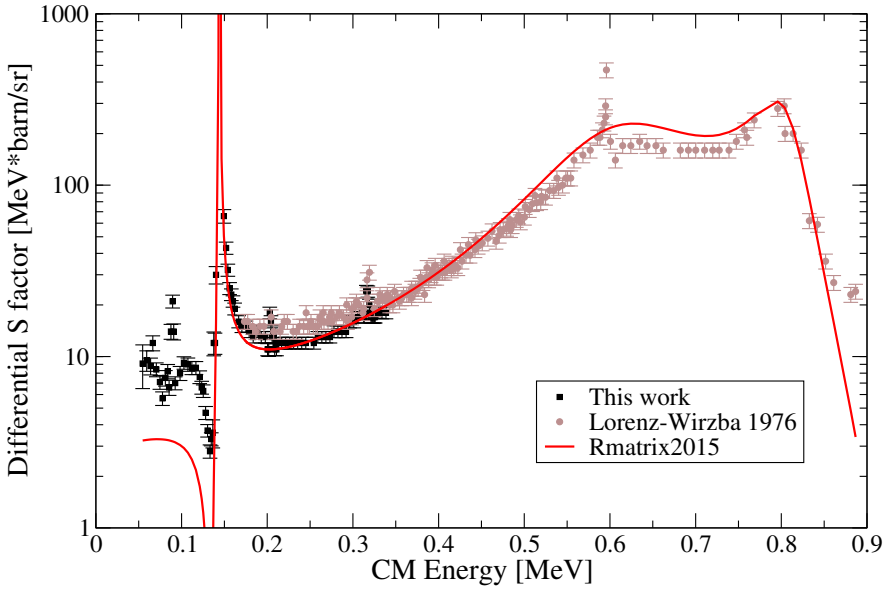

Figure 6.8 *As Fig. 6.7, after adding the $E_p = 151$ keV resonance.*

with $J^\pi = 1/2^-$. The reason for this choice is that $J^\pi = 1/2^-$ corresponds to an angular momentum of $l = 1$ in the entrance channel and $l = 0$ in the exit channel. No other resonance below $E_{CM} = 1$ MeV has $J^\pi = 1/2^-$, but since the momentum conditions are favourable, it seems reasonable to assume some contribution in this partial wave from a higher-energy resonance that is not included in the fit. Furthermore, in R-matrix theory a background state is also the way to model a non-resonant contribution to the cross-section which could play a role in this reaction, especially at low energies. After adding the background state I had to fit its parameters to reproduce the data. The agreement improves again (Fig. 6.9), but there is still a "bump" around $E_{CM} = 110$ keV which remains unexplained. I was unable to reproduce this bump with any combination of background states or by altering the parameters of the $E_p = 151$ keV resonance. Furthermore, while the addition of the background state improves the agreement between data and theory for the ^{18}O(p,α)^{15}N reaction at $\theta = 135°$, the situation is still not as good for other datasets (not shown), and in particular for the data acquired in this work with the lower row detectors (102.5°).

In order to solve this issue I first tried adding the narrow resonance just below $E_{CM} = 600$ keV, in case its absence was influencing the fit algorithm. Adding this resonance according to the parameters suggested in ref. [48] improved the fit, but not at low energies. I then added the weaker resonances at $E_p = 95, 220, 330$ using the parameters obtained in Section 6.1.4. Since the alpha width for these three

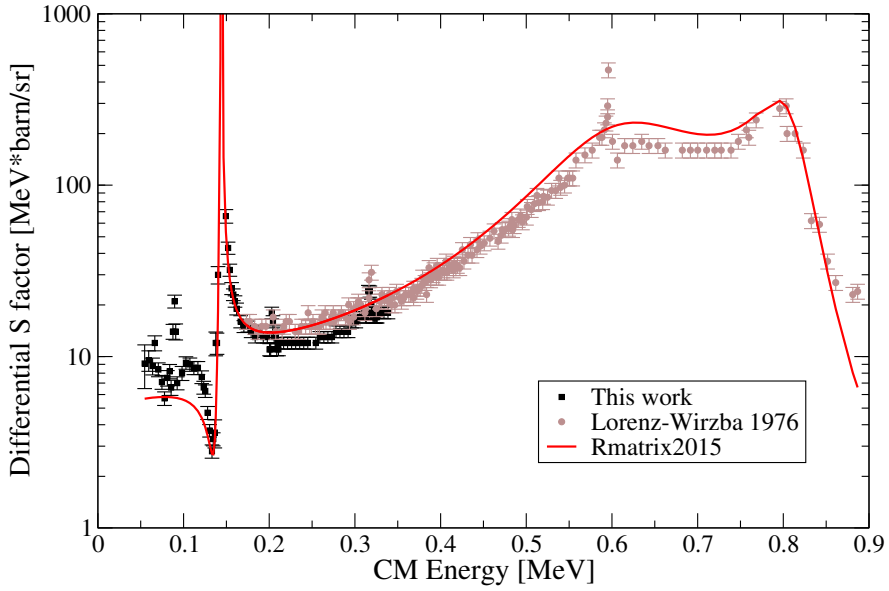

Figure 6.9 *As Fig. 6.8 with the addition of a background state.*

resonances is unknown, I assumed $\Gamma_{\rm tot} \simeq \Gamma_\alpha$ to obtain Γ_p from the $\omega\gamma$ value, and fitted Γ_α to the data. After adding these four resonances and re-optimising the fit parameters, the agreement improves significantly (Fig. 6.10). This is especially true for the data acquired by the lower row detectors in this work (not shown), however the bump at $E_{\rm CM} = 110$ keV remains unexplained.

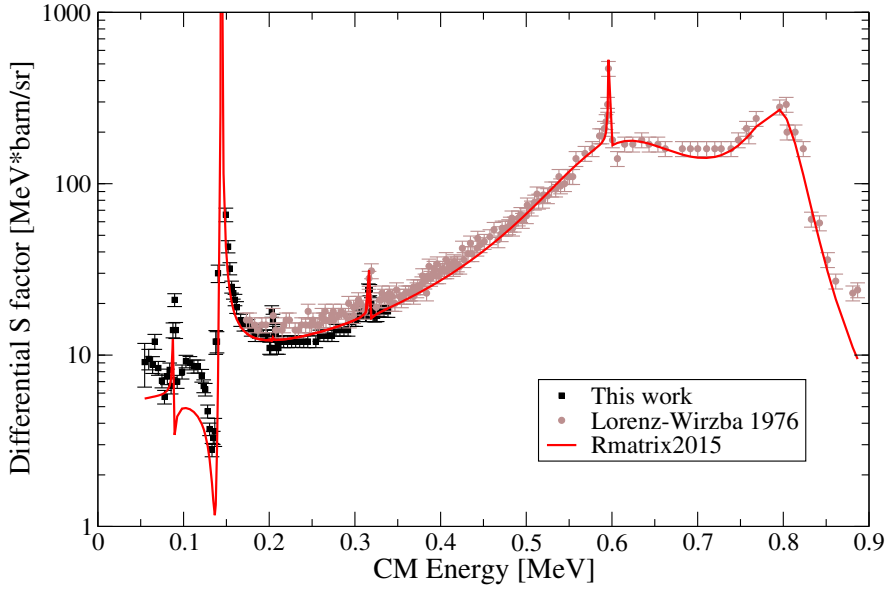

Figure 6.10 *As Fig. 6.9 with the addition of the four narrow resonances at* $E_{\rm p} =$ *95, 220, 330 and 600 keV and optimisation of the fit parameters.*

In order to solve this outstanding issue, I tentatively added a new state at $E_{\rm p} =$

120 keV with a total width of 10 keV and attempted to improve the agreement by optimising the fit parameters. I made this attempt for different values of J^π (Fig. 6.11) and found very similar reduced χ^2 ($\simeq 2.7 - 3.0$) values for each spin-parity assignment. The lowest reduced χ^2 value was obtained for $J^\pi = 3/2^+$, but this assignment should be considered tentative since the statistical evidence is quite weak.

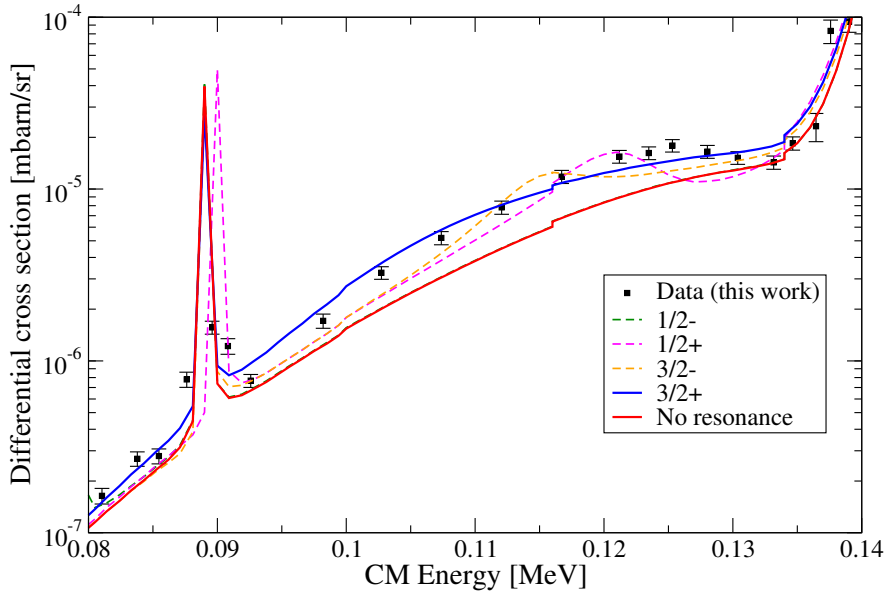

Figure 6.11 *R matrix fits to the $^{18}O(p,\alpha)^{15}N$ for different J^π values of the new resonance at $E_p = 120$ keV. The best agreement (reduced $\chi^2 = 2.7$) is obtained for $J^\pi = 3/2^+$. Note that the plot shows the differential cross-section as opposed to differential S-factor.*

I performed a final optimisation of all parameters (Fig. 6.12). By adding the new resonance at $E_p = 120$ keV, the agreement between the R matrix calculation and the experimental data improves significantly (reduced $\chi^2 = 3.0$). I repeated the same procedure described above employing AZURE2 instead of Rmatrix2015. In addition to fitting the resonant energies and widths of the states involved in the R-matrix calculation, AZURE2 also allows each dataset to be normalised by an arbitrary coefficient which can be optimised by the fit. This additional coefficient allows one to account for systematic shifts between datasets due to *e.g.* incorrect efficiency or stopping power values. For this fit, I allowed the normalisation coefficient to vary between 0.95 and 1.05, where 1.00 corresponds to no normalisation. Thanks to the presence of these additional normalisation parameters, the final agreement between the data and the fit (Fig. 6.13) is further improved (reduced $\chi^2 = 2.7$). I decided to employ the AZURE2 fit to obtain the physical parameters of the states involved in the reaction to be used in the

calculation of the reaction rate.

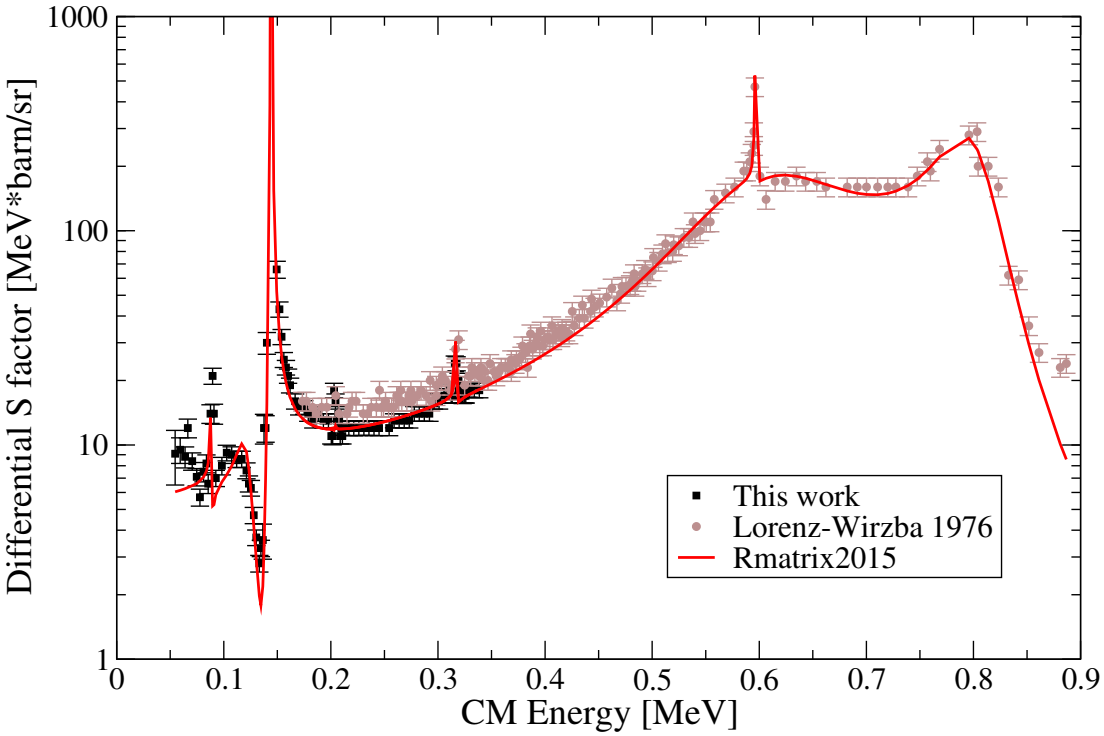

Figure 6.12 *As Fig. 6.10 with the addition of the new resonance at* $E_{\mathrm{p}} = 120$ *keV.*

6.2.3 Results of the R-matrix analysis

The fit parameters obtained from the final AZURE2 fit are shown in Table 6.3. The uncertainty in the parameters (*e.g.* $\Gamma_{p,143.7}$) derived from thick-target analyses are derived from the uncertainties in the $\omega\gamma$ value. The other uncertainties are obtained from the fitting procedure, and are statistical only. For instance, the two broad resonances at $\mathrm{E}_r = 610.7$ and 798.2 keV have very small uncertainties in the resonant energies, reflecting the (statistical) precision with which the optimum E_i parameter in the R-matrix fit is known. This uncertainty is not necessarily a fair reflection of *e.g.* the systematic uncertainties in the original measurements. I decided to conservatively assign a minimum uncertainty of ± 0.3 keV (beam energy uncertainty in LUNA) to all resonant energies. For resonances that were not measured in this work, the meaning of this minimum uncertainty is that the new data cannot constrain the resonant energies with a precision better than 0.3 keV.

The fit had a total of 34 free parameters, and the correlation matrix R (34×34)

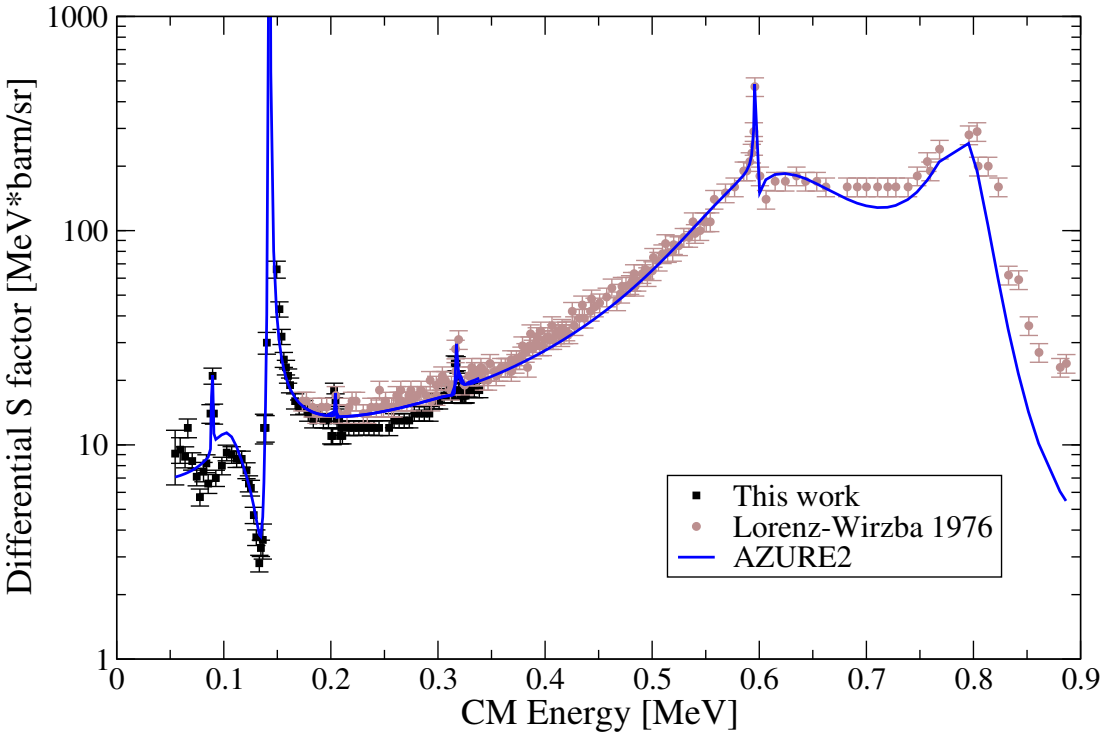

Figure 6.13 *As Fig. 6.12 employing AZURE2 instead of Rmatrix2015 in order to allow for the possibility of a ±5% normalisation coefficient for each dataset.*

will not be reported for space constraints, but there do not appear to be significant correlations between the parameters ($|R_{i,i}| \lesssim 0.5$). The parameter set obtained from the Rmatrix2015 fit (not shown) is largely in agreement with the parameter set in 6.3, except for the parameters of the background state at 12 MeV. However these parameters are not supposed to have an immediate physical meaning (Section 2.4.4) as they control the height of the constant contribution of the background state to the cross-section. Generally speaking, the parameters in Table 6.3 are in broad agreement with previous works [48, 43]. See Section 6.4 for a more in-depth comparison.

6.3 Reaction rate

I used RatesMC to calculate the reaction rate from the results of the R-matrix fit. One of the limitations of the code is its inability to include more than two interfering resonances [20], and in this case the E_R = 143, 611 and 798 keV resonances (Table 6.3) have the same $J^\pi = 1/2^+$ and do interfere. In principle

Table 6.3 *Fit parameters obtained from the R-matrix AZURE2 fit of the $^{18}O(p,\alpha)^{15}N$ reaction. All quantities are given in the CM frame. Values in* **bold** *were included in the calculation, but not optimised by the fit. See text for details on the uncertainties. Interf. refers to the sign of the off-diagonal interference between resonances.*

J^π	E_r [keV]	Γ_p	Γ_α	Interf.
$1/2^+$	**142.8±0.3**	**164 ± 12 meV**	79 ± 1 eV	+
$1/2^+$	610.7±1.3	6.33 ± 0.07 keV	154 ± 1 keV	-
$1/2^+$	798.2±0.4	24.6 ± 0.3 keV	24.5 ± 0.4 keV	+
$3/2^-$	89.1±0.3	**866 ± 61 neV**	124 ± 9 eV	+
$3/2^-$	596.1±0.3	33.3 ± 1.5 eV	610 ± 45 eV	+
$(3/2^+)$	104±2	3.0 ± 0.2 μeV	34 ± 2 keV	+
$5/2^+$	**204.4 ± 0.3**	**0.78 ± 0.05 meV**	15.2 ± 2.2 eV	+
$5/2^+$	**317.2 ± 0.3**	**24.2 ± 1.7 meV**	1.43 ± 0.05 keV	-
$1/2^-$	**12000**[a)]	87 MeV	48 MeV	+

[a)] Background state

it would be possible to obtain the reaction rate from a numerical integration of the cross-section, but that would not result in a precise estimate of the uncertainties. In order to solve this problem, I calculated the reaction rate with RatesMC following the approach in ref. [20], using the input file employed in ref. [20] and replacing only the values presented in Table 6.3. I calculated three reaction rates neglecting in turn the interference contribution of one of the three resonances at E_R = 143, 611 and 798 keV. All three resonances were always included in the calculation, only the interference contribution of a given resonance was neglected. I compared the three reaction rates obtained for the three possible combinations (Fig. 6.14) following this approach. The rates obtained considering the interference between the E_R = 142 keV resonance and either of the other two are in very good agreement, while the rate computed considering the interference between the E_R = 611 and 798 keV resonances is markedly different at temperatures lower than 0.08 GK or higher than 0.18 GK.

At a given temperature, the most reliable rate will be the one that takes into account the interference of the dominant resonances at that temperature. Therefore, following an approach similar to that of ref. [20], I adopted the final reaction rate at temperatures $T < 0.10$ GK from the calculation performed considering the interference between the resonances at E_R = 143 and 611 keV, while at temperatures $T \geq 0.10$ GK I adopted the rate from the calculations considering the interference between the resonances at E_R = 611 and 798 keV.

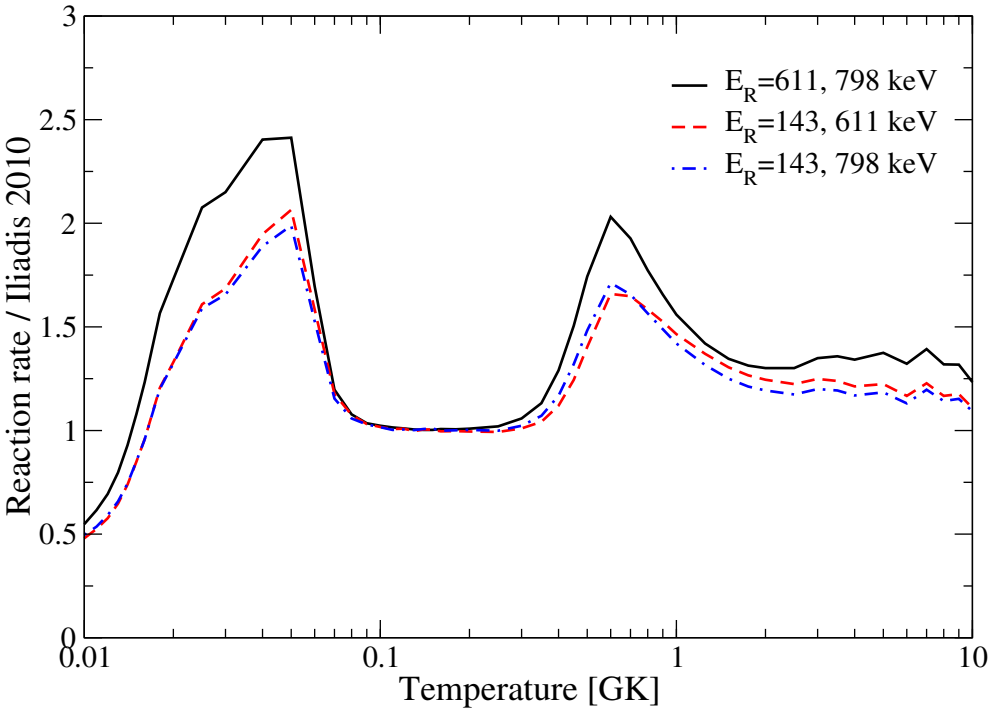

Figure 6.14 *Comparison between the reaction rates computed with RATESMC using the parameters obtained in this work. The three lines refer to the three reaction rates calculated considering the interference between two out of the three resonances with* $J^\pi = 1/2^+$ *at* $E_R =$ 143*, 611 and 798 keV. All three resonances were always included in the calculations, only the interference was neglected. The reaction rate is normalised to the value reported in ref. [79]. See text for details.*

This rate, together with the rate proposed in ref. [20], are shown in Fig. 6.15 normalised to the reference rate of the compilation in ref. [79]. In spite of the addition of a new resonance at $E_R = 104$ keV and the significant increase in the $\omega\gamma$ value of the resonance at $E_R = 89$ keV, the final reaction rate is lower than the one in ref. [20], likely as a result of the new and improved constraints of the three resonances with $J^\pi = 1/2^+$. As a result of these constraints and of the multi-channel R-matrix fit, the uncertainty in the reaction rate is significantly reduced at the temperatures shown. Note that ref. [20] adopts an weighted average of the parameters previously published to calculate the reaction rate. The R-matrix fit presented in this work is the first attempt at fitting all available datasets to minimise the systematic uncertainties.

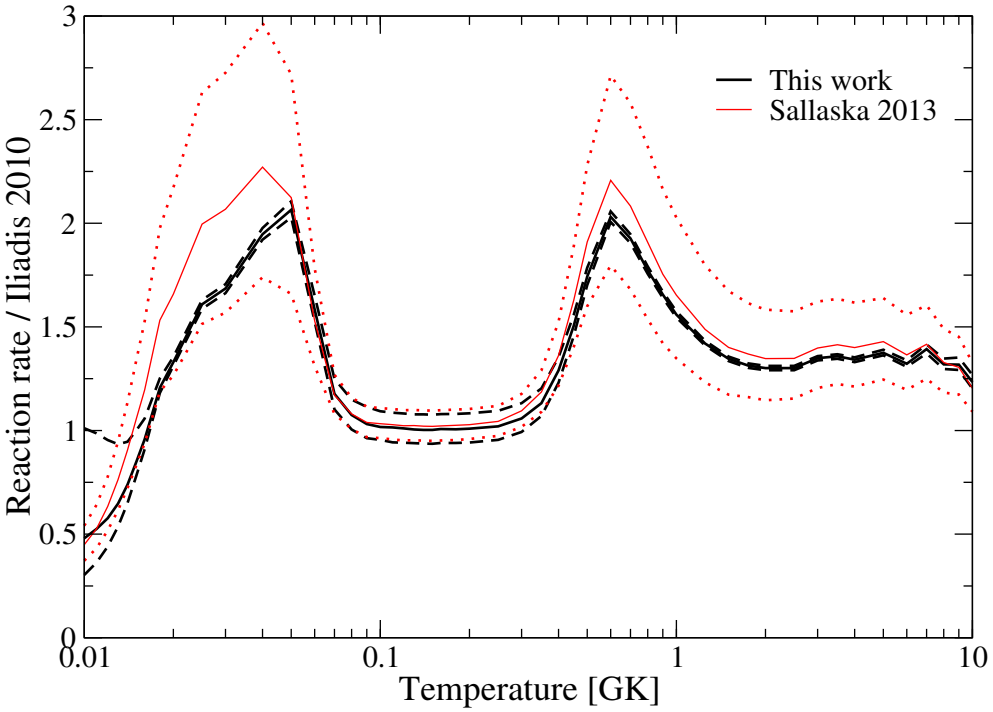

Figure 6.15 *Comparison between the reaction rate adopted in this work (solid black line) and the one proposed in ref. [20] (solid red line). Dashed and dotted lines indicate recommended upper and lower limits. The data in this work supplies new and stringent constraints to the extrapolation of the resonances at lower temperatures, significantly reducing the uncertainty.*

6.4 Comparison with previous measurements

Thanks to the background suppression afforded by the underground environment, we were able to measure the cross-section of the ^{18}O(p,α)^{15}N reaction to the lowest CM energy to date, greatly reducing the uncertainties (both statistical and systematic) compared to previous measurements [44]. The reduction in the statistical uncertainties allowed us to detect a previously unknown resonance at E_R = 104 keV, though I was unable to make an unambiguous J^π assignment because of the poor angular resolution in this experiment.

Finally, I observed a strength of the E_R = 89 keV approximately an order of magnitude higher than previously reported. The widths of the state associated with this resonance had previously been questioned [52], but it is not obvious whether the new $\omega\gamma$ value in this work would go in the direction of solving the inconsistencies reported. Resonance strength values for this E_R = 89 keV were previously reported in refs. [44, 50]. The value reported in ref. [44] may have

been affected by the very large (±3 keV) uncertainty assigned to the energy of the $E_R = 89$ keV resonance and it is possible that the peak of the resonance was not found. For what concerns ref. [50], the method employed is very different (Trojan Horse) and a simple comparison with the results in this work cannot be carried out. The presence of the new resonance at $E_R = 104$ keV will have affected the deconvolution shown, but it is not obvious whether the impact of an additional resonance could be enough to explain the large difference observed.

Chapter 7

Astrophysical implications

This chapter summarises some of the most important astrophysical implications of the revised reaction rates of the ^{17,18}O(p,α)^{14,15}N reactions presented in the previous two chapters. See refs. [10, 4] for more details.

7.1 Origin of meteoric stardust

The puzzle of the grains produced by massive ($M \geq 4M_{\odot}$) AGB stars was presented in section 1.2. Models predict that massive AGB stars should produce significant amounts of cosmic dust, and yet no pre-solar grain appears to match the HBB signature expected from these stars [4]. The most obvious candidates, Group II grains, have ^{17}O/^{16}O ratios that are a factor of two lower than expected. The factor of two increase in the rate of the ^{17}O(p,α)^{14}N reaction translates directly into a factor of two reduction in the expected ^{17}O isotopic content, which now closely matches the observed values. Fig. 7.1 shows a comparison between model predictions of the isotopic ratio ^{17}O/^{16}O against the values observed in Group II grains. The isotopic ratios observed in Group II grains are well reproduced using the rate obtained in this work (LUNA) at typical HBB temperatures in massive AGB stars. On the other hand, at typical CBP temperatures in low-mass AGB stars, only the lowest observed ratios are reproduced. This result suggests that massive AGB stars are the most likely site of origin for Group II grains. Furthermore, our result provides direct evidence that these stars do contribute to the dust inventory from which the Solar System

formed [4].

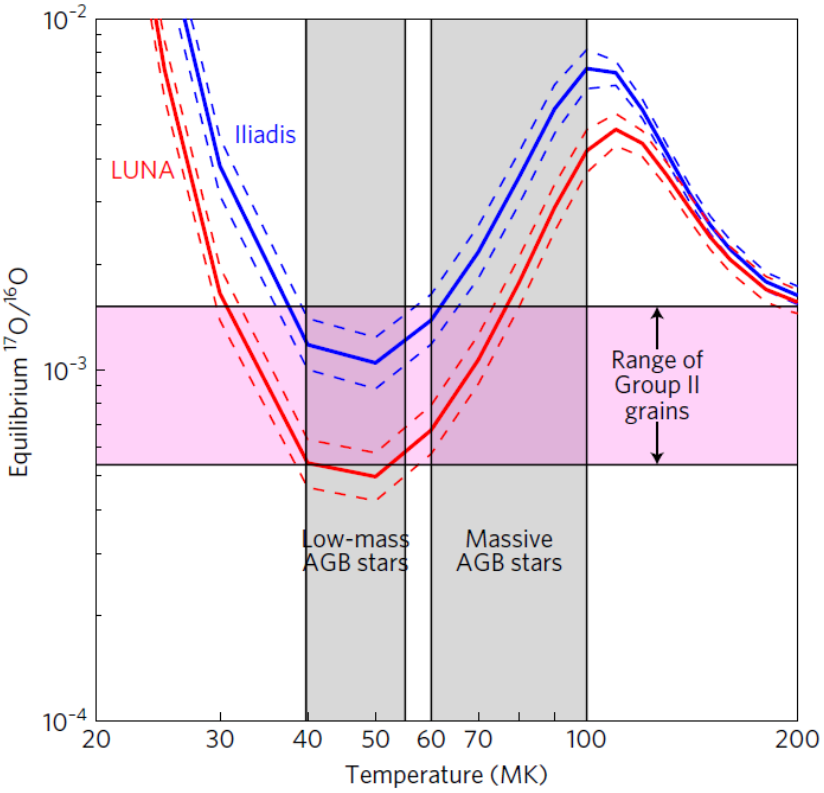

Figure 7.1 *Equilibrium $^{17}O/^{16}O$ ratio defined as the ratio of the production to destruction rate of ^{17}O in the temperature of range for AGB stars. The two lines show the ratio derived in this work (LUNA) and that in ref. [79] (Iliadis). The pink horizontal band indicates the ratio observed in Group II grains. See text and ref. [4] for details.*

7.2 Galactic chemical evolution

One of the net results of the CNO cycle is the enrichment of ^{17}O, and all stars where hydrogen burning is active contribute to the synthesis of this oxygen isotope [10]. When these stars enter the RGB phase and lose mass to stellar winds after the first dredge-up, ^{17}O is injected in the interstellar medium (ISM), polluting the gas clouds that may eventually collapse into new stars. Indeed, astronomical observations of stars belonging to populations of different ages confirm [86] that the abundance of ^{17}O increases with time. The revised rate of ^{17}O(p,α)^{14}N reaction proposed in this thesis work increases the destruction rate of ^{17}O, and therefore it reduces the expected ^{17}O enrichment of the ISM with

time. Specifically, stellar models show [10] that the amount of ^{17}O injected in the ISM is reduced by 20 to 40% for stars in the mass range $2.5M_{\odot} \leq M \leq 20M_{\odot}$, depending on the star mass. This result may have significant implications for Galactic chemical evolution models, and will improve the constraints on the initial isotopic abundances of some types of stars including RGBs in open clusters [10].

7.3 Potential implications of the ^{18}O(p,α)^{15}N reaction rate

In general, hydrogen burning of ^{18}O is extremely efficient [87] and therefore expected abundances for this oxygen isotope are significantly lower than solar in many scenarios, such as massive AGB stars [4]. Results from stellar models using the enhanced ^{18}O(p,α)^{15}N reaction rate proposed in this work confirms previous predictions for several stellar sites, including in particular those discussed in the previous two sections [87, 88]. Work is in progress to quantify the impact of the revised reaction rates in other scenarios, such as low mass AGB stars [89].

Chapter 8

Conclusions and summary

The ^{17,18}O(p,α)^{14,15}N nuclear reactions affect the abundances of the rare, stable ^{17,18}O isotopes in a number of stellar sites. These two isotopes can be used to trace and constrain the mixing and convection processes in RGB and AGB stars. Precisely determining the rate of the ^{17,18}O(p,α)^{14,15}N reactions improves our understanding of the evolution of stars that are in, or will enter, the RGB and AGB phase, including our own Sun.

This thesis work described an experimental campaign aimed at measuring both nuclear reactions at the underground LUNA accelerator, in Gran Sasso Laboratory, Italy. The study was carried out in direct kinematics, accelerating a proton beam onto a $Ta_2^{17,18}O_5$ target and detecting the alpha particles produced by the reaction at backward angles using an array of silicon detectors. The background reduction provided by the underground environment proved critical for the success of both experimental investigations.

We measured a resonance at $E_p = 70$ keV in ^{17}O(p,α)^{14}N which dominates the reaction rates at temperatures of RGB and AGB. We observed a strength for this resonance approximately a factor of two higher than previously reported, which translates into an enhancement of the reaction rate by a factor of two. Our result solves a long-standing puzzle on the attribution of pre-solar grains generated by massive AGB stars, and provides the first direct evidence of HBB signature in pre-solar grains.

Thanks to the background reduction of the underground environment, we were able to measure the ^{18}O(p,α)^{15}N reaction down to $E_{CM} = 50$ keV, the lowest energy to date. Furthermore, we observed a new resonance at $E_{CM} = 104$ keV and found that the strength of a previously observed resonance at $E_{CM} = 89$ keV

is an order of magnitude higher than previously reported. Our new determination of the cross-section significantly reduced the uncertainty in the rate of the ^{18}O(p,α)^{15}N reaction, improving the constraints on the abundance of the ^{18}O isotope in a number of stellar sites.

In summary, this thesis presented the results from an experimental campaign aimed at measuring the ^{17,18}O(p,α)^{14,15}N nuclear reactions. Both reactions were studied successfully and new reaction rates were derived with the best precision achieved to date. These results have significant implications in a number of astrophysical scenarios including RGB and AGB stars, pre-solar grains and Galactic chemical evolution.

Appendix A

Alpha-particle peaks fitting

The presence of a low-energy tail in the peaks originating from the interaction of charged particles in solid-state detectors is very well established [58]. These tails can be due to a combination of various physical phenomena such as e.g. energy straggling and pulse height defect, depending on the experimental conditions. Events observed in the tail have the same physical origin as those in the main peak, and must be taken into account when computing the total number of detected events. This appendix deals with the problem of extracting a number of counts from the alpha particle peaks observed in the energy spectra during the experimental campaigns aimed at measuring the ^{17,18}O(p,α)^{14,15}N reactions.

A.1 The fitting function

The problem of extracting a number of detected events from an alpha particle spectrum acquired by a silicon detector is not new [90], a relatively recent review of the strategies that can be employed to solve this issue can be found in ref. [91]. After a few trials, I decided to fit the alpha peaks employing a skewed Gaussian function following an approach close to the one proposed in ref. [90]. The skewed Gaussian fitting function is obtained as a convolution product between a Gaussian $g(x)$ and a shape function $s(x)$

$$f(x) = g(x) * s(x) \tag{A.1}$$

where

$$g(x) = \frac{A}{\sigma\sqrt[2]{2\pi}} \exp\left\{-\frac{(x-\mu)^2}{2\sigma^2}\right\} \tag{A.2}$$

$$s(x) = \epsilon\phi_1 + (1-\epsilon)\phi_2 + k \tag{A.3}$$

$$\phi_i = \frac{1}{\tau_i} \exp\left\{\frac{x}{\tau_i}\right\} [1 - H(x)] \tag{A.4}$$

where A, σ and μ are the area, standard deviation and mean parameter of the Gaussian, ϵ is a weight parameter, τ_i is a tail shape parameter, k is a positive constant and $H(x)$ is the Heaviside step function. The convolution in Eq. A.1 can be calculated analytically and results in

$$\begin{aligned} f(x) = A & \left(\frac{\exp\left\{\frac{\sigma^2 + 2\tau_1(x-\mu)}{2\tau_1^2}\right\} \epsilon \operatorname{Erfc}\left\{\frac{x-\mu+\frac{\sigma^2}{\tau_1}}{\sigma\sqrt{2}}\right\}}{2\tau_1} \right) + \\ + A & \left(\frac{\exp\left\{\frac{\sigma^2 + 2\tau_2(x-\mu)}{2\tau_2^2}\right\} \epsilon \operatorname{Erfc}\left\{\frac{x-\mu+\frac{\sigma^2}{\tau_2}}{\sigma\sqrt{2}}\right\}}{2\tau_2} \right) + Ak = \\ & = A\left[b_1(x) + b_2(x) + k\right] \end{aligned} \tag{A.5}$$

where Erfc(x)=1-Erf(x), and Efx(x) is the error function. Note that ref. [90] obtains a result which is arranged in a different way, but equivalent. The fitting function in Eq. A.5 consists of three parts summed together (Fig. A.1). The first two, called $b_i(x)$ are tailed Gaussians or skewed Gaussians while the third part is a constant that reproduces the long-range behaviour of the tail. This

last component is not always required, depending on the physical process that produces alpha particles and the statistics available.

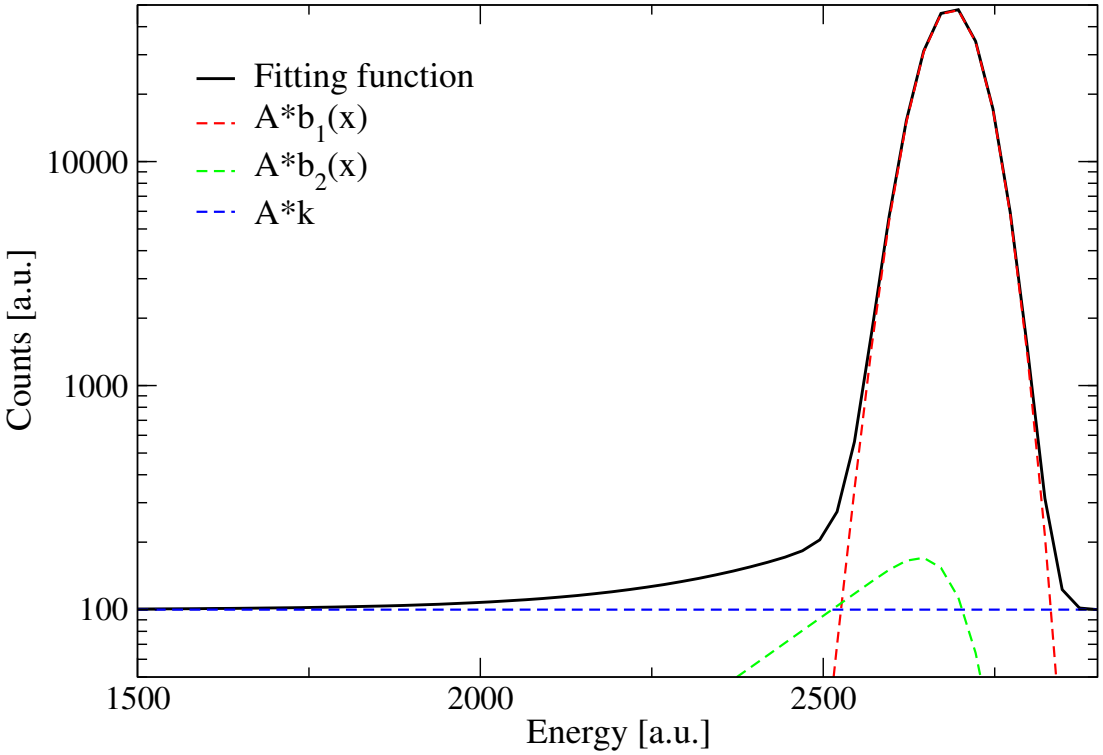

Figure A.1 *The three components of the fitting function in Eq. A.5.*

I attempted to use Eq. A.5 to fit a ^{241}Am spectrum acquired with collimators (Fig. A.2 top) and an alpha peak from the $E_{\mathrm{p}} = 151$ keV resonance in ^{18}O(p,α)^{15}N (Fig. A.2 bottom). Visually, the results are very good and the reduced χ^2 is 1.7 for the ^{241}Am spectrum and 5.9 for the $E_{\mathrm{p}} = 151$ keV resonance. In this second case, the disagreement between the function and the data is primarily on the high energy half of the peak ($E \simeq 2800$ keV) as opposed to the tail. In conclusion, Eq. A.5 appears to work reasonably well to fit high-statistics alpha peaks.

The purpose of these fits was to obtain the number of counts. However, since the shape function $s(x)$ is not normalised[1], to extract an area $\mathbb{A}$ from the function one cannot simply take the Gaussian area parameter A. Instead, one has to integrate Eq. A.5. However, the presence of the k parameter makes the integral of $f(x)$ divergent, that is to say

$$\mathbb{A} = \int_{-\infty}^{+\infty} f(x)dx = A \int_{-\infty}^{+\infty} [b_1(x) + b_2(x) + k]dx$$

[1]Its integral is not unity

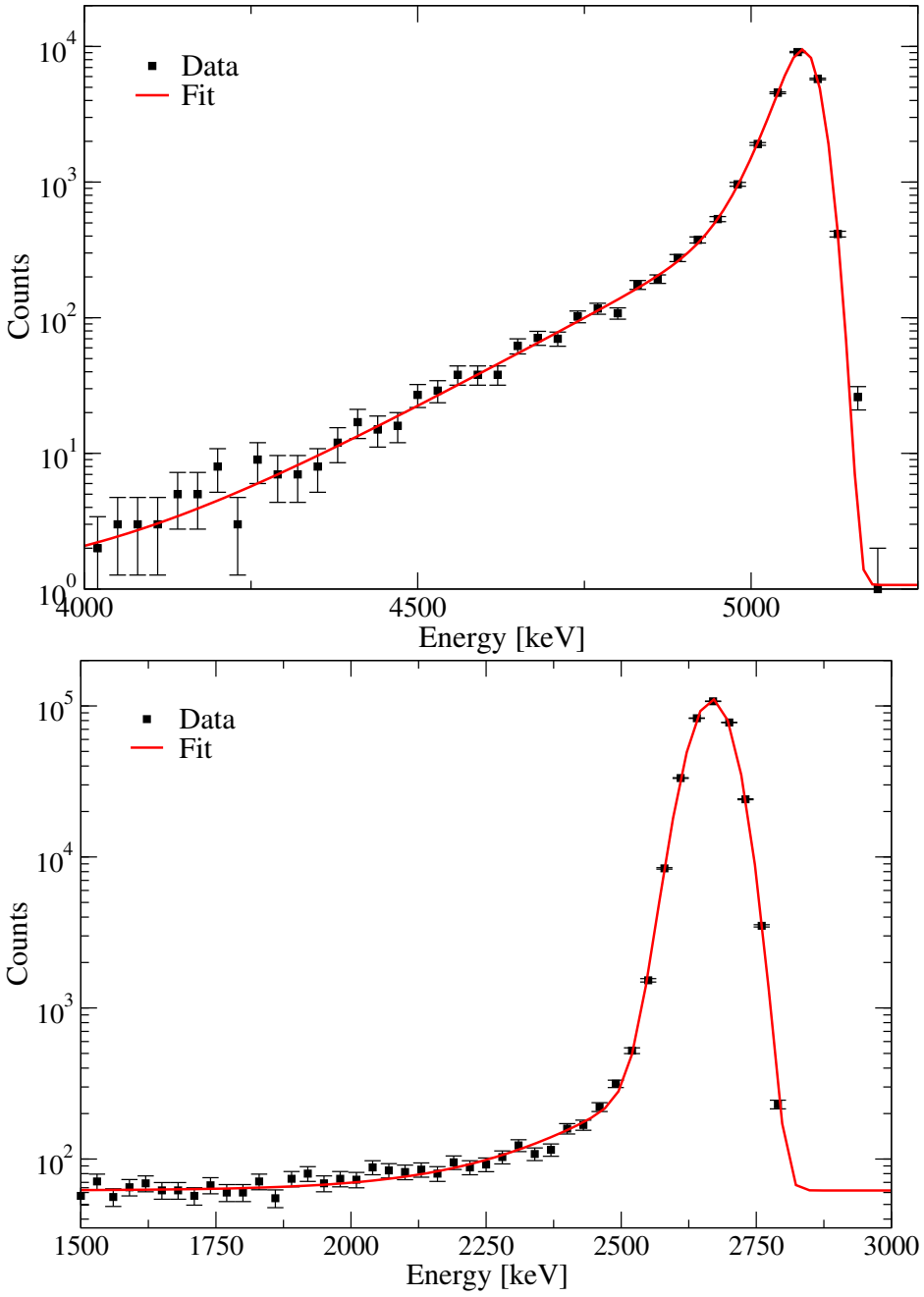

Figure A.2 *Fits employing Eq. A.5 to the alpha peak of a ^{241}Am radioactive source, and the $E_p = 151$ keV resonance in $^{18}O(p,\alpha)^{15}N$ (top and bottom). See text for details.*

does not converge. To obtain $\mathbb{A}$, we can instead integrate Eq. A.5 over the region in which we are fitting it

$$\mathbb{A} = \int_{E_{\min}}^{E_{\max}} f(x)dx = A\left(\int_{E_{\min}}^{E_{\max}} [b_1(x) + b_2(x)]dx + k\Delta E\right) \tag{A.6}$$

and as long as the energy region $[E_{\min}, E_{\max}]$ is larger than the energy region $[\mu - \sigma - \tau, \mu + \sigma]$ in which the two skewed Gaussians are significantly different from zero, we can approximate the integral in Eq. A.6 with an integral from $-\infty$ to $+\infty$, or formally if

$$\int_{E_{\min}}^{E_{\max}} [b_1(x) + b_2(x)]dx \gg \int_{-\infty}^{E_{\min}} [b_1(x) + b_2(x)]dx + \int_{E_{\max}}^{+\infty} [b_1(x) + b_2(x)]dx$$

then the area $\mathbb{A}$ can be written as

$$\mathbb{A} = A(1 + k\Delta E) \tag{A.7}$$

In order to test the influence of the tail on the main peaks as well as the reliability of this fitting method, I compared the result obtained from Eq. A.7 against a simple integral of the number of counts in the energy region of the peak. The difference in the number of counts obtained with the two methods is quite small, and neglecting the tail appears to result in a loss of approximately 2% of the total number of events. While small, this difference is not completely negligible and therefore - if possible - one should use a fit to obtain the number of alpha particles.

A.2 The $E_{\mathrm{p}} = 193$ keV resonance in ^{17}O(p,α)^{14}N

I attempted to employ Eq. A.5 to fit the alpha peak from the $E_{\mathrm{p}} = 193$ keV in ^{17}O(p,α)^{14}N where, because of the presence of the low-energy background, the alpha peak tail is not observable (Fig. A.3). I found that the constant contribution k was no longer needed, and I was instead forced to use an arbitrary exponential function to fit the low-energy background as proposed in refs. [33, 34]. In order to further reduce the influence of the low-energy beam-induced background, before carrying out the fits, I normalised in charge and subtracted a spectrum acquired off-resonance at $E_{\mathrm{p}} = 192$ keV from a typical spectrum acquired on-resonance at $E_{\mathrm{p}} = 194$ keV. Even after this subtraction, the tail cannot be seen, and therefore the long-range tail coefficient τ_2 and the weight coefficient ϵ in Eq. A.5 cannot be optimised. To solve this issue, I attempted

to employ two fitting strategies. In both approaches I started by fitting an exponential function of the type

$$E(x) = B * \exp(-Cx) \tag{A.8}$$

to the low energy background. Since according to ref. [90], the τ coefficients do not depend on the energy of the peak, as a first approach I employed the same τ_2 value as found for the fit of the alpha peak of the $E_{\mathrm{p}} = 151$ keV resonance in ^{18}O(p,α)^{15}N. I optimised the other coefficients, including B and C and obtained a fit, shown in Fig. A.3 (top), with a reduced χ^2 of 15. This is a poor statistical result and, furthermore, it is not obvious that the tail is being reproduced properly. Ref. [90] does not provide many details on the evidence supporting the claim that τ does not depend on the energy of the alpha peak. In fact this claim was supported only by data acquired with alpha particle radioactive sources in a small energy range ($E_\alpha \simeq 5$ MeV). In conclusion, this first fitting gives bad statistical results and does not appear to work.
It is quite obvious that $b_2(x)$ gives a very limited contribution in the previous strategy. Therefore, the second approach consisted in removing $b_2(x)$ from Eq. A.5 entirely, and using only $b_1(x)$ to fit. After optimising the parameters, again including B and C from the exponential function, I obtained the result in Fig. A.3 (bottom). The reduced χ^2 is 10, which is better than for the first strategy, but still statistically questionable. Critically note that the fit is almost indistinguishable from the previous one, except for the tail which is even less prominent. The events in the tail of the peak - if there is a tail - are clearly not being accounted for. Since obtaining the events in the tail was the purpose of the fitting procedure, this second fitting strategy did not appear viable. Ultimately, the main issue in both approaches was that it is not obvious whether the peak we were trying to fit had a tail or not, and therefore it was not possible to fit it.

A.3 Conclusions

Alpha particle peaks detected throughout this experiment show a clear low-energy tail. In order to account for the number of detected events in this tail, I developed a fitting function (Eq. A.5) following an approach similar to that proposed in ref. [90]. The approach is quite successful for clear, isolated, high-energy ($\mathrm{E}_\alpha >$ 1 MeV) alpha peaks, but fails for the alpha peak of the $E_{\mathrm{p}} = 193$ keV resonance

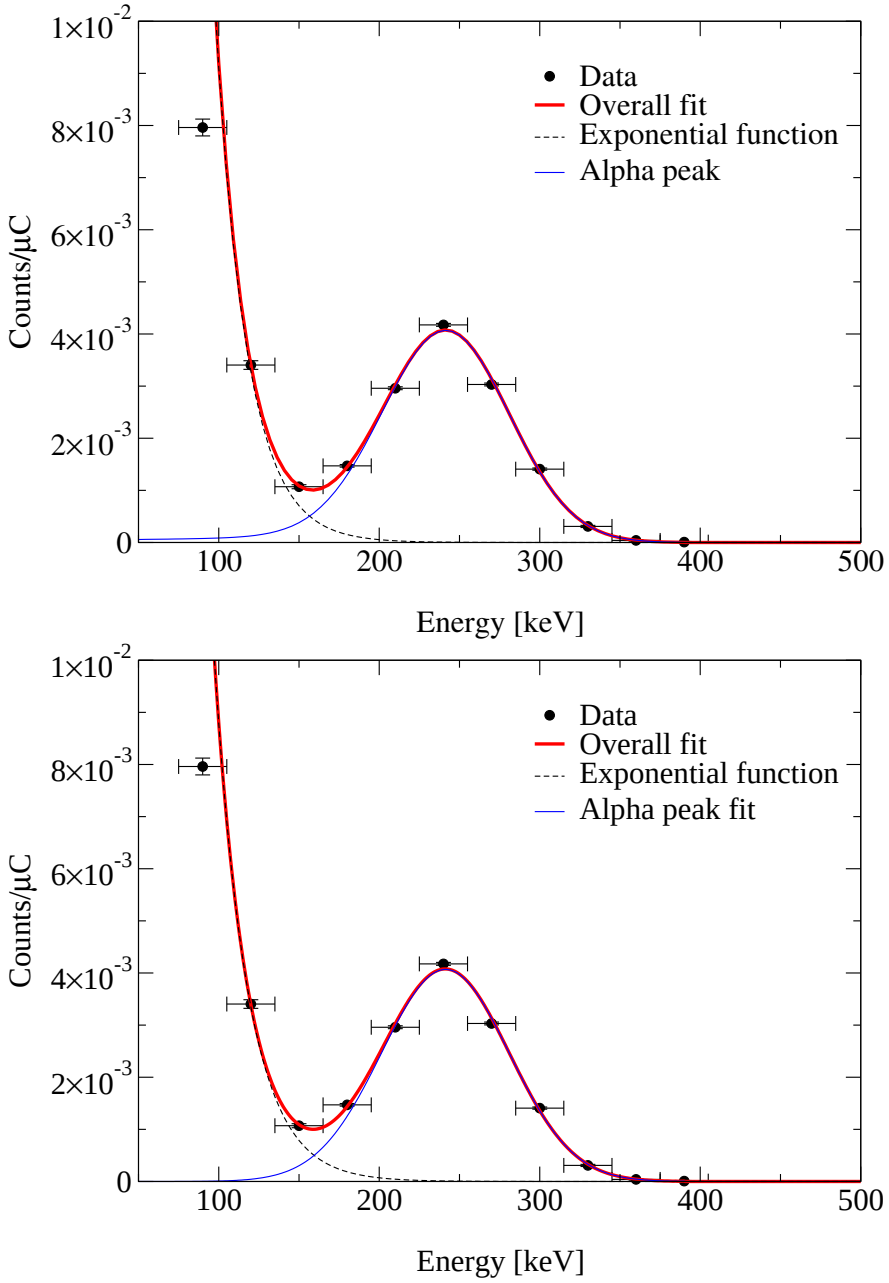

Figure A.3 *Fits to the alpha peak from the E_p = 193 keV resonance in the $^{17}O(p,\alpha)^{14}N$ reaction employing two fitting strategies. The reduced χ^2 coefficients are 15 (top) and 10 (bottom). In spite of the difference in reduced χ^2 the two plots are almost indistinguishable, except for the alpha peak tail that is slightly more prominent in the top fit. See text for details on the fitting functions employed.*

in the $^{17}O(p,\alpha)^{14}N$ reaction, where the tail - if it exists - is masked by the low-energy background. Since the fitting function does not work for the $E_p = 193$ keV resonance where a peak is visible, it is not reasonable to use Eq. A.5 to fit the alpha peak of the $E_p = 70$ keV resonance in the $^{17}O(p,\alpha)^{14}N$ reaction, for which

both the peak and the tail are masked by the natural background. Therefore, a simple integral of the number of counts in the main alpha peak was used in this work to quantify the number of detected events. For consistency, this approach was used at all energies and for both reactions. To account for the possibility of a tail peak, an asymmetric +2% uncertainty was added to the number of counts. This +2% uncertainty is derived from a comparison between the results given by fitting Eq. A.5 and integrating the counts in the alpha peak of the $E_{\mathrm{p}} = 151$ keV resonance in $^{18}\mathrm{O}(\mathrm{p},\alpha)^{15}\mathrm{N}$, where both the fit and the integral could be carried out.

Appendix B

Maximum Likelihood

The aim of this appendix is to find an estimator to obtain the best value for the number of alpha particle counts N_α obtained for the measurement of the $E_\mathrm{p} = 70$ keV resonance in the $^{17}\mathrm{O(p,}\alpha)^{14}\mathrm{N}$ reaction. A simple approach based on subtracting the background from the foreground, presented in section 5.2.8, resulted in negative charge-normalised background-subtracted (CNBS) off-resonance rates, which are potentially unphysical. In this appendix another estimator for the number of counts is proposed. This estimators is built following the approach in ref. [77] in a way that ensures the number of counts, and thus the rate, cannot be negative.

B.1 Obtaining the estimator

The key idea is to write the probability of observing the events during on-resonance ($E_\mathrm{p} = 71.5$ keV), off-resonance ($E_\mathrm{p} = 65$ keV) and background (beam off) runs as a product of the individual probabilities. Let us first consider the background data. During the background runs, we detected a given number m of counts. These counts are obtained from a Poissonian probability distribution with mean b_bkg which in general is not equal to m. Given a Poissonian distribution with mean b_bkg, the probability P of observing m counts is

$$P(b_\mathrm{bkg}; m) = \frac{b_\mathrm{bkg}^m}{m!} e^{-b_\mathrm{bkg}} \tag{B.1}$$

Let us now consider the on-resonance data, and let us neglect for a moment the possibility of beam-induced background. The n counts that we observed are either background counts extracted from a Poissonian with mean $b_{\rm on}$ or signal events extracted from a Poissonian with mean μ. We can write the probability P as

$$P(\mu + b_{\rm on}; n) = \frac{(b_{\rm on} + \mu)^n}{n!} e^{-(\mu + b_{\rm on})} \tag{B.2}$$

We can combine Eq. B.1 and B.2 to write the compound probability of observing n counts during the background and m counts during the on-resonance, given the underlying Poissonian distributions. Note that $b_{\rm bkg}$ and $b_{\rm on}$ are in general different, since the on-resonance data and the background data were acquired for different lengths of time. The background rate is the same, but the number of counts is not. Explicitly

$$\frac{b_{\rm bkg}}{t_{bkg}} = \frac{b_{\rm on}}{t_{on}} \Rightarrow b_{\rm bkg} = b_{\rm on} \frac{t_{\rm bkg}}{t_{\rm on}} = b_{\rm on}\tau = b\tau \tag{B.3}$$

where $b = b_{\rm on}$ and $\tau = \frac{t_{\rm bkg}}{t_{\rm on}}$. Using this notation we can write

$$L(\mu, b; m, n) = P(\mu + b; m) \times P(\tau b; m) = \frac{(b + \mu)^n}{n!} e^{-(\mu + b)} \frac{(\tau b)^m}{m!} e^{-\tau b} \tag{B.4}$$

where L is the likelihood of observing m counts on-resonance and n counts off-resonance, given a signal rate μ and a background rate b, where "rate" here has the meaning of "expected value of a Poissonian distribution over a time $t_{\rm on}$". Everything in Eq. B.4 is defined except μ and b and one could in principle maximise L, or equivalently minimise $-\log L$, as a function of μ, b to find their most likely values. In Maximum Likelihood theory, these most likely values are indicated as $\hat{\mu}, \hat{b}$. Adding the possibility of beam-induced non-signal counts in Eq. B.4 is a straightforward extension. We can define

$$\tau_{\text{bkg}} = \frac{t_{\text{bkg}}}{t_{\text{on}}} \tag{B.5}$$

$$\tau_{\text{off}} = \frac{t_{\text{off}}}{t_{\text{on}}} \tag{B.6}$$

$$\omega = \frac{Q_{\text{off}}}{Q_{\text{on}}} \tag{B.7}$$

where Q is the charge deposited. Note we have to use the charge Q as opposed to the effective charge k which has no meaning off-resonance. With these definitions we can write the combined probability of observing the counts on-resonance, off-resonance and during background as

$$\begin{aligned} L(\mu, b, \nu; m, n, l) &= P(\mu + b + \nu; m) \times P(\tau_{\text{bkg}} b; m) \times P(\tau_{\text{off}} b + \omega\nu; l) \\ &= \frac{(b+\mu+\nu)^n}{n!} e^{-(\mu+b+\nu)} \frac{(\tau_{\text{bkg}} b)^m}{m!} e^{-\tau_{\text{bkg}} b} \frac{(\tau_{\text{off}} b + \omega\nu)^l}{l!} e^{-(\tau_{\text{off}} b + \omega\nu)} \end{aligned} \tag{B.8}$$

where l is the number of counts observed off-resonance and ν is the off-resonance rate, in the same sense as μ and b. The only important assumption in Eq. B.8 is that the beam-induced non-signal rate ν scales as the ratio of the charges ω. Since the off-resonance and the on-resonance were taken at different energies, if we were dealing with a beam-induced background process that strongly depends on energy this assumption may not be true. However since we found no evidence for any kind of beam-induced background in sections 5.2.6 and 5.2.7, it seems justified to assume that ν has a linear dependence on ω.

The physical problem that led us to write Eq. B.8 was that the off-resonance CNBS rate was negative. To enforce a non-negative rate, we can now simply maximise the likelihood in Eq. B.8 with the condition $\nu \geq 0$. The results are reported in Table B.1 and are in excellent agreement with those results one would obtain from the simple subtraction method previously employed in section 5.2.8 (i.e. Eq. 5.12). Note $\hat{\mu} = N_{\alpha,\text{tot}}$.

Table B.1 *Best values for signal rate μ, background rate b and beam-induced non-signal rate ν as obtained with a simple subtraction method in section 5.2.8 (Eq. 5.12) and a Maximum Likelihood (ML) approach. Note "rate" here has the meaning of "expected value of a Poissonian distribution over a time t_{on}", where t_{on} is the on-resonance acquisition time. Results are consistent.*

Method	$\hat{\mu}$	$\hat{b}$	$\hat{\nu}$
Subtraction	1222 ± 165	13814 ± 111	-109 ± 194
ML	1257 ± 178	13779 ± 98	0^{+55}_{-0}

B.2 Obtaining the uncertainties

Using the subtraction method the uncertainties are trivially computed from Poissonian statistics and error propagation. However, obtaining the uncertainties for the Maxmimum Likelihood method is significantly more complicated. In general there are several ways to proceed, some of which have advantages and disadvantages. A full review is beyond the scope of this work, see instead refs. [74, 77]. In this case for computational ease I employed a Monte Carlo technique to estimate the uncertainties. This technique consists in assuming that the best values obtained from the minimisation are the mean values of the Poissonian distributions (i.e. $\mu = \hat{\mu}$). Under this assumption, using the Poissonian distributions in Eq. B.8, one generates a large number of simulated observed values m_i, n_i, l_i. For each observation, one employs Eq. B.8 to maximise the likelihood and extract a set of best values $\hat{\mu}_i, \hat{b}_i, \hat{\nu}_i$. The distribution of these simulated best values follows a Gaussian in most cases, and one can take its standard deviation as the uncertainty. As an example, Fig. B.1 (top) shows the distribution of the simulated $\hat{\mu}_i$, which has $\hat{\mu}$ (the experimental best value) as the mean and standard deviation equal to 178 (Table B.1).

The distribution of $\hat{b}_i$ is also Gaussian, but as expected the distribution of $\hat{\nu}_i$ is not. This is a result of the constraint $\nu \geq 0$ which "cuts" the Gaussian at zero, and forces all negative values to be zero. See Fig. B.1 (bottom). In this case, I computed the uncertainty reported in Table B.1 as the 68% confidence interval [73, 74]. Other choices would be possible, but note that conveniently the uncertainty in $\hat{\mu}$ does not depend on our choice of the uncertainty in $\hat{\nu}$, which is in any case never used in this work.

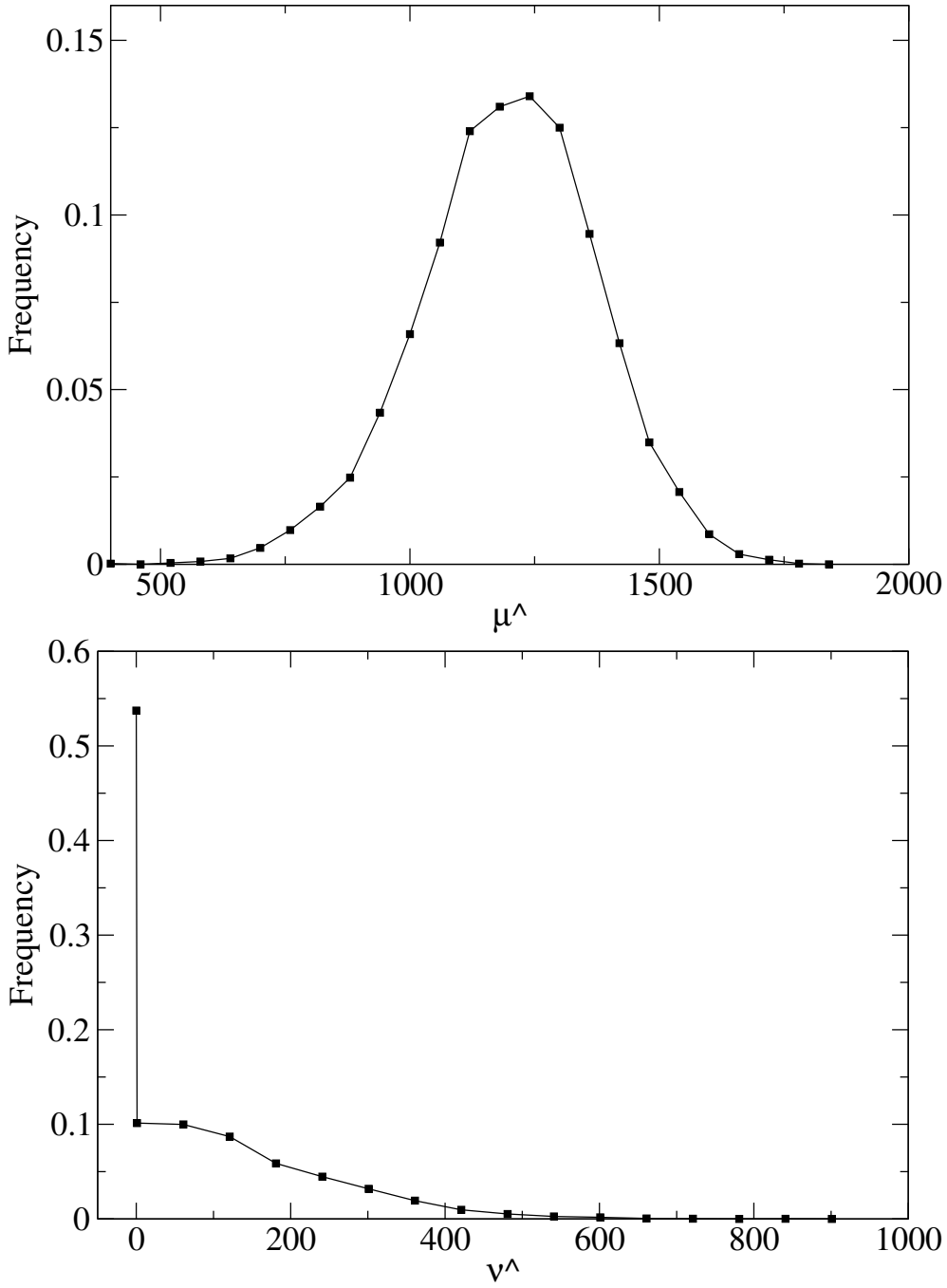

Figure B.1 *The distribution of the ML estimates for the signal counts $\hat{\mu}_i$ (top) and the beam-induced background counts $\hat{\nu}_i$ (bottom) obtained from 10 000 simulated events. The black lines are just guides to the eye. In the bottom plot, the first marker refers to values of $\hat{\nu}_i = 0$, while the second symbol refers to values between 0 and 1. See text for details.*

B.3 Conclusions

A Maximum Likelihood estimator for the number of alpha particle counts N_α detected during the measurement of the $E_\mathrm{p} = 70$ keV resonance in the $^{17}\mathrm{O}(\mathrm{p},\alpha)^{14}\mathrm{N}$ reaction has been proposed. The number of counts obtained and their uncertainty is in agreement with the values found using a simple subtraction method described in section 5.2.8. The ML estimator has numerous advantages over the subtraction method, including the possibility of accounting explicitly for the possibility of beam-induced background. The N_α value obtained from this estimator was used to calculate the strength of the $E_\mathrm{p} = 70$ keV resonance in the $^{17}\mathrm{O}(\mathrm{p},\alpha)^{14}\mathrm{N}$ reaction.

Bibliography

[1] C. Iliadis. *Nuclear Physics of Stars*, Wiley-VCH, 1st ed. (2007).

[2] C. Iliadis. *Nuclear Physics of Stars*, Wiley-VCH, 2nd ed. (2015).

[3] C. E. Rolfs and W. S. Rodney. *Cauldrons in the Cosmos*, The University of Chicago Press, (1988).

[4] M. Lugaro *et al.* Nature Astronomy. **1** (2017) 27.

[5] P. Ventura *et al.* Astron. Astrophys. **461** (2007) 657-664.

[6] G.J. Wasserburg *et al.* Atrophys. J. **447** (1995) L37-L40.

[7] C.A. Frost *et al.* Astron. Astrophys. **332** (1998) L17-L20.

[8] K. M. Nollett *et al.* Atrophys. J. **582** (2003) 1036-1058.

[9] P. Ventura *et al.* MNRAS. **431** (2013) 3642-3653.

[10] O. Straniero *et al.* Astron. Astrophys. **598** (2017) A128.

[11] J. Ziegler. SRIM 2013, from url: http://srim.org , (accessed 04/2017).

[12] C.R. Brune and D.B. Sayre. Nuc. Inst. Meth. Phys. A, **698** (2013) 49-59.

[13] P. Descouvemont and D. Baye. Repr. Prog. Phys. **73** (2010) 036301.

[14] K.S. Krane. *Introductory Nuclear Physics*, Wiley & Sons. (1987).

[15] C. Spitaleri *et al.* Phys. Lett. B, **755** (2016) 275-278.

[16] H.J. Assenbaum *et al.* Z. Phys. A, **327** (1987) 461-468.

[17] L. Bracci *et al.* Nucl. Phys. A, **513** (1990) 316-343.

[18] F. Strieder *et al.* Naturwissenschaften. **88** (2001) 461-467.

[19] R. Longland *et al.* Nucl. Phys. A, **841** (2010) 1-30.

[20] A.L. Sallaska *et al.* Astrophy. J Suppl. **207** (2013) 18.

[21] STARLIB compilation. from url: http://starlib.physics.unc.edu/. (accessed 04/2017).

[22] K. Ahnlund *et al.* Phys. Rev. **106** (1957) 124.

[23] R.E. Brown *et al.* Phys. Rev. **125** (1962) 347.

[24] W.E. Kieser *et al.* Nucl. Phys. A, **331** (1979) 155-179.

[25] E.A. Silverstein *et al.* Phys. Rev. **124** (1961) 868-876.

[26] G. Bogaert *et al.* Phys. Rev. C, **39** (1989) 265.

[27] A. Chafa *et al.* Phys. Rev. C, **75** (2007) 035810.

[28] C. Fox *et al.* Phys. Rev. Lett. **93** (2004) 081102-1.

[29] A. Chafa *et al.* Phys. Rev. Lett. **95** (2005) 031101.

[30] B.H. Moazen *et al.* Phys. Rev. C. **75** (2007) 065801.

[31] J.R. Newton *et al.* Phys. Rev. C, **75** (2007) 055808.

[32] M. Berheide *et al.* Z. Phys. A, **343** (1992) 483-487.

[33] J.C. Blackmon *et al.* Phys. Rev. Lett. **74** (1995) 14.

[34] J.C. Blackmon. PhD thesis, University of North Carolina at Chapel Hill (1994).

[35] S. Niemeyer. Diplomarbeit, Ruhr-Universität Bochum (1996).

[36] M.D. Hannam and W.J. Thompson. Nuc. Inst. Meth. A, **431** (1999) 239-251.

[37] C. Iliadis. *private communication.* (2016).

[38] M.L. Sergi *et al.* Phys. Rev. C, **82** (2010) 032801(R).

[39] M.L. Sergi *et al.* Phys. Rev. C, **91** (2015) 065803.

[40] F. Ajzenberg-Selove. Nucl. Phys. A, **190** (1972) 1-196.

[41] F. Ajzenberg-Selove. Nucl. Phys. A, **300** (1978) 1-224.

[42] C. Angulo *et al.* Nucl. Phys. A, **656** (1999) 3-183.

[43] M. La Cognata *et al.* Astrophys. J, **723** (2010) 1512.

[44] H-M. Lorenz-Wirzba *et al.* Nucl. Phys. A, **313** (1979) 346.

[45] H.-B. Mak *et al.* Nucl. Phys. A, **304** (1978) 210.

[46] N.S. Christensen *et al.* Nucl. Inst. Meth. Phys. B. **51** (1990) 97.

[47] G. Amsel and D. Samuel. Anal. Chem. **39** (1967) 1689.

[48] K. Yagi. J. Phys. Soc. Japan, **17** (1962) 4.

[49] H. Smotrich *et al.* Phys. Rev. **122** (1961) 232.

[50] M. La Cognata *et al.* Phys. Rev. Lett. **101** (2008) 152501.

[51] H.W. Becker *et al.* Z. Phys. A, **351** (1995) 453-463.

[52] H.T. Fortune. Phys. Rev. C, **88** (2013) 015801.

[53] C.G. Bruno *et al.* Eur. Phys. J. A, **51** (2015) 94.

[54] A. Formicola *et al.* Nucl. Phys. Meth. A. **507** (2003) 609-616.

[55] H. Costantini *et al.* Rep. Prog. Phys. **72** (2009) 086301.

[56] A. Caciolli *et al.* Eur. Phys. J. A, **48** (2012) 144.

[57] V.F.E. Pucknell and D. Laff. MIDAS (Multi Instance Data Acquisition System), from url http://npg.dl.ac.uk/MIDAS/. (accessed 04/2017).

[58] G. Knoll. *Radiation Detection and Measurement*, 3rd edition, Wiley-VCH Verlag GmbH. (2000).

[59] C.G. Bruno. Master Thesis, University of Milano (2013).

[60] Goodfellow. from url http://www.goodfellow.com. (accessed 04/2017).

[61] DuPont. from url http://www.dupont.co.uk. (accessed 04/2017).

[62] Lebow Company. from url http://www.lebowcompany.com. (accessed 04/2017).

[63] Canberra PIPS Detectors data sheet. from URL http://www.canberra.com/. (accessed 04/2017).

[64] GEANT4. from url http://geant4.cern.ch. (accessed 04/2017).

[65] C.J. Griffin. Master Thesis, University of Edinburgh (2014).

[66] A. Lemut. unpublished. (2012).

[67] D.A. Scott *et al.* Phys. Rev. Lett. **109** (2012) 202.

[68] D.A. Scott. PhD Thesis, University of Edinburgh (2014).

[69] H.-B. Mak *et al.* Nucl. Phys. A. **343** (1980) 79.

[70] M. Junker *et al.* Phys. Rev. C. **57** (1998) 5.

[71] M. Misiaszek *et al.* Appl. Radiat. Isot. **81** (2013) 146.

[72] C.G. Bruno *et al.* Phys. Rev. Lett. **117** (2016) 142502.

[73] P.R. Bevington and D.K. Robinson. *Data Reduction and Error Analysis for the Physical Sciences*, McGraw Hill 3rd edition, (2003).

[74] G. Cowan. *Statistical Data Analysis*, Clarendon Press, Oxford, (1998).

[75] J.R. Newton. PhD thesis, University of North Carolina at Chapel Hill (2010).

[76] R.E. Azuma *et al.* Phys. Rev. C. **81** (2010) 045805.

[77] G. Cowan *et al.* Eur. Phys. J C. **71**(2011) 1554.

[78] M.Q. Buckner *et al.* Phys. Rev. C. **91**(2015) 015812.

[79] C. Iliadis *et al.* Nucl. Phys. B. **841**(2010) 31-250.

[80] M. Wang *et al.* Chin. Phys. C. **36**(2012) 12.

[81] S. Stave *et al.* Phys. Lett. B. **696** (2012) 26-29.

[82] GNU Scientific Library. from url http://www.gnu.org. (accessed 04/2017).

[83] H. Akima. ESSA Tech. Rep. ERL 101-ITS 73. (1969).

[84] P. Descouvemont. DREAM. (2015), pdesc@ulb.ac.be.

[85] Experimental Nuclear Reaction Data (EXFOR). Database Version of 2017-02-01. (accessed 04/2017).

[86] T. Lebzelter *et al.* Astron. Astrophys. **578** (2015) A33.

[87] O. Straniero. *private communication.* (2017).

[88] M. Lugaro. *private communication.* (2017).

[89] P. Marigo. *private communication*. (2017).

[90] G. Bortels and P. Collaers. Appl. Radiat. Isot. **38** (1987) 831-837.

[91] E. Garcia-Torano. Appl. Radiat. Isot. **64** (2006) 1273-1280.